Algorithms for Tissue Image Analysis using Multifractal Techniques

---

A thesis submitted in partial fulfilment

of the requirements for

the Degree of Master of Science

in Computer Science and Software Engineering

in the University of Canterbury

by

ChiangHau TAY

Dr R. Mukundan……..Supervisor
Associate Professor, Department of Computer Science and Software Engineering

Dr D. Racoceanu…….Co-Supervisor
Director, Image & Pervasive Access Lab, Singapore

University of Canterbury

2012

Abstract

Histopathological classification and grading of biopsy specimens play an important role in early cancer detection and prognosis. Nottingham Grading System (NGS) is one of the standard grading procedures used in breast cancer assessment, where three parameters, Mitotic Count (MC), Nuclear Pleomorphism (NP), and Tubule Formation (TF) are used for prognostic information. The grading takes into account the deviations in cellular structures and appearance between tumour and normal cells, using measures such as density, size, colour, and regularity. Cell structures in tissue images are also known to exhibit multifractal characteristics.

This research focused on the multifractal properties of several graded biopsy specimens and analysed the dependency and variation of the fractal parameters with respect to the scores pre-assigned by pathologists. The effectiveness of using multifractal techniques on breast cancer grading was measured with a set of quantitative evaluations for MC, NP, and TF criteria. The developed method for MC scoring has obtained 82.87% true positive rate on detecting mitotic cells. Furthermore, the overall positive classification rates for NP and TF analysis were 67.38% and 71.82%, respectively, while obtaining 30.26% of false classification rate for NP analysis and 27.17% for TF analysis. The results have shown that multifractal formalism is a feasible and novel method that could be used for automatic grading of biopsy sections.

Acknowledgements

It is my pleasure to thank my supervisor Dr R. Mukundan for his guidance and help during my research. My Masters degree could not be achieved without his support and advice.

Special thanks to the staff members of the Image & Pervasive Access Lab (IPAL), Singapore. This thesis would not have been possible without the support from the director of IPAL, Dr D. Racoceanu, my co-supervisor, who has provided valuable inputs. The group has provided essential software, histopathological images, and related information which were extremely useful for this research. I am grateful for the help and support received from Dr L. Roux and Dr N. Lomenie during my visit to IPAL.

It is an honour for me to have the financial support from the Department of Computer Science and Software Engineering for me to visit IPAL in Singapore. I would also like to thank the Department for providing all the support and resources required for my research.

Finally, I must acknowledge the support from my family, friends, Mrs S. Day from Learning Skills Centre, and colleagues from the department for helping and supporting me throughout my studies.

Table of Contents

List of Figures

List of Tables

List of Abbreviations

ACM	Active Contour Model
ASL	Arterial spin labelling
ASR	Age-standardised rate
AT	Area that represents water, carbohydrate, lipid or gas
CMY	Cyan, magenta, and yellow (colour space)
CPU	Central processing unit
CT	Computed tomography
ECM	Collagen-based matrix
EEG	Electroencephalogram
FMRI	Functional Magnetic Resonance Imaging
GPU	Graphics processing unit
HPF	High-power field
IARC	International Agency for Research on Cancer
IPAL	Image & Pervasive Access Lab
MC	Mitotic Count
MF-DFA	Multifractal Detruded Fluctuation Analysis
NGS	Nottingham Grading System
NM1	Nuclei of inflammatory cells
NM2	Cell nuclei of epithelial origin
NM3	Nuclei of cancer cells
NP	Nuclear Pleomorphism
REM	Rapid eye movement

ROC	Receiver operating characteristic
ROI	Region of interest
SBR	Scarff-Bloom-Richardson
SVM	Support Vector Machine
SWS	Slow wave sleep
TF	Tubule Formation
WTMM	Wavelet Modulus Maxima Method

Chapter 1:

Introduction

Cancer is a term that describes the uncontrolled growth of abnormal cells in the body [1]. Normal cells follow the orderly path of growth, division, and death. Cancer cells begin to form when this process breaks down, as they continue to expand and divide. This leads to a mass of abnormal cells that grows out of control. Healthy tissue can be invaded by cancer cells; it can harm the body when the abnormal cells start to form lumps or masses of tissue, known as tumours, which can interfere with the body's system and function.

More than 100 different types of cancer have now been discovered. According to the statistics collected by the International Agency for Research on Cancer (IARC), breast cancer is the most frequent type of cancer among women worldwide, as shown in Figure 1-1 [2-4]. The statistic has shown that the incidence and mortality rates for breast cancer have rapid growth in many Eastern European, Asian, Latin American, and African countries [5]. In addition, breast cancer is the major cause of death for women in several developing and developed countries. Lack of funding and resources are the reason why these patients do not receive medical treatment [2, 5].

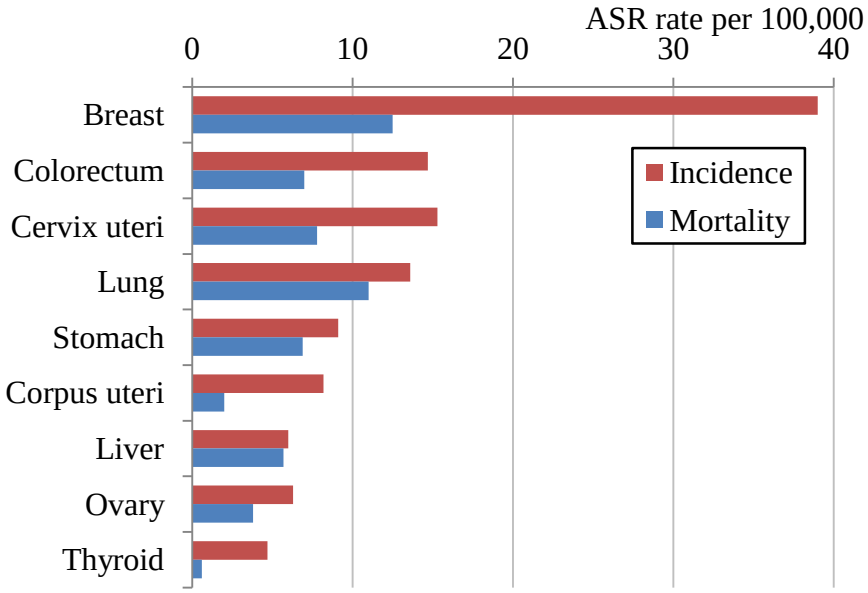

Figure 1-1 The top nine most frequent cancers for women worldwide, 2008 [2]

Studies have shown that death from breast cancer can be reduced if the disease is managed. An age-standardised rate (ASR) was introduced to adjust the population age structures based on different periods of time, geographic areas, and population sub-groups. ASR is the ratio of a specific rate in the population being studied over the population of an age group in standard population [6]. A health services research showed the incidence rate of breast cancer is 39.0 ASR per 100,000 people, while the mortality rate is 12.5 ASR per 100,000 people. Compared to lung cancer which has a high incidence-to-mortality ratio of 1: 0.81, breast cancer has a lower ratio of 1: 0.32 [2]. Improving disease management can increase the chances of survival and recovery from breast cancer [7].

1.1 Motivation

Early detection plays an important role in reducing cancer mortality. The current procedure for breast cancer grading is manually performed by pathologists. Breast tissue samples of patients are taken and examined under microscopes. Pathologists grade the tissue samples based on the deviation of the cell structures from normal tissues. A pathologist may have to examine hundreds of slides daily [8], which is a subjective and time consuming process.

Histopathological images (images of biopsy samples) are now available in high resolution and high magnification digital format which can be further processed to extract useful structural information. However, the manual analysis of such huge sets of data can be time consuming [9]. Figure 1-2 is an example of a compressed image of a full size histopathological image. The original size of this biopsy sample was 14,654 μm × 11,026 μm. At a ×40.0 magnification scale, this histopathological image can be represented in digital format with a resolution of 58,630 × 44,216 pixels, and it requires 449,149 Kb of digital data storage.

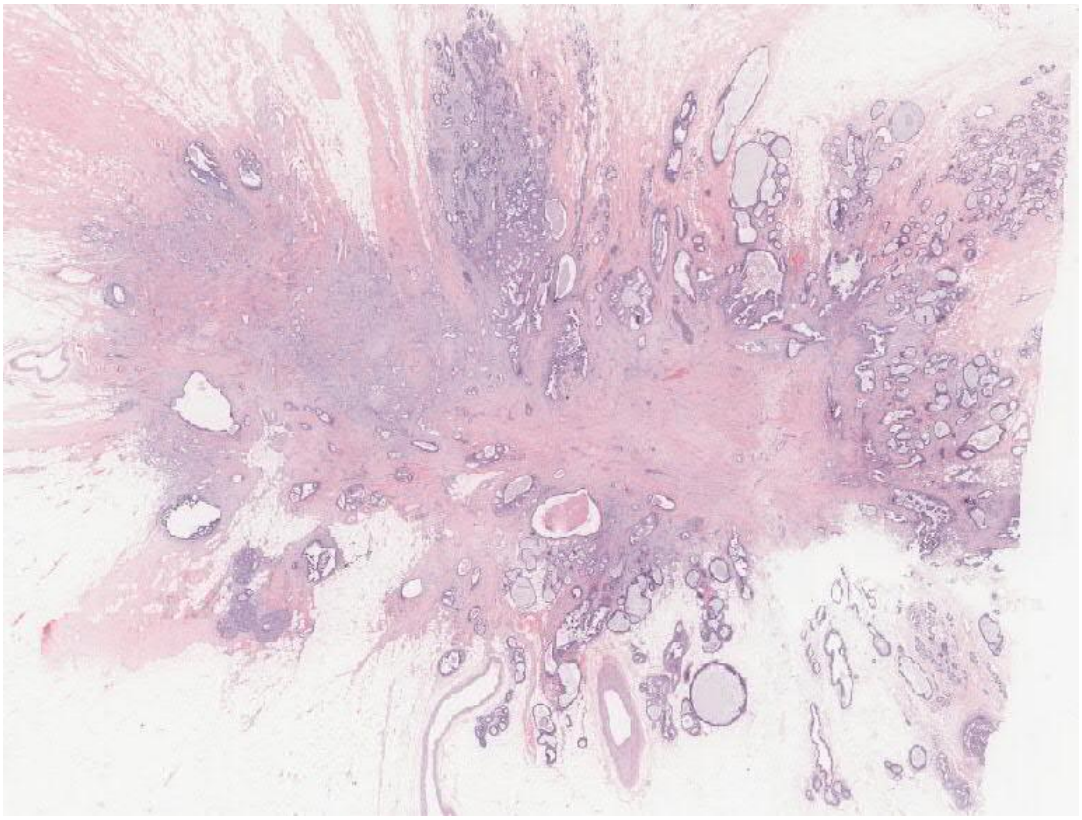

Figure 1-2 A whole slide image at a ×1.0 magnification scale [10]

The medical data used in this research were provided by Image & Pervasive Access Lab (IPAL), Singapore. The research group in IPAL is constructing a "cognitive virtual microscopic framework" for the breast cancer grading system. This framework introduces a "knowledge-driven medical imaging environment"; it can provide a system that is effective, efficient, reliable, and traceable assistance for prognosis [8].

George and Sager showed that tumours can be classified using the multifractal techniques [11]. This research is going beyond George and Sager's research to measure the effectiveness of using multifractal techniques to grade the tissues of breast cancer tumours.

1.2 Objectives

Cell structures have multifractal characteristics that could be directly used for identifying pathological conditions. Multifractal formalism has been developed by many researchers; it has been recently used in the domain of biomedical image processing. Applying multifractal techniques is a novel approach for analysing breast cancer grading. This research aims to explore the relationship between various multifractal measures of cell structures in the tissue samples and the corresponding scores assigned by pathologists.

However, this grading system does not replace the work of pathologists; rather, it provides a pre-screening analysis for them. The system should reduce the workload of pathologists and alert them to the cases that require closer attention.

1.3 Publication

The work of this Master's research has been published in the 26th International Conference Image and Vision Computing New Zealand (IVCNZ 2011). The details of the paper are as follows:

ChiangHau Tay, Ramakrishnan Mukundan, and Daniel Racoceanu. Multifractal Analysis of Histopathological Tissue Images. In *Image and Vision Computing New Zealand. IVCNZ '2011. 26th International Conference*, Auckland, Dec 2011, pp. 80-85

1.4 Thesis Overview

The thesis contains six chapters, and it is presented as follows:

- Chapter 2 outlines the overview of breast cancer grading and summarises the related work developed by other researches in breast cancer analysis.
- Chapter 3 contains the working procedure of multifractal technique and demonstrates the algorithms to calculate the multifractal spectrum. Several applications of multifractal analysis are reviewed in this chapter.
- Chapter 4 presents the outline of the system structure and implementation of this research. The developed methods are fully described and explained.
- Chapter 5 contains the results and the discussion of the implemented methods.
- The conclusions and suggestions for future work are presented in Chapter 6.

Chapter 2:

Background and Literature Survey

The overview of breast cancer diagnosis is presented in this chapter. The methods for evaluating the features of breast cancer grading are summarised.

2.1 Overview of Breast Cancer Grading

Scarff-Bloom-Richardson (SBR) system has been commonly used in the United States since 1957 [12]. Nuclear grading was one of the main focuses in SBR system; however, the effects of tubules have not been considered. In 1998, two European histopathologists, Professor Elston (Professor of Tumour Pathology) and Dr Ellis (Reader of Pathology) modified SBR system into Nottingham Grading System (NGS) [13, 14], which focuses on three criteria: Mitotic Count (MC), Nuclear Pleomorphism (NP), and Tubule Formation (TF). Each criterion contributes 1 to 3 points, and they are added to give a final equivalent grade, as shown in Table 2-1. Both Collage of American Pathologists and World Health Organization recommended NGS for breast cancer grading [15] because NGS introduces more specific criteria [13]. Hence it has become the current standard.

Table 2-1Nottingham Grading System [16]

Overall grade	Equivalent grade	Combined histological grade
Low Grade	I	3-5 points
Intermediate Grade	II	6-7 points
High Grade	III	8-9 points

However, the presence of solely a good grading system does not guarantee the reliability of pathology results. Pathologists could analyse these medical tests based on their experience and subjective opinions [17]; hence the grade of a cancer case could have a low agreement between pathologists [18]. Dunne and Going carried out a case study to analyse the breast cancer grading ranked by different pathologists. The results showed that differences might arise from individual decision on nuclear grading in breast carcinoma. Professional pathologists specialised in breast cancer tended to grade higher pleomorphism scores than non-specialists [19]. Huang et al. also noticed that different doctors could give different diagnosis for the same biopsy samples. Although it is not a usual case, a doctor can make different prognosis on a same medical test at different times [20].

Therefore, a computer-aided system is required to provide a standard and quantitative measurement for breast cancer assessment. Currently, many computer science researchers focus their studies on the algorithms for automatic and semi-automatic breast cancer grading system based on the NGS criteria. These researches aim to perform the time-consuming pre-screening job, and to provide reliable information for pathologists for breast cancer diagnosis.

2.2 Mitotic Count Scoring

The scoring for Mitotic Count (MC) calculates the number of mitotic cells found in a high-power field (HPF). HPF is a term used in microscope; it refers to the visible area under maximum magnification power of a microscope. The diameter of the "field of view" varies between microscopes [21]; the numbers of mitotic count related to NGS in 10 HPF is shown in Figure 2-1.

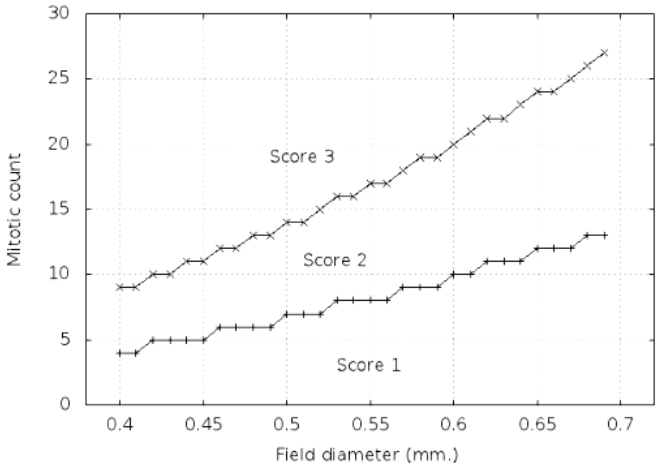

Figure 2-1 The number of mitotic count per 10 HPF by the field diameter [22]

Mitosis detection is challenging because the mitotic cells are small and have different shapes. The mitosis has four main stages determined by the shapes of the nucleus (Figure 2-2): prophase, metaphase, anaphase, and telophase [22, 23]. A mitotic cell refers to the daughter cells form at metaphase, anaphase, and telophase; whereas cells at prophase are not considered as mitotic cells [22]. Different circumstances make the process of detecting mitotic cells even more challenging.

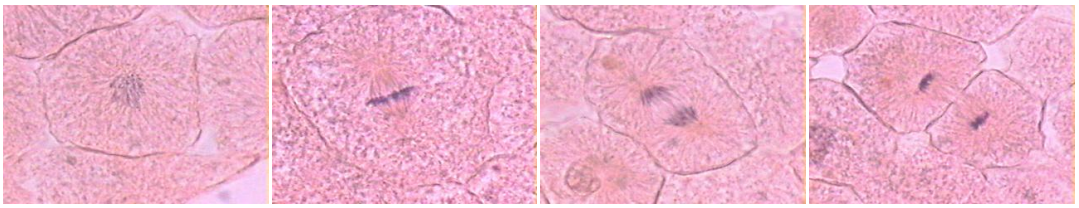

(a) (b) (c) (d)

Figure 2-2 Four stages of mitosis: (a) prophase (b) metaphase (c) anaphase (d) telophase [22]

Kamen et al. studied an automated recognition of mitosis in tissue sections in 1984. The aim of their study was to maximise the number of detected mitotic cells. Potential mitotic cells were selected by using global and local segmentation techniques. The global threshold separated darker elements (mitotic cells, artefacts, and inflammatory cells) from the background pixels which were brighter; the local threshold then performed a second sieving process to the darker elements. Contour features were applied on classification of mitotic cells and non-mitotic cells. This method had a result of a large net loss of 37% mitotic cells, and 5% of non-mitotic cells were mistaken as mitotic cells [24]. Low image quality and unsuitable staining preparation were the cause of the unsatisfactory result [25].

In 1993, Kate et al. used region growing method to segment mitotic cells [25]. The method was able to correctly classify 81% of the mitotic cells, while obtaining 30% of false positive rate. A mitotic cell has the darkest pixel in the cell region; a seed can start from the darkest pixel and expand to the neighbouring pixels which have similar intensity properties. During the classification process, Kate et al. analysed contour features for detecting the hairy feature of mitotic cells and "optical density measurements" to observe the object feature of mitosis. During the training stage, the semi-automated method required the users' input to classify mitotic cells and non-mitotic cells. The system then learned from the first training experiment and re-evaluated the entire training set. The result of the fully automatic method was not ready for clinical practice, but the semi-automated method could be used as a pre-screening device.

The improvement work from Kate et al. was carried on by Beliën et al. in 1997. They investigated the effects of spatial resolution on the results of automatic mitosis recognition. The process was slow due to hardware limitation back then. They suggested that higher resolution in breast cancer sections can improve the resolution of the hairy features of mitotic cells, but the irrelevant artefacts formed during the preparation of the microscope slides also gained better resolution. The combination of the "optical density features" and "minimal grey value feature"

worked better at higher spatial resolution. They managed to reduce the false negative rate from 19% [25] to 5-8%, but the false positive rate was still unsatisfactory, ranging from 22% and 42% [26].

In 2008, Dalle et al. classified potential mitotic cells by matching the shapes and intensity properties of test cells with those of mitotic cells. They captured a set of histological image frames, each of 1,024 × 1,280 pixels, from a patient's sample. The average count of mitotic cells over all image frames was calculated and multiplied by a factor of 10. NGS states that the MC score is evaluated by the total mitotic cells found from 10 randomly selected cell regions; hence the multiplication factor was introduced. This method was tested and compared with the results analysed by a pathologist. Four out of six grading results agreed with the expert, one was overestimated, and one was underestimated [27].

Segmentation of mitotic cells is complicated; researchers found that mitotic cells are small and can be easily confused with artefacts. However, mitotic cells have unique hairy features which make them detectable.

2.3 Nuclear Pleomorphism Scoring

Nuclear Pleomorphism (NP) score focuses on the shapes, chromatin distribution, and sizes of cell nuclei. The score of NP is listed in Table 2-2; one of the key factors in NP scoring is cell nuclei detection. Many methods have been proposed for cell nuclei segmentation, such as thresholding [28], watershed [29], morphological operation [30], and generic features [31]. However, only the methods developed for breast cancer are reviewed in this section.

Table 2-2NGS for Nuclear Pleomorphism [16]

Score	Nuclear Pleomorphism scoring
1	Small regular uniform cells
2	Moderate nuclear size and variation
3	Marked nuclear variation

Cosatto et al. described a robust method for measuring the size of neoplastic nuclei. They used an Active Contour Model (ACM) to segment cell nuclei and classified them with a Support Vector Machine (SVM). To remove colour variations, Cosatto et al. converted a colour image into CMY (cyan, magenta, and yellow) colour space. Then, a 2D Difference of Gaussian filter was applied to find the malignant cells, which are always larger than a normal nucleus. Elliptical nuclei, which have symmetric shapes, could be detected with a Hough transform operation. The outline of an elliptical nucleus could be approximated with ACM. The SVM classifier was trained to analyse the shape, texture, and fitness of the outline of the malignancies. Cosatto et al. showed that their result obtained 92% true positive and 20% false negative in classifying malignant and benign cells [32]. Although their method had yet to provide actual NP grading, accurately measuring the sizes of malignant cells is a key parameter in NP scoring.

Dalle et al. applied Gaussian function to model the probability distributions of the colours of cells used for NP scoring. Each NP score had a global Gaussian model which defined the mean and covariance matrix of the colours in its corresponding type of cells; these models represented three types of chromatin distribution: homogeneous, moderate, and clumped. On the other hand, every detected cell had its own Gaussian model which was then compared with the global model. A cell was denoted as a particular type of cell when its colour distribution was similar to that global model. Six medical samples were tested, where three of them were Score 2 and three were Score 3. This method had correctly classified all medical tests with Score 2 and only one for Score 3. The other two Score 3 cases were underestimated to be Score 2. Dalle et al. were confident to their result because a pathologist only needs enough numbers of cell regions which are Score 2 and Score 3 to make an assessment [27].

Unlike other existing methods that tended to detect every cell in the image, Dalle et al. showed that NP scoring could be achieved by analysing the critical cell nuclei. Epithelial cells which they defined as the critical cell nuclei always crowd

together and have larger shape than inflammatory cells and mitotic cells. Dalle et al. first detected a region of interest (ROI), described in [27], and applied a gamma correction to the red channel of the ROI. Gamma correction can change the brightness and the ratio of red, green, and blue of an image; it highlighted the cell nuclei from the background. Then, a threshold operation was applied to separate cell nuclei and background. Nearby clusters could be connected with a dilation operation, while the isolated clusters remained isolated. After that, an erosion operation was applied to separate connected clusters. A candidate critical cell nucleus was large and had close-by critical cell nuclei. The measurement for NP score was based on the size, shape and, texture of the critical cell nuclei.

Overall, Dalle et al. found that 7.84% of cell nuclei were incorrectly classified. Besides, they also found that the number of critical cell nuclei was crucial for classification (Figure 2-3). To minimise the error rate to 7.8%, at least 40 cell nuclei were required for Score 3. Similarly, NP Score 2 required a minimum of 50 cell nuclei to keep the error rate below 12%. This method used less processing time while maintaining a good accuracy of the classification [33].

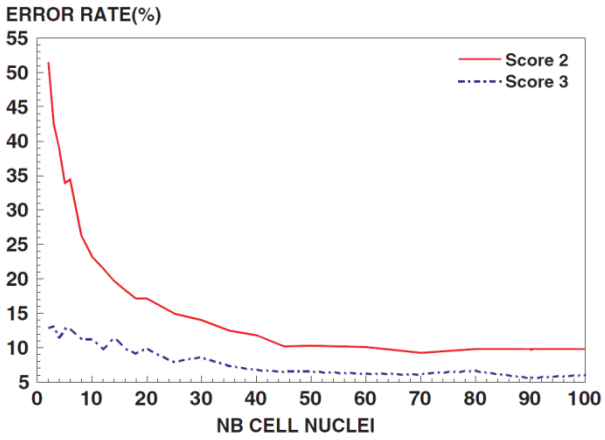

Figure 2-3 Impact of number of critical cell nuclei to the error rate of NP scoring [33]

A breast cancer detection method which combined neural network as a classifier tool was presented by Singh et al. They classified malignant breast tumor into three types: Type 1, Type 2, and Type 3. The adaptive thresholding method and watershed algorithm were first applied for cell nuclei segmentation. In order to

separate stained tissue and background, Singh et al. assumed that local variations occurred during the preparation did not affect the measurements. Once the individual cells had been detected and segmented, the neural network classified malignant and benign nuclei based on eight different nucleus characteristics. The result of a histopathological image after applying the method is shown in Figure 2-4. The proposed system gave an overall accuracy of 95.80%, which is relatively high for breast tumour screening [34].

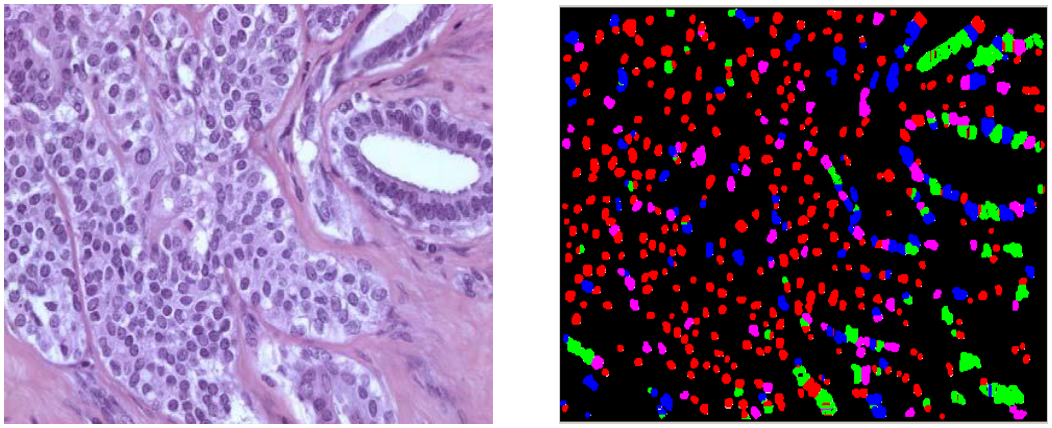

(a) (b)

Figure 2-4 Example of (a) a histopathological image (b) results where red represents type 3 malignant, magenta represents type 2 malignant, blue represents type 1 malignant, and green represents benign object [34]

The score of NP is based on the deviation of cell nuclei in an invasive breast tissue region. Although there are many different methods developed for cell nuclei segmentation, literatures agreed that the performance of NP scoring is dependent on accurate segmentation of cell nuclei.

2.4 Tubule Formation Scoring

Tubules refer to the white blobs (lumina) surrounded by a continuous string of cell nuclei [35]. The scoring of Tubule Formation (TF) measures the percentage of tubules present in a histopathological image. NGS for TF score is shown in Table 2-3.

Table 2-3NGS for Tubule Formation [16]

Score	Tubule Formation scoring	
1	Majority of tubule	(> 75%)
2	Moderate degree of tubule	(10-75%)
3	Marked nuclear variation	(< 10%)

Petushi et al. showed that the microstructure existed in a histological image could be modelled; this model could localize TF via segmentation and machine learning classification of the cell nuclei [36, 37]. The grading for each section image could be distinguished by measuring the average distances between the centroids of closest nuclei in a high density region. Besides, Petushi et al. also noticed that there was a correlation between tubules and cancer cells. As shown in Figure 2-5, a section image which had majority nuclei of cancer cells contained a fewer number of tubules. Based on these texture features, the section image could be classified as Score 1 and Score 3. The overall results had shown that this method worked well in Score 1 and 3 cases, but the result of Score 2 was less satisfactory [36].

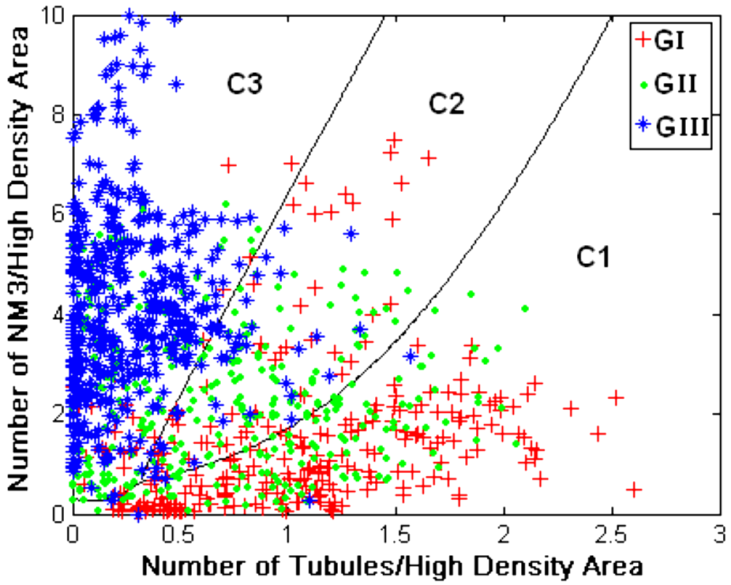

Figure 2-5 Scatter plot for the classification of section images using the number of cancer cells and tubules as features parameters; C1, C2, and C3 are the quadratic classifier which associated with G I, G II, and G III (Score 1, 2, and 3) [36]

A “rules-based system modelling” that transformed medical concepts into computer vision concepts were developed by Tutac et al. Their model was developed for a full NGS diagnosis tool, but only the development for TF is described in this section. Tutac et al. defined “*DarkCellsCluster*” as a symbolic rule which contained a group of adjacent cells with intensity value setup between very dark and white limits. The pathological criterion TF could be satisfied when the symbolic rule for TF “*WhiteBlobs*” were included in the “*DarkCellsCluster*”. The local grading TF (single criterion of NGS) was calculated with the ratio of TF ROI over the area of “*DarkCellsCluster*”. Among six breast cancer tests which composed to 5,600 frames, this method obtained 11% testing errors for TF scores. Although the average single component error (including MC and NP) was 11%, the global grading errors of NGS was 0% [35]. As a result, the final NGS grade was not affected by single component errors.

Dalle et al. used a morphological operation to segment tubules in a low resolution global image. A blob structure containing fat or lumina region was considered a TF. Subsequently, the blob structures presented in the neoplasm could be found with the morphological filling operation. The ratio of the section occupied by tubules and the total area of cells in the image frames denoted the TF score. However, the results based on this method tended to score lower than the pathologist’s. Dalle et al. explained that their system had slightly stricter measurements [27].

All researchers agreed that localising the white blobs surrounded by cell nuclei was the first step to analyse TF score in the biopsy slides. Hence, it was an important aspect during the development of this research.

2.5 Summary of Literature Review

NGS is the benchmark for breast cancer analysis, where MC, NP, and TF are used for prognostic information, as shown in Figure 2-6. Automatic and semi-automatic methods for breast cancer diagnosis have been developed by many researchers. Most of the methods were proposed to address a single NGS criterion. Only a few researches focused on complete breast cancer diagnosis tools which had an equivalent grading result with NGS. A brief description of how literatures approached NGS parameters is summarised in Table 2-4.

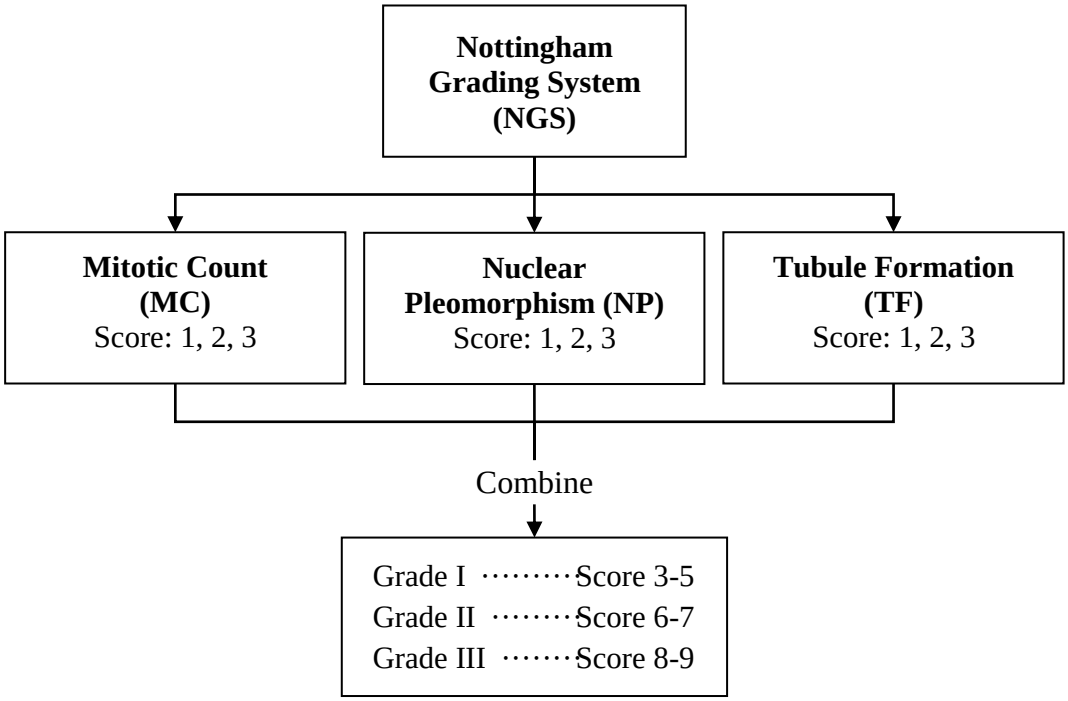

Figure 2-6 General schematic of Nottingham Grading System

Table 2-4Summary of the evaluations for NGS parameters

NGS criterion	Features	Methods		Measurement
		Segmentation	Classification	
MC	− Darker colour − Hairy feature	− Thresholding − Growing method	− Contour feature	− Count the number of mitotic cells in 10HPFs
NP	− Larger than normal nucleus	− Active Contour Model − Adoptive thresholding − Watershed method	− Support Vector Machine − Gaussian model − Neural network	− Based on size, shape, and texture
TF	− White blobs surrounded by cell nuclei	− Morphological operation	− Machine learning	− Calculate the area ratio of tubules and the cell region

Chapter 3:

Multifractal Analysis

Biomedical image processing involves segmentation, automatic recognition, and classification of the image features. Image analysis for tissue and cell images is complicated and challenging. The shapes of the tissues and cells are irregular; they are different in size and have different orientations. Hence, performing such complex tasks requires more advanced techniques than traditional image analysis methods [38].

Natural objects exhibit statistical self-similarity, a repetition of form over a variety of scales [39]. Tissues and cells have the feature of self-similarity with varying degrees of randomness, so they belong to a class of objects known as multifractal [40]. Multifractal refers to configurations with different observed degree of fractal dimension, an attribute that describes the level of self-similarity [41]. Many researchers conclude that multifractal technique is an effective and robust tool for image segmentation and interpretation [38, 42-44]. Therefore, multifractal technique has been widely applied in biomedical image processing.

This chapter includes the process of calculating Hölder exponent, denoted as α-value, the description of variation in local density of the image. Moreover, the types of multifractal measures are illustrated in detail with the properties of each measure. The computation of multifractal spectrum, which describes the fractal dimension of the image, is demonstrated. In addition, the applications of

multifractal techniques on biomedical image processing are reviewed in Section 3.5 of this chapter.

3.1 Hölder exponent

A digital image is numerically represented by a two-dimensional array with a configuration of *M* rows and *N* columns; each index, known as pixel, contains a unique property. Depending on the types of digital image, the unique property of a pixel can be different. For example, the pixels of a binary image have binary values, the pixels of a greyscale image have intensity values, and the pixels of a colour image have red, green, blue, and alpha values.

Multifractal describes the fractal properties of an image using an intensity-based measure within the neighbourhood of each pixel. In an example of a greyscale image, each pixel in the image has an intensity value which is represented as a multi-level of grey value. These grey values are linearly interpolated from black to white, ranging from 0 to 1. The local singularity coefficient, also known as the Hölder exponent [38, 44, 45], or α-value, reflects the local behaviour of a function $\mu_p(w)$, described in Equation 3.1, around the pixel [46]. The window of size *w*, is centred at the pixel *p*, as shown in Figure 3-1. The variation of the intensity measure with respect to *w* can be characterised as follows:

$$\mu_p(w) = Cw^{\alpha_p} \tag{3.1}$$

$$w = 2i + 1, \quad i = 0,1,2, \dots, d \tag{3.2}$$

$$\log(\mu_p) = \alpha_p \log(w) + \log(C) \tag{3.3}$$

where *C* is an arbitrary constant. In Equation 3.1, α_p is an unknown quantity that needs to be estimated using the measured values of μ_p. In Equation 3.2, *d* is the total number of windows used in the computation of α_p. The value of α_p can be estimated from the slope of the linear regression line in a log-log plot where $log(\mu_p)$ is plotted against $log(w)$. Furthermore, the slope of a linear regression line is calculated with given *n* sets of *X* and *Y*, by:

$$linear\ regression = \frac{n \cdot \sum(XY) - \sum X \cdot \sum Y}{n \cdot \sum X^2 - \sum X \cdot \sum X} \tag{3.4}$$

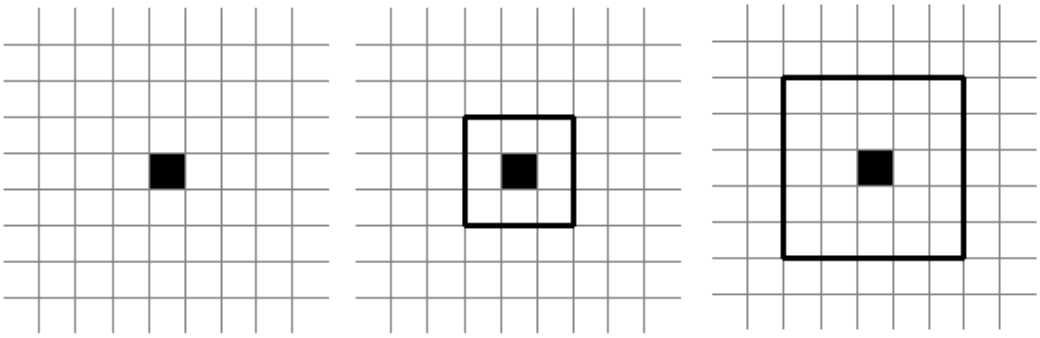

Figure 3-1 Window size of w = 1, 3, 5 at the black centre pixel, p (reproduced from [40])

In Nilsson's research on multifractal-based image analysis [47] , different neighbouring shapes can affect the estimation of the local dimension. He applied three different shapes (square, rhombus, and round) on the calculation. For a homogeneous region, only the square window had a regression slope of two. On the other hand, I. Reljin and B. Reljin stated that "the measure is regular" when the α-value is approximately two, for instance, "the probability of the signal changes is small" [44]. Based on this property, Nilsson determined square window to be the natural choice, and it was used in this research.

An image contains a range of positive, finite α-values, namely the α-range, with a minimum value of α_{min} and a maximum value of α_{max}. Under some circumstances, the minimum α-value could be zero. These α-values are stored in a two-dimensional matrix where each element corresponds to the pixel's location on the original image. The resulting image given by computing the local singularity of the original image is called the α-image.

As the computation for the Hölder exponent requires a window surrounding each pixel, a problem will occur when computing the pixels around the edge of the image. A border of width w (the width of corresponding square window) is assigned to address this issue. The pixels located at the border will not be present in the image, but the intensity values are included in the calculation of Hölder exponents of their inner neighbouring pixels. Figure 3-2(b) shows that only the Hölder exponents of pixels inside the black frame will be calculated

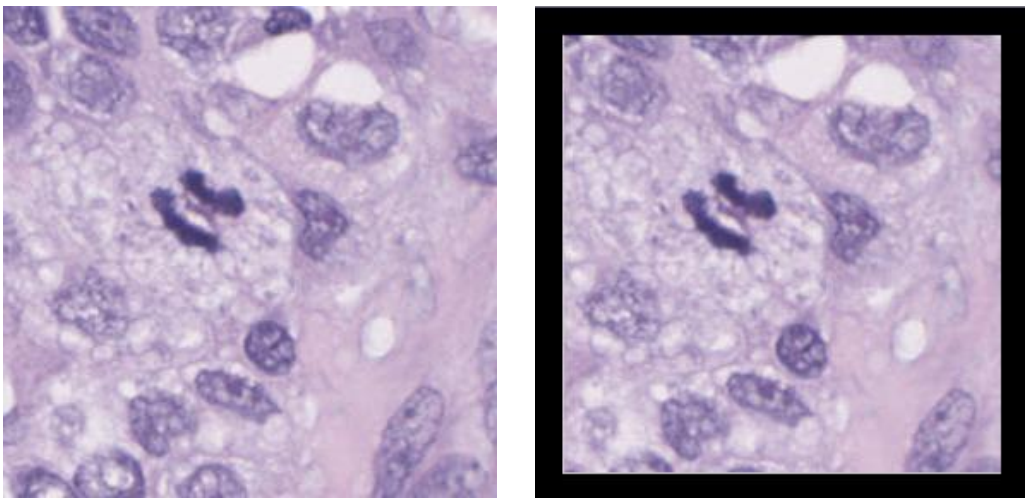

(a) (b)

Figure 3-2 The (a) original image (b) border for calculating multifractal measure

3.2 Multifractal Measures

There are four common types of intensity measures in multifractal analysis: maximum measure, inverse-minimum measure, summation measure, and Iso measure [38, 48, 49].

The function of a multifractal measure is denoted as $\mu_w(m, n)$. Let $g(k, l)$ represent the intensity value at pixel (m, n), and Ω be the set of all pixels within the measured neighbourhood of a square window size w.

Since the α-value is always greater than or equal to zero, a pixel which is not involved in the calculation is denoted as background and is assigned with a negative α-value.

3.2.1 Maximum measure (max measure)

In the max measure, as shown in Equation 3.5, $\mu_w(m, n)$ represents the maximum intensity value within the square region. A problem may occur if all pixels are completely black with an intensity value of exactly 0. This may cause mathematical error for computing $log(0)$. To avoid this error, completely black pixels are treated as background and are neglected in calculations of max measure.

$$Maximum: \mu_w(m,n) = \max_{(k,l)\in\Omega} g(k,l) \tag{3.5}$$

3.2.2 Inverse-minimum measure (inv-min measure)

The minimum measure finds the minimum intensity value and assigns it to $\mu_w(m, n)$. Nilsson revealed that minimum measure was not reliable [47]; hence, Hemsley suggested the inverse-minimum measure which takes the positive difference between $\mu_w(m, n)$ and 1 (Equation 3.6) [40]. However, this may cause another mathematical error when every pixel is completely white, with intensity value of exactly 1. To prevent computing $log(0)$, completely white pixels are treated as background and are ignored in calculations of inv-min measure.

$$Inverse - minimum: \mu_w(m,n) = 1 - \min_{(k,l)\in\Omega} g(k,l) \tag{3.6}$$

3.2.3 Summation measure (sum measure)

Sum measure sums all pixel intensities in the neighbourhood. Similarly if all pixels are completely black, then Equation (3.7) will encounter error for calculating $log(0)$. Therefore, completely black pixels are treated as background and will not be considered in calculations of sum measure.

$$Summation: \mu_w(m,n) = \sum_{(k,l)\in\Omega} g(k,l) \tag{3.7}$$

3.2.4 Iso measure

Iso measure, as illustrated in Equation (3.8), counts the number of pixels in the neighbourhood which have a similar intensity values to the centred pixel. If the centred pixel is the only pixel with unique intensity in the region, then $\mu_w(m, n)$ is 1. Since the probability that the pixels in a neighbourhood to have an identical intensity value is very low, the Iso measure can be modified to accept a 5% degree of accuracy [40]. This adjustment allows more pixels that have similar intensity values to the centred pixel to be considered in the multifractal measurement.

$$Iso: \mu_w(m,n) = \#\{(k,l)|g(m,n) \cong g(k,l), (k,l) \in \Omega\}, \quad \text{where \# is the number of pixels} \tag{3.8}$$

3.3 The α-image

The results of using different multifractal measures are illustrated in Figure 3-4, and the original greyscale image is shown in Figure 3-3 for comparison. The α-range for each measure is different: [*0.0000, 0.4808*] for max measure, [*0.0000, 0.9354*] for inv-min measure, [*1.7917, 2.3315*] for sum measure, and [*0.0000, 2.1694*] for Iso measure. For display purpose, the original image in Figure 3-3 and α-images in Figure 3-4 are normalised to [*0.0, 1.0*], black to white. Besides, the α-histogram for each multifractal measure shows that the distribution of α-values has a bell-shaped curve, and is skewed and translated along the α-axis respectively.

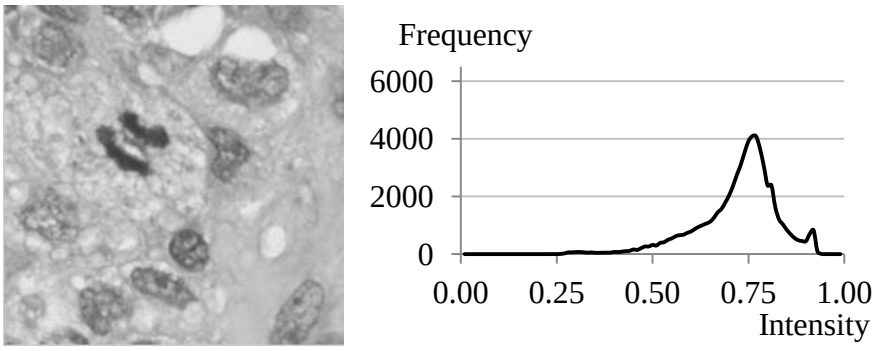

Figure 3-3 The greyscale image (left) and its corresponding intensity histogram (right)

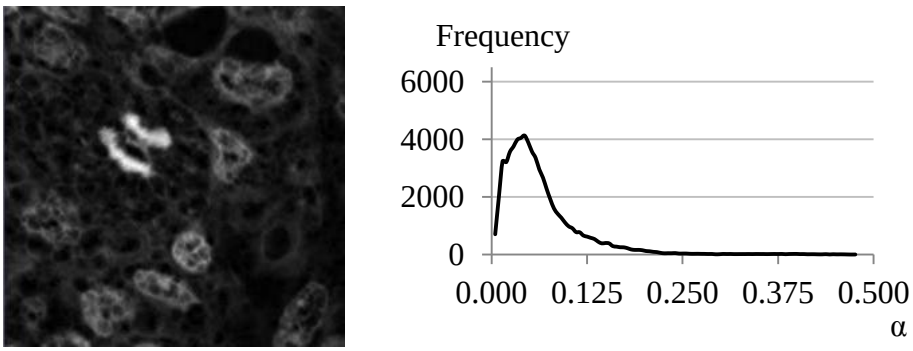

(a) Sum measure

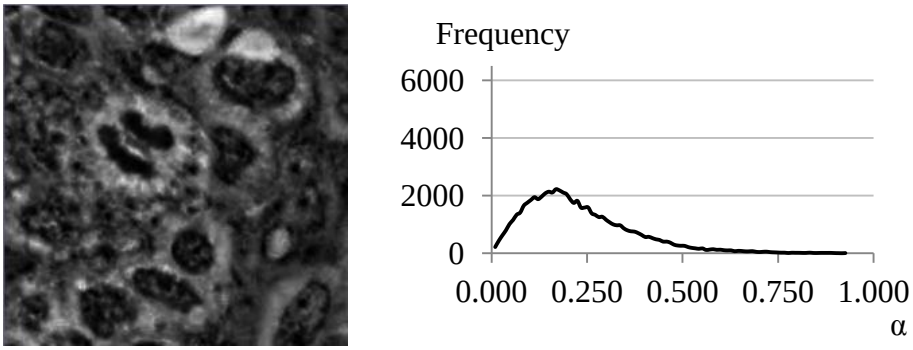

(b) Inv-min measure

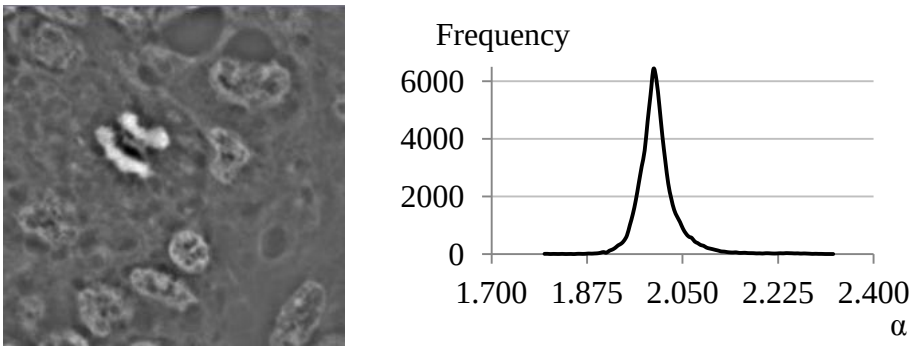

(c) Sum measure

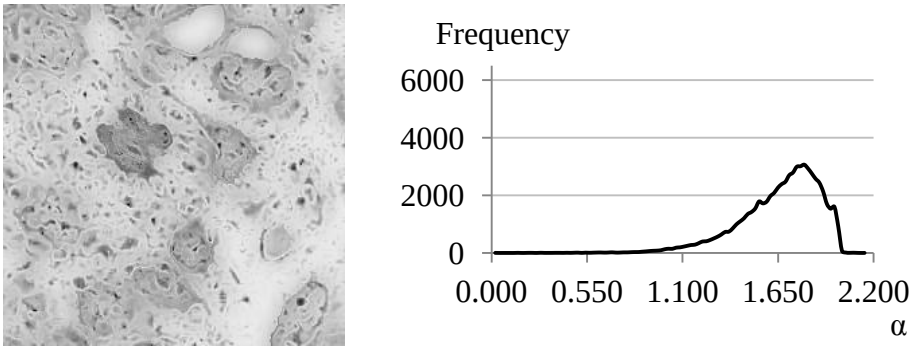

(d) Iso measure

Figure 3-4 The α-image (left) and its corresponding α-histogram (right)

The binary images for each multifractal measure displayed in Figure 3-5 are produced by thresholding the α-image at different α-series. These α-series represent every quarter of the α-ranges. Only the pixels with α-values within the particular α-series are assigned as ones and all the others as zeros. For a particular α-series and multifractal measure, some of the tissue substances are more observable in the binary image. Hence, image features can be detected in a particular range of the α-values. This is a unique feature of multifractal analysis. More details are discussed in Chapter 4.

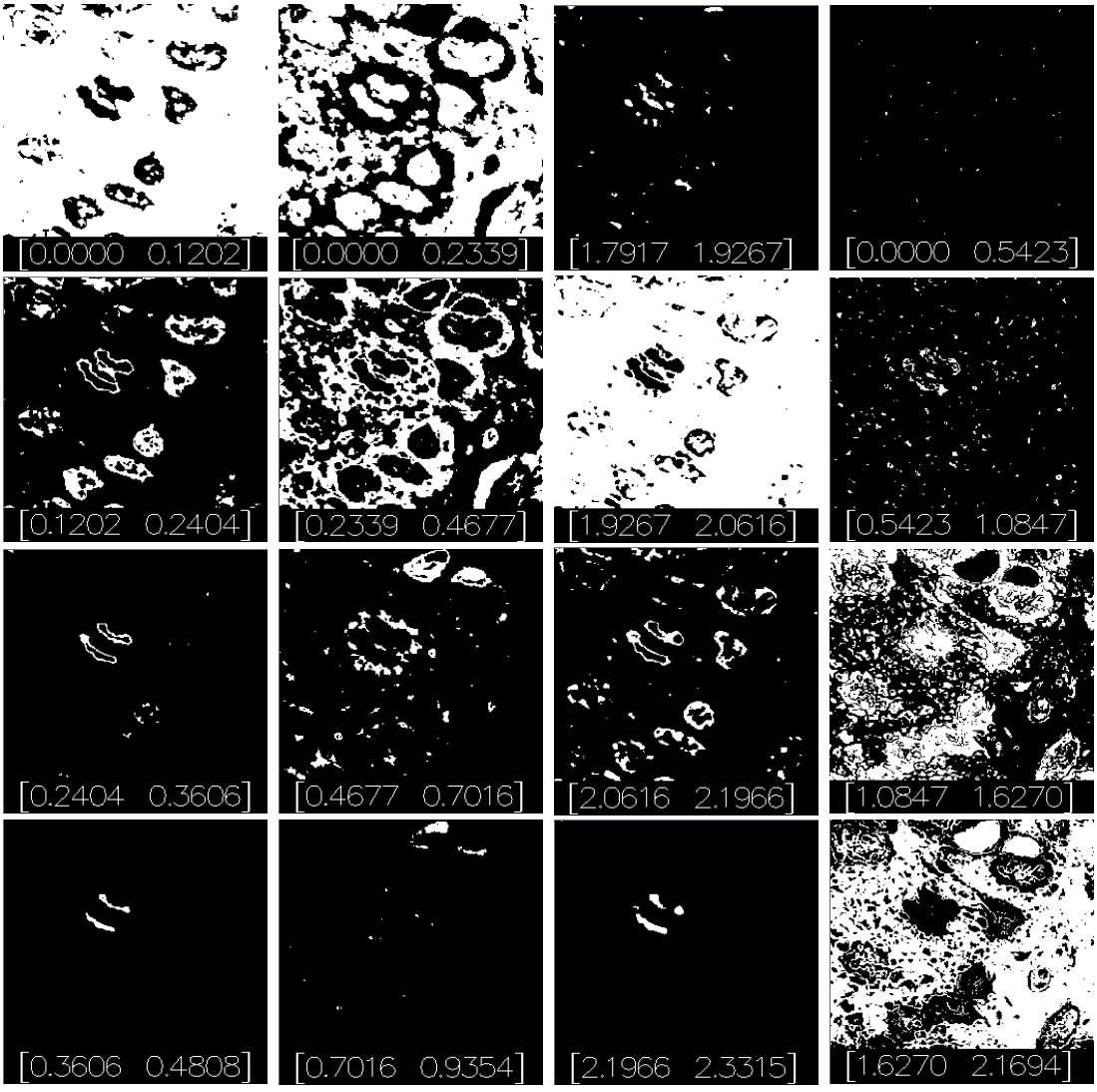

(a) max measure (b) inv-min measure (c) sum measure (d) Iso measure

Figure 3-5 The binary images produced by thresholding the α-image at different α-series

3.4 The Multifractal Spectrum

The following step of multifractal analysis is the calculation of fractal dimension where sets of points have the same singularity coefficient α. Multifractal spectrum characterises the intensity of the image; it is a unique description of the geometric property of fractal dimension. Besides, it can be presented by plots of fractal dimension against α-value, as shown in Figure 3-6. The resulting discrete plot (Figure 3-6 (a)) can be displayed as a continuous function, as shown in Figure 3-6 (b). Clearly, the latter presentation is easier to read and understand; hence, multifractal spectrum is presented as continuous functions in this thesis.

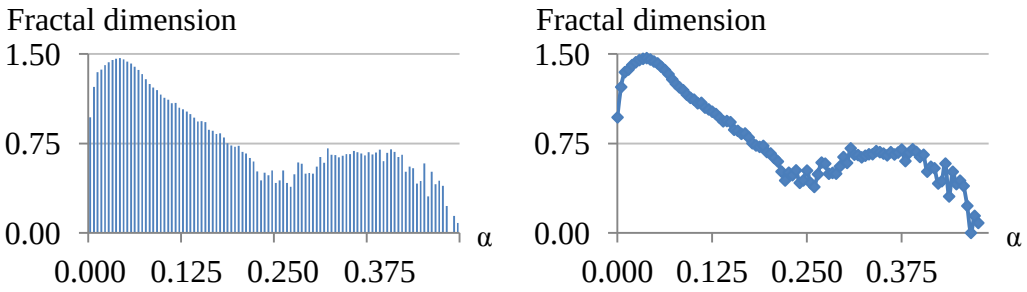

Figure 3-6 Multifractal spectrum: (a) actual form (b) continuous form

3.4.1 Fractal dimension

Theiler demonstrated that fractal dimension can be estimated using a box-counting method, a correlation algorithm, or a fixed-mass ball technique [50]. Box counting is one of the most commonly used methods for calculating fractal dimension [41, 45, 48] because it is simple and easy to implement. For an N by N image, box counting only requires an average $O((N^2/2)\log N)$ computation time [49], while maintaining a good estimation for the image's fractal dimension [51].

3.4.2 Box-counting method

Box-counting method counts the number of boxes, $n(\varepsilon)$ with box size ε, that contain pixels with α-values within the α-interval $[\alpha_i, \alpha_{i+1}]$, as shown in Figure 3-7. The α-intervals are obtained by subdividing the range of α-values into a pre-specified number of sub-intervals. In this research, the number of sub-intervals

is 100. Referring to Equation 3.9, the fractal dimension, $f(\alpha)$, can be obtained by calculating the slope of linear regression line of the plot of $log(n(\varepsilon))$ against $log(\varepsilon)$. The size of box ε starts from half the size of the input image of size N, and recursively reduces until 1, as shown in Equation 3.11.

$$f(\alpha) = \frac{\log(n(\varepsilon))}{\log(\varepsilon)} \tag{3.9}$$

$$\left.\begin{array}{c} n(\varepsilon) = \#\{\Omega | \alpha_i \leq \alpha(k,l) < \alpha_{i+1}, (k,l) \in \Omega\} \\ \text{where \# is the number of pixels} \end{array}\right\} \tag{3.10}$$

$$\varepsilon = \frac{N}{2^k} \ , \ k = 1,2..t \ , \ t \leq \frac{\log N}{\log 2} \tag{3.11}$$

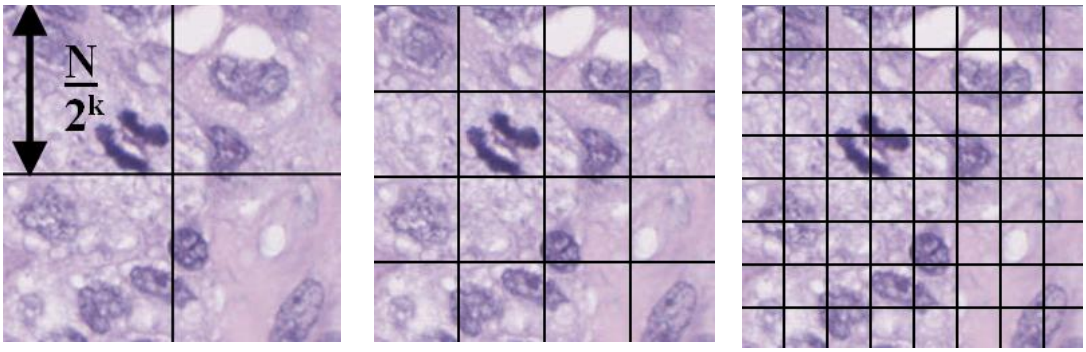

(a) ε = 128 (b) ε = 64 (c) ε = 32

Figure 3-7 Box-counting method that uses different box sizes ε

3.4.3 Polynomial curve fitting

As mentioned earlier, multifractal spectrum is a discrete function of α-values; it can be expressed as a continuous function. Representing a large set of $f(x)$ values by a continuous polynomial curve (see Figure 3-8 (b)) is useful for obtaining a small set of coefficients that we can use for comparing or matching two multifractal spectra. A general n-th order polynomial equation, $f(\alpha)$, is an expression which consists of sets of variables and constants, defined as follow:

$$f(x) = a_n x^n + a_{n-1} x^{n-1} + \cdots + a_2 x^2 + a_1 x + a_0 \tag{3.12}$$

where x is the variable, n is a non-negative integer, and a_0, a_1, a_2, …, a_n are constant coefficients.

Suppose the data points of a multifractal spectrum are the m-th pairs of vectors, (x_1, y_1), (x_2, y_2), …, (x_m, y_m), where x is the value of α and y is the value of $f(\alpha)$, then a least squares method can fit the spectrum to a polynomial function, described as follow:

$$\Pi = \sum_{i=1}^{m} [y_i - f(x_i)]^2 = minimum \tag{3.13}$$

$$\Pi = \sum_{i=1}^{m} \left[y_i - (a_n x_i^n + \cdots + a_2 x_i^2 + a_1 x_i + a_0)\right]^2 \tag{3.14}$$

$$\left.\begin{aligned} \frac{d\Pi}{da_0} &= \sum_{i=1}^{m} \left[y_i - (a_0 + a_1 x_i + a_2 x_i^2 + \cdots + a_n x_i^n)\right] = 0 \\ \frac{d\Pi}{da_1} &= 2\sum_{i=1}^{m} x_i \cdot \left[y_i - (a_0 + a_1 x_i + a_2 x_i^2 + \cdots + a_n x_i^n)\right] = 0 \\ &\vdots \\ \frac{d\Pi}{da_n} &= 2\sum_{i=1}^{m} x_i^n \cdot \left[y_i - (a_0 + a_1 x_i + a_2 x_i^2 + \cdots + a_n x_i^n)\right] = 0 \end{aligned}\right\} \tag{3.15}$$

$$\left.\begin{aligned} \sum_{i=1}^{m} y_i &= a_0 \sum_{i=1}^{m} 1 + a_1 \sum_{i=1}^{m} x_i + \cdots + a_n \sum_{i=1}^{m} x_i^n \\ \sum_{i=1}^{m} x_i y_i &= a_0 \sum_{i=1}^{m} x_i + a_1 \sum_{i=1}^{m} x_i^2 + \cdots + a_n \sum_{i=1}^{m} x_i^{n+1} \\ &\vdots \\ \sum_{i=1}^{m} x_i^n y_i &= a_0 \sum_{i=1}^{m} x_i^n + a_1 \sum_{i=1}^{m} x_i^{n+1} + \cdots + a_n \sum_{i=1}^{m} x_i^{2n} \end{aligned}\right\} \tag{3.16}$$

The unknown coefficients a_0, a_1, …, a_n can be obtained by solving the linear equations in Equation 3.16 with a Gaussian Elimination.

An example of polynomial fitting with a sixth order polynomial equation for the multifractal spectrum (in Figure 3-6) is demonstrated in Figure 3-8. The equation is given to be:

$$f(\alpha) = 63.1506\alpha^6 + 650.6059\alpha^5 - 1340.2903\,\alpha^4 + 821.3956\alpha^3 - 191.4751\alpha^2 + 12.2804\alpha + 1.1769 \quad (3.17)$$

with a correlation coefficient of 0.9650.

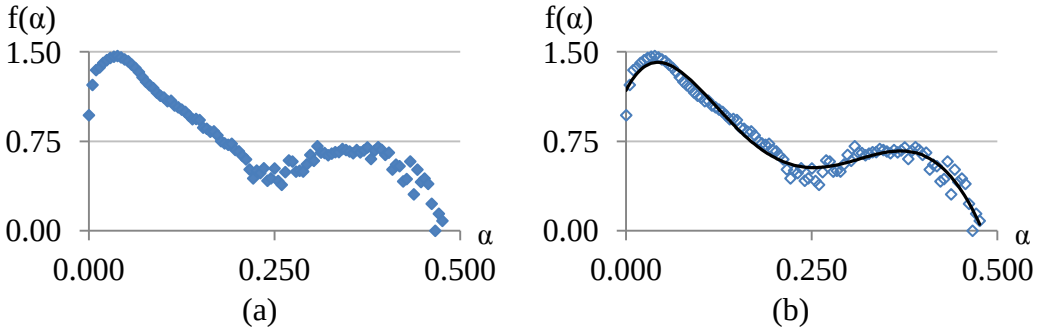

Figure 3-8 Multifractal spectrum: (a) original discrete function (b) sixth order polynomial equation

3.4.4 Adjusting the α-range

Noise often exists in digital images. A simple equalisation can minimise the problem. As discussed in Section 3.3, the α-histogram in Figure 3-4 shows that all α-values of the image are distributed along its unique α-range, from α_{min} to α_{max}. Each α-interval in the α-histogram has its own count for the number of pixels with particular α-values. The α-value can be treated as noise when its occurrence in corresponding α-interval is below a certain threshold. In this research, the threshold is set to 65, which is 0.1% of the total number of pixels in a 256×256 size image. The new α-range can be modified by neglecting α-values of occurrence below the threshold.

As shown in Figure 3-9, the α-image based on the summation measure has α-values distributed between 1.79 and 2.33. The bold boxes in the figure show the α-intervals where the α-values have occurrence below the threshold of 65. These α-values are treated as noise and are excluded; the modified α-range is now from

1.90 to 2.13. Note that the α-values which located in the middle of the histogram are not treated as noise even if its occurrence in corresponding α-interval is below the threshold.

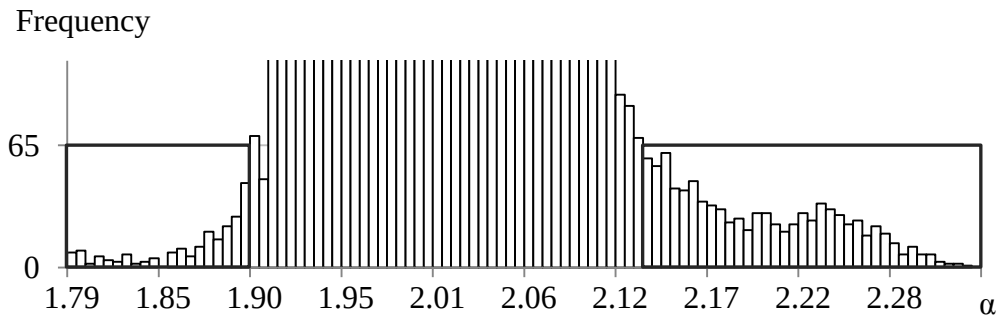

Figure 3-9 The magnified portion of the α-histogram of the sum measure from Figure 3-4

The effect of adjusting the α-range and re-sampling the spectrum is demonstrated in Figure 3-10. It should be noted that the multifractal spectra have similar trends as the α-histograms show in Figure 3-4. All further calculations on multifractal spectrum will include the α-range adjustment.

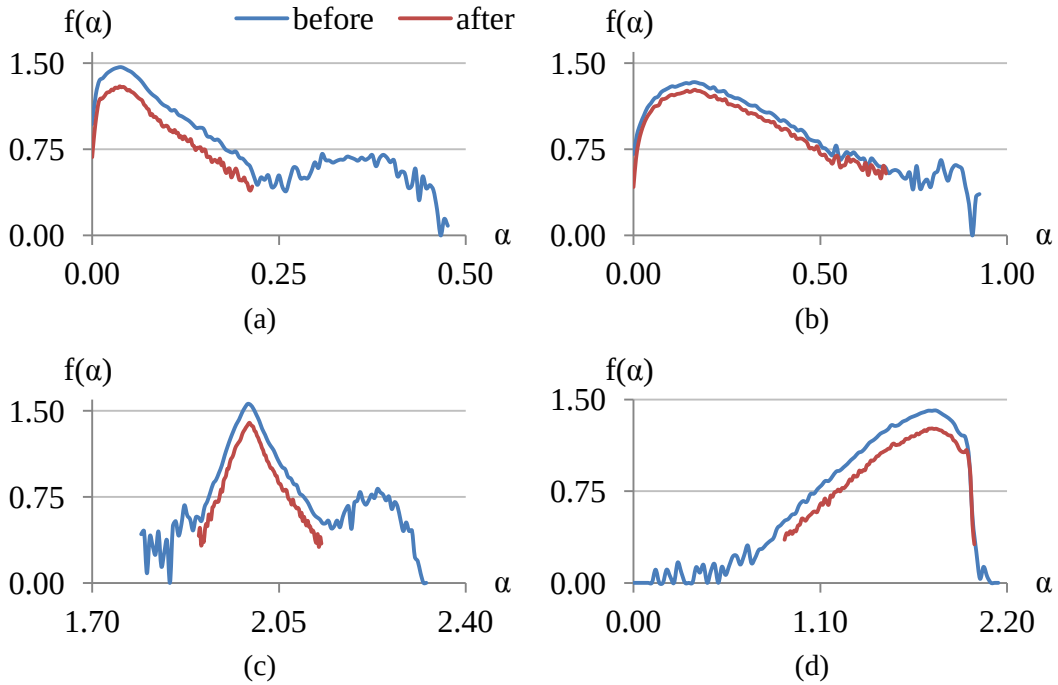

Figure 3-10 The effect of adjusting the α-range of the multifractal spectrum for Figure 3-3 which uses the (a) max measure (b) inv-min measure (c) sum measure (d) Iso measure

3.5 Applications in Medical Image Processing

Song et al. related electroencephalogram (EEG) signals with multifractal theory. They compared EEG signals with rapid eye movement (REM) sleep and four different sleep stages: awake, Stage 1, Stage 2, and slow wave sleep (SWS). The fluctuation in signals could have correlated, uncorrelated, and anti-correlated behaviours. Song et al. showed that EEG signals during different sleep stages could be differentiated with multifractal measures. Human sleep EEG signals during awaken stage, Stage 1, and REM sleep had shown anti-correlated behaviours, while Stage 2 sleep had uncorrelated behaviour, and SWS stage had correlated behaviour. Different sleep stages were briefly classified, and a total error rate of 41.8% was found [52]. Therefore, Song et al. recommended that a set of scalars could better describe human sleep EEGs rather than a single dominant scale which were suggested in other researches.

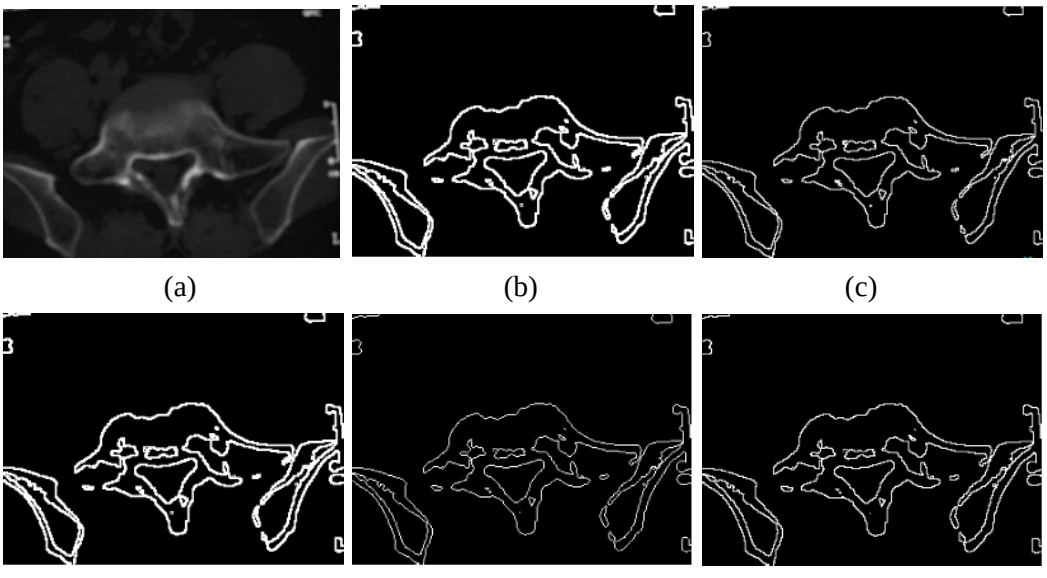

Figure 3-11 Example of an medical image (a) original; result after: (b) Sobel operator (c) Robbers operator (d) Prewitt operator (e) Log operator (f) Hölder exponent [53]

Qi and Yu applied multifractal spectrum as an edge detection tool for a medical computed tomography (CT) image. They compared the result with four different edge detection tools: Sobel operator, Robbers operator, Prewitt operator,

and Log operator. As shown in Figure 3-11, these operators could not precisely display the edge information. Intact edges could not be detected with Robert, Sobel, and Prewitt operators, while Log operator could not obtain continuous edges. However Hölder exponent could detect exact edges with a proper selection of multifractal spectrum threshold. Therefore, multifractal theory was concluded to be a relatively effective method for edge detection [53].

The structure of the human retinal vessels had been proven to have geometrical fractal properties by many literatures. Applying the fractal concepts, Family et al. presented the first quantitative analysis on the geometry of blood vessels in normal human retina in 1989 [54]. A year later, Mainster concluded that fractal geometry offered a more accurate description of ocular anatomy as fractal dimension could characterise a complete vascular patterns span over the retina [55]. Landini et al. (1995) [56] and Avakian et al. (2002) [57] pointed that the previous work only focused on a single fractal analysis: retinal vessels might have different properties in different regions. In 2006, T. Stosic and B. Stosic showed that human retinal vessels have geometrical multifractal properties. Examples of retinal vessel are illustrated in Figure 3-12. T. Stosic and B. Stosic also found that by comparing the normal cases with pathological cases, images with pathological cases tended to have lower generalized dimensions and have a shifted spectrum range. However, they suggested more detailed studies were needed to explore the statistical significance between normal and pathological cases [58].

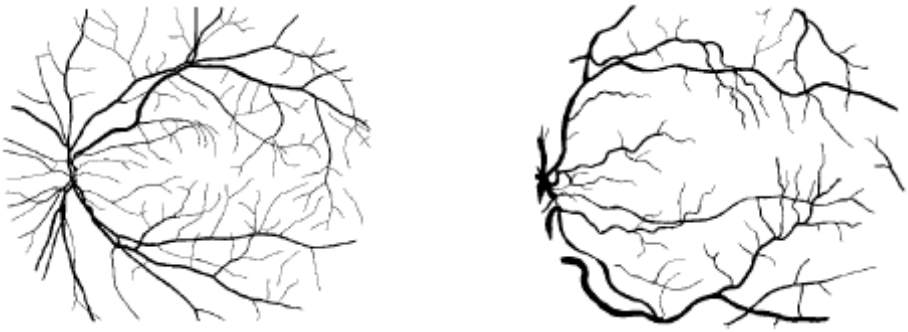

(a) (b)

Figure 3-12 Image of a retinal vessel structure: (a) normal (b) pathological state [58]

The time series of human brain activity could be extracted from arterial spin labelling (ASL) Functional Magnetic Resonance Imaging (FMRI). Some researchers focused on multifractal formalism when analysing these human brain function. Multifractal formalism for FMRI analysis were based on two methods: Wavelet Modulus Maxima Method (WTMM) [59] and Multifractal Detruded Fluctuation Analysis (MF-DFA) method [60]. Shimuze et al. proposed a multifractal FMRI analysis based on WTMM, which had high accuracy in the scaling analysis and did not require a prior knowledge of the paradigm. However, the extension of application on ASL function time series was limited by the complexity of this method [61, 62]. On the other hand, Kantelhardt et al. studied multifractal analysis which is based on MF-DFA. Although both WTMM and MF-DFA provided similar results, Kantelhardt et al. showed that MF-DFA was more reliable than WTMM [60]. Soares et al. used MF-DFA method and demonstrated that the voxels from activated and non-activated brain regions showed clear differences in the multifractal spectra [63]. The time series of human brain activity exhibited self-similarity formalism and could be described with multifractal spectra.

3.6 Summary of Multifractal Method

Square window is used for calculating the local singularity coefficient of the image, and the result of the calculation is called the α-image. Four multifractal measures are applied; each measure has its unique characteristics. Multifractal spectrum is a function which describes the geometrical property of the α-image; it can be estimated via box counting method. A brief flow chart to describe the process of calculating the Hölder exponent and multifractal dimension is demonstrated in Figure 3-13.

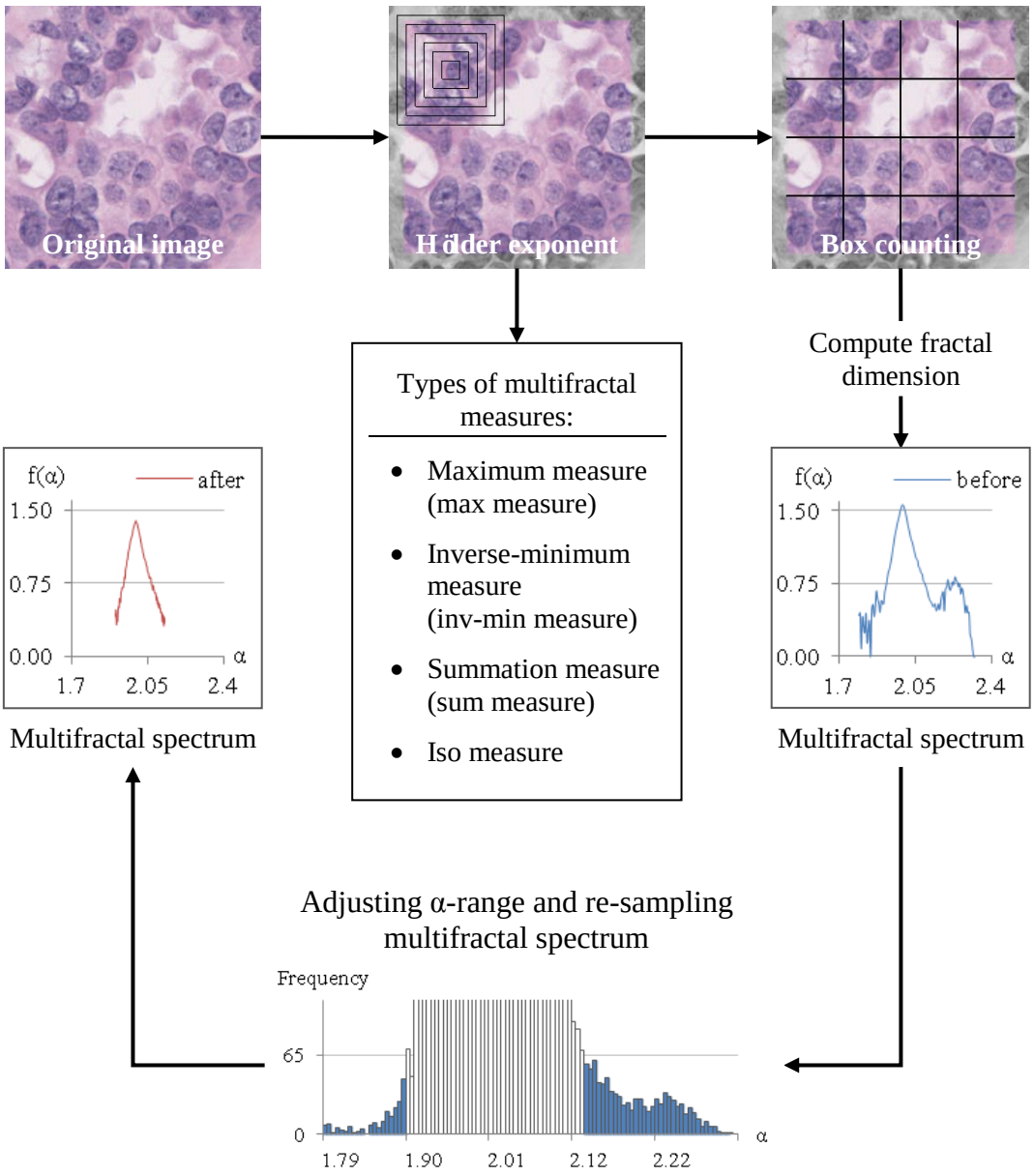

Figure 3-13 Summary of calculating the Hölder exponent and multifractal dimension

Multifractal formalism is an effective tool for biomedical image processing. Many researchers have proposed using this technique for different medical applications. The multifractal analysis designed for breast cancer grading is discussed in Chapter 4.

Chapter 4:

System Structure and Implementation

The criteria denoted for NGS (described in Chapter 2) and multifractal theory (defined in Chapter 3) are combined and demonstrated along with the description of the structure for the breast cancer analysis system in this chapter.

4.1 System Overview

The system overview for the multifractal analysis of breast cancer grading is indicated in Figure 4-1. First, the image frames are loaded to the system, and the calculation for Hölder exponent based on four multifractal measures is performed to generate the α-images. Then, the α-threshold comparison is applied to separate the sub-image frames of epithelial type tissues from those of non-epithelial type tissues. Once the epithelial sub-image frames are identified, the system detects the mitotic cells and computes the fractal spectra of the α-images. Finally, the information for NP and TF are analysed from the multifractal spectra.

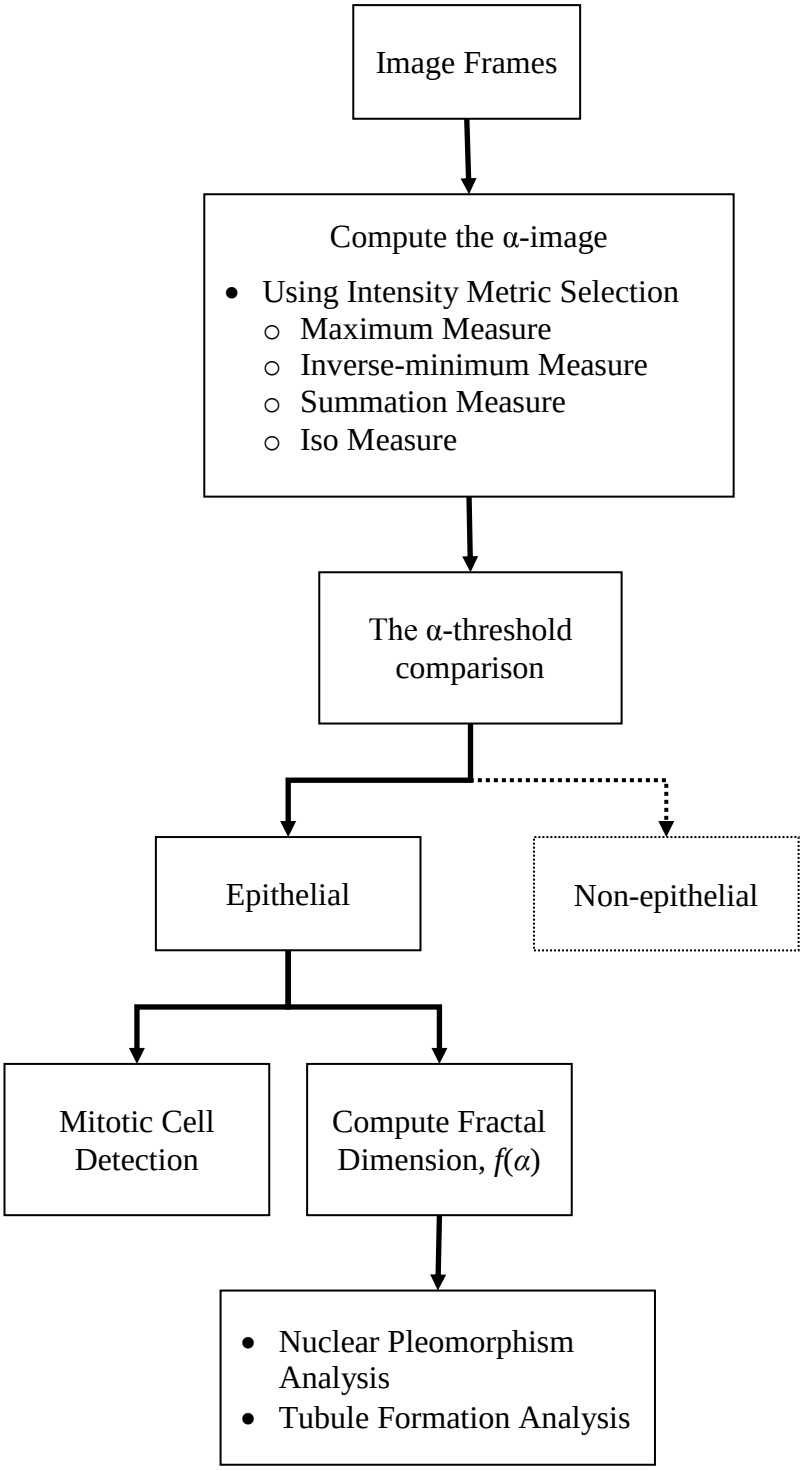

Figure 4-1 System overview of the multifractal analysis of the tissue images

4.1.1 Image data extraction

The high resolution, high magnification histopathological images and data used in this research were provided by IPAL, where 17 histopathological images were identified and graded by pathologists. These images can be viewed with the FrameWork Viewer, a software workstation for laboratories imaging. As shown in Figure 4-2, pathologists can label the invasive regions, identify the mitotic cell, and grade the invasive areas with NP and TF scores based on NGS.

Figure 4-3 shows some of the image samples, with the size of 1,024 × 1,024 pixels each, that had NP and TF scores pre-assigned by pathologists. Tissue substances of similar types occupy a relatively small area of a section image. Hence the identified ROIs need to be cropped into smaller sub-images. Figure 4-4 is an example of the developed graphical user interface (GUI) program that collects the sub-images. The GUI program was built under the OpenGL framework; more developed visualising programs can be found in Section 4.5. The sub-images are randomly sub-divided into smaller image frames with the size of 288 × 288 pixels each, from the labelled invasive region of the histopathological image. Each image frame contains a border of 16 pixels wide, which is the window size for measuring local singularity coefficient. The sizes of the final α-images are 256 × 256 pixels each.

Each of the 17 histopathological images contributed 150 to 250 sub-image frames. 850 sub-image frames were non-epithelial type. 3,270 sub-image frames were epithelial types and had NP score pre-labelled by pathologists; only 600 sub-image frames had TF score pre-labelled. The number of image frames analysed in this research is summarised in Table 4-1.

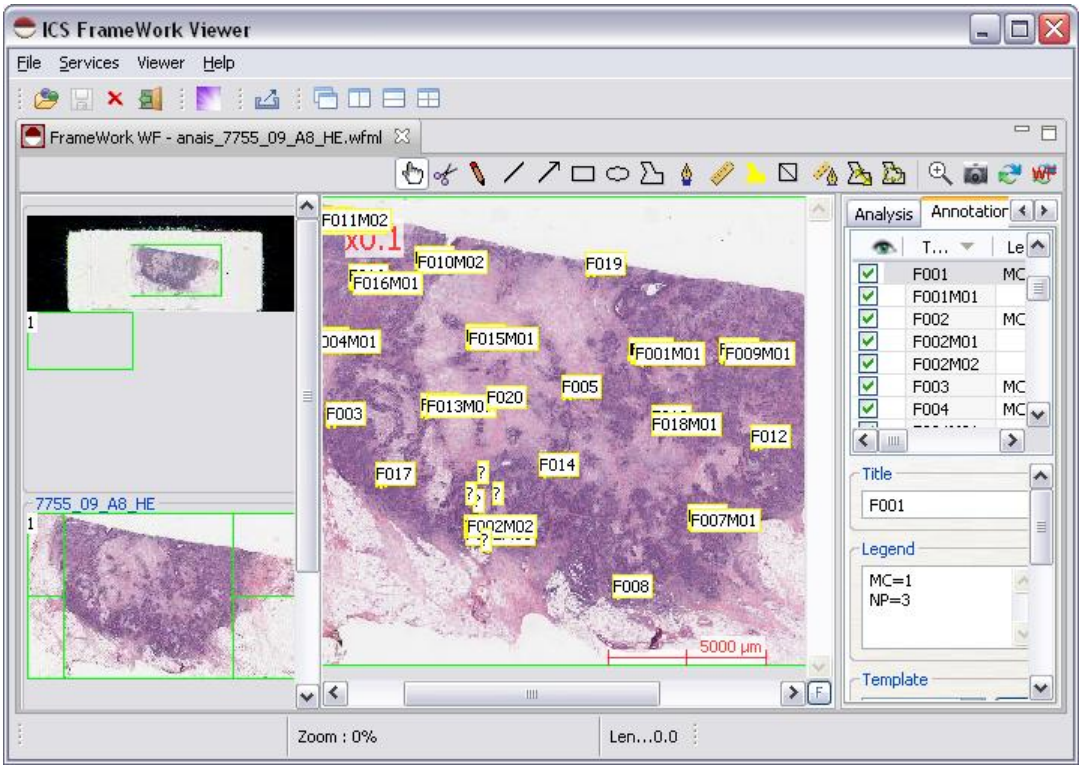

(a) A view of a full slide biopsy sample

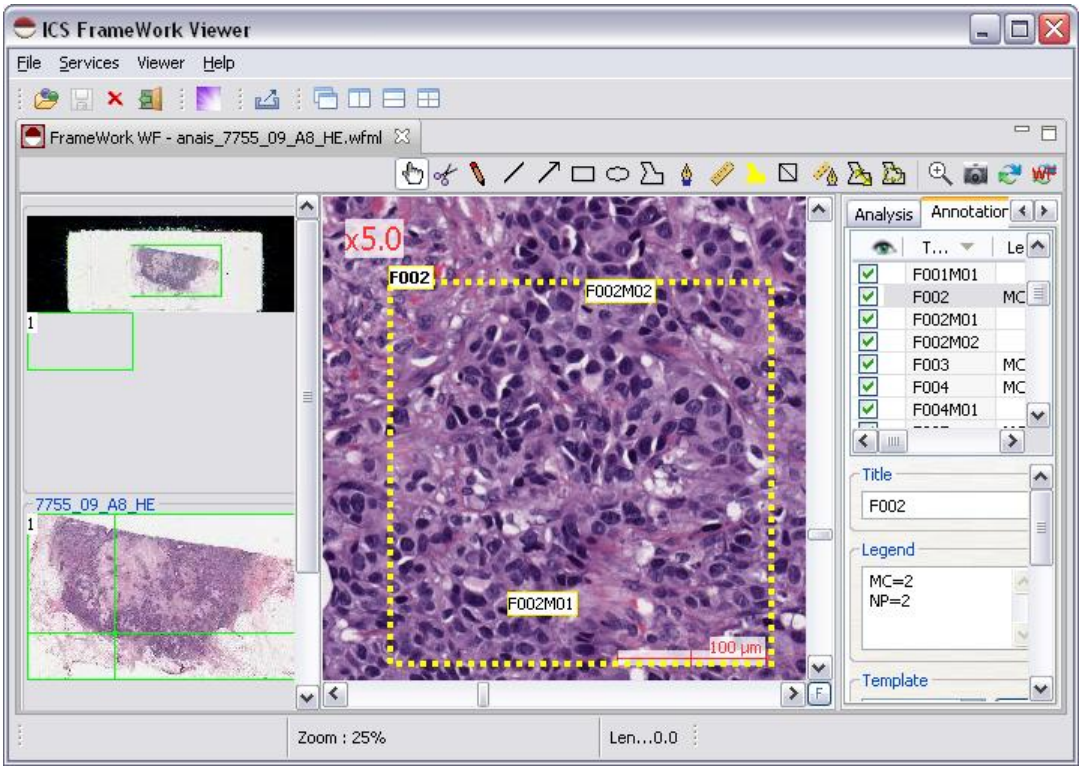

(b) A section view of ×5.0 zoom in

Figure 4-2 Screenshots of the FrameWork Viewer

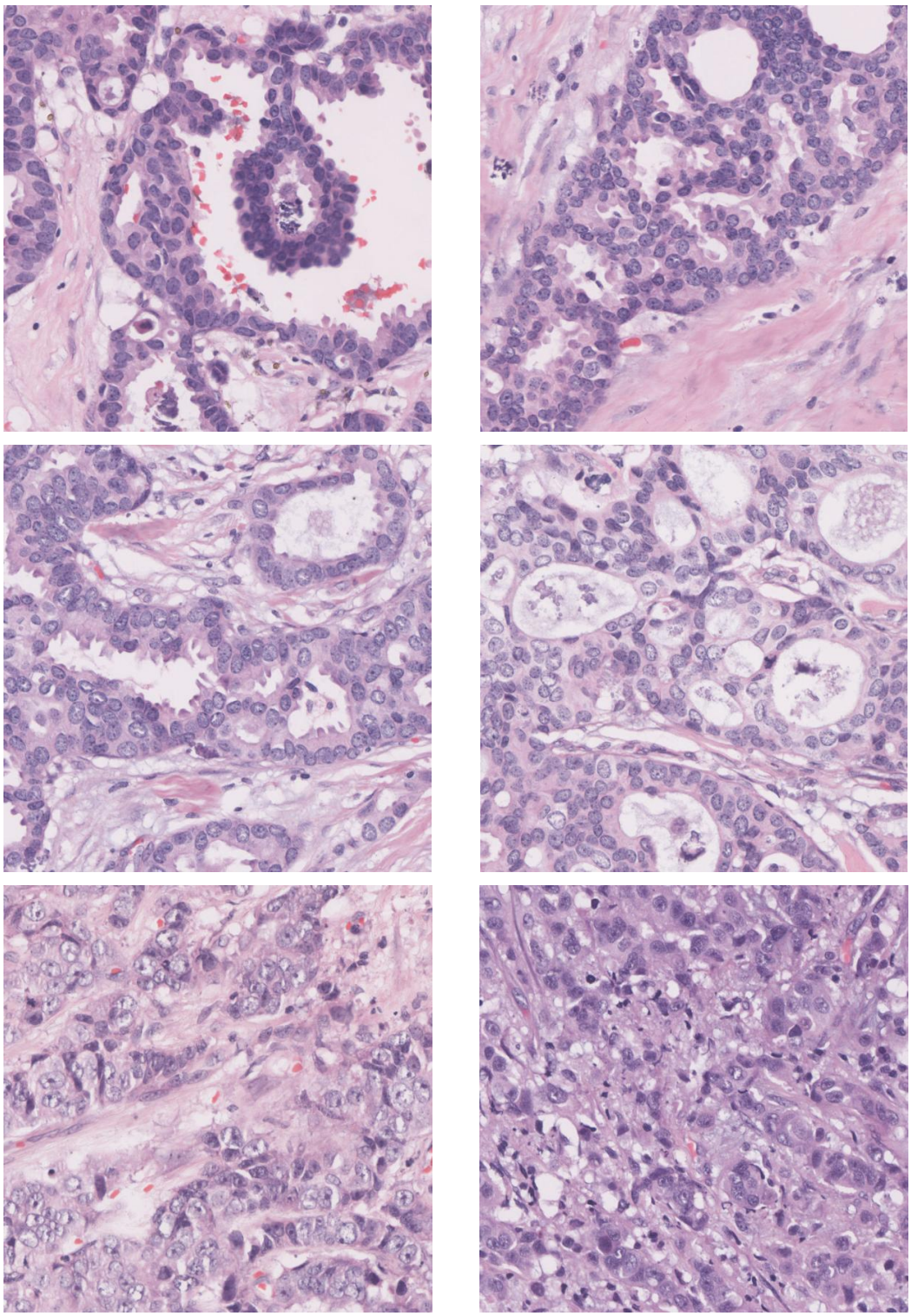

(a) (b)

Figure 4-3 Sample images of pre-labelled: (a) NP (b) TF scores,

(from top to bottom) Score 1, Score 2, and Score 3

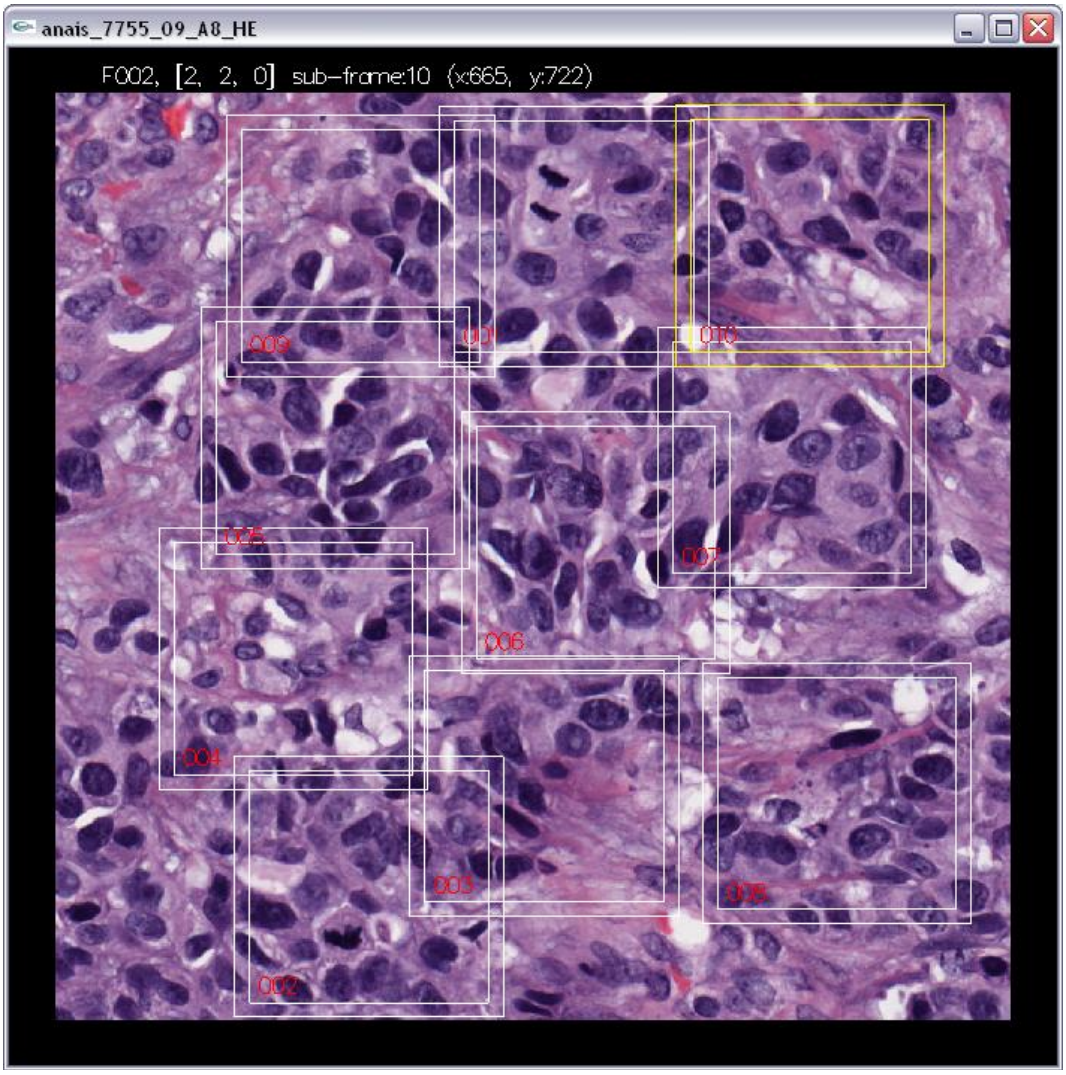

Figure 4-4 The developed GUI for cropping 10 sub-image frames from a NP/TF-labelled region

Table 4-1The number of image frames used for data analysis

	Score			
Criterion	1	2	3	Total
NP	350	970	1,950	3,270
TF	160	60	380	600

4.2 First Stage Classification

Petushi et al. classified the tissue micro-textures into five categories: nuclear morphology 1 (NM1), nuclear morphology 2 (NM2), nuclear morphology 3 (NM3), extra cellular matrix (ECM), and adipose tissue (AT). They defined NM1 to be the nuclei of inflammatory cells, NM2 to be the nuclei of cells of epithelial origin, NM3 to be the nuclei of cancer cells, ECM to be a collagen-based matrix, and AT to be the area that represents water, carbohydrate, lipid or gas [36, 37].

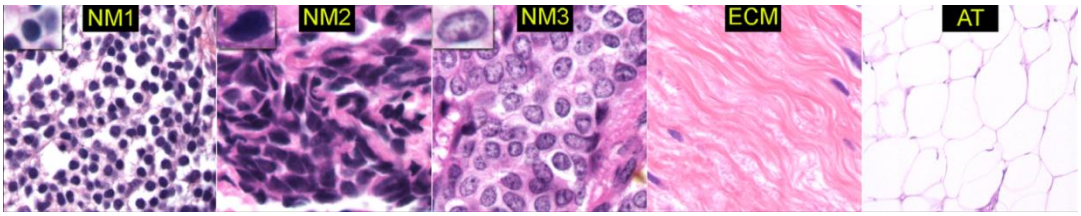

Figure 4-5 Tissue micro-textures identified using image processing [36]

This research classifies the image frames into two tissue structure categories: epithelial type and non-epithelial type. Examples of these image frames are given in Figure 4-6. Stroma and fat-like tissues (ECM and AT) are categorised as non-epithelial tissue because they have a plain tissue substance and are irrelevant to breast cancer grading. Furthermore, differentiating the epithelial tissue from stroma and connective tissue is a common practice for most cancer tissue types [17]. Huang et al. used epithelial tissue images to extract information for Nottingham parameters [20, 64]. Hence, only the image frames which have epithelial tissue are carried for further analysis.

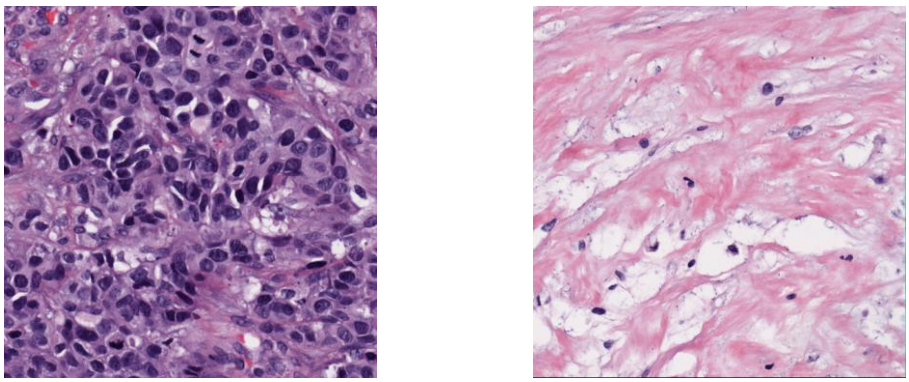

(a) (b)

Figure 4-6 The tissue image example of (a) epithelial type (b) non-epithelial type

Based on the multifractal properties of sub-image frames, the characteristic of epithelial tissue can be identified from the α-range of the max and sum measures. The minimum α-value in the Iso measure is the key feature for separating the epithelial and non-epithelial tissues.

Table 4-2 and Figure 4-7 show the α-ranges of sub-image frames generated from a histopathological image. As indicated in Figure 4-7 (a) and Figure 4-7 (b), epithelial tissues have greater α-ranges of the α-image compared to non-epithelial tissues in both max and sum measures. An epithelial tissue contains cell nuclei along with other tissue substances; therefore, its intensity distribution is richer than the images of stroma and fat-like tissue.

The image of non-epithelial tissue has a nearly uniform intensity distribution and yields higher α-values for Iso measure. As mentioned in Section 3.2.4, the Iso measure counts the number of pixels that have similar intensity values as the centred pixel. The α-value of a pixel based on Iso measure is small if the intensity values of the nearby pixels have great difference. Conversely, non-epithelial tissue has larger α_{min} value. Note that these α-ranges are post-adjusted for noise removal.

Table 4-2Examples of α-range from a histopathological example

Type of multifractal	Epithelial		Non-epithelial	
	α_{min}	α_{max}	α_{min}	α_{max}
Max measure	[*0.00, 0.00*]	[*0.29, 0.51*]	[*0.00, 0.00*]	[*0.02,0.19*]
Sum measure	[*1.*80, *1.89*]	[*2.20, 2.38*]	[*1.89, 1.99*]	[*2.01, 2.15*]
Iso measure	[*0.*56, *0.84*]	[*1.94, 2.04*]	[*0.89, 1.86*]	[*2.01, 2.08*]

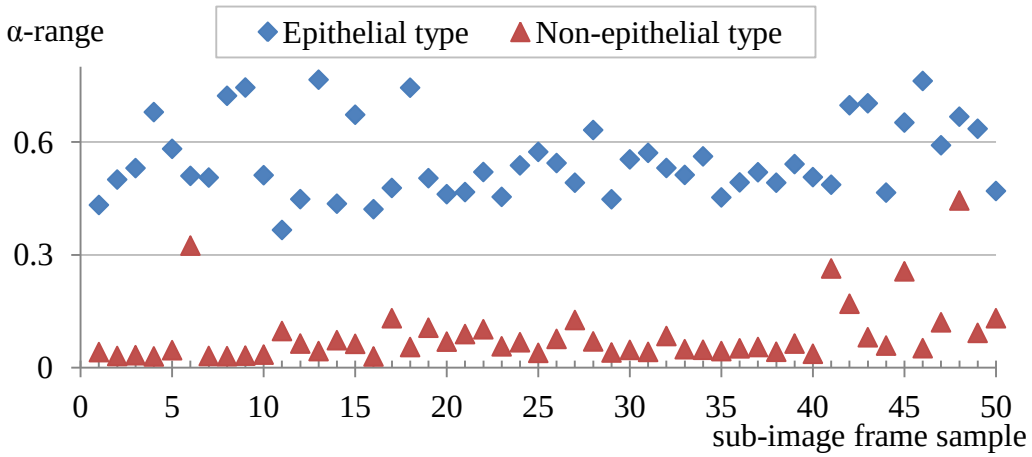

(a) Max measure

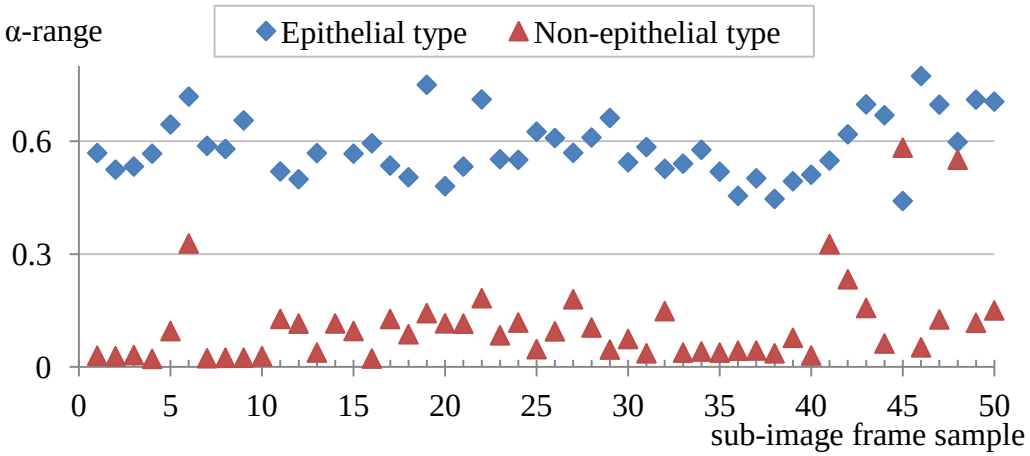

(b) Sum measure

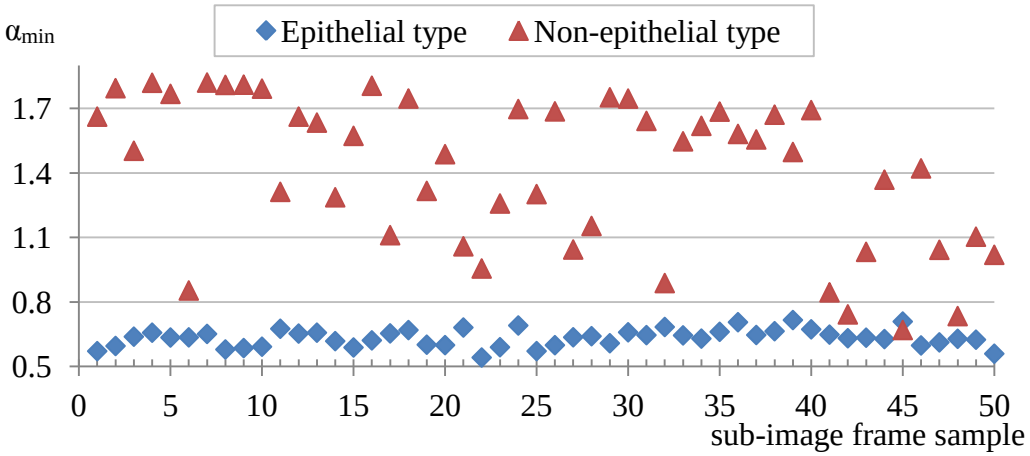

(c) Iso measure

Figure 4-7 The α-range of sub-image frames from a histopathological sample

4.3 Mitotic Cell Detection

As mentioned in Section 2.2, mitotic cells are darker and have irregular shapes. These properties enable the detection of mitotic cells from computed α-values within the cell region. Figure 4-8 illustrates the detection of a mitotic cell, which was pre-detected by pathologists, as labelled "M1" in Figure 4-8 (a).

From Figure 3-5(a) and Figure 3-5 (c), it is clear that the mitotic cell has higher α-values in both max measure and sum measure than other tissue substances. The α-threshold based on sum measure is used for detecting mitotic cells in this study. As shown in Figure 4-8 (b), the pixels with α-values above 55% of the α-range remain visible in the binary image.

All connected components are marked based on the threshold binary α-image. A connected component is considered as noise if its area is smaller than the predefined threshold of 100 pixels. The largest remaining component after removal of noise usually indicates a mitotic cell. The resulting mitotic cell detected, C1, is shown in Figure 4-8(c).

However, the selection of α-threshold and noise threshold can affect the result. The evaluation is discussed in Section 5.3.

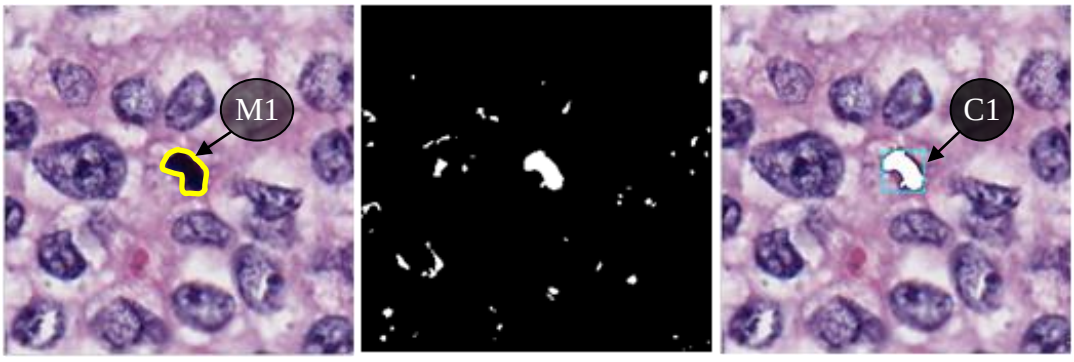

(a) (b) (c)

Figure 4-8 The process of detecting a mitotic cell: (a) original image with a manually detected mitotic cell (b) the binary threshold image (c) the computationally detected mitotic cell

4.4 Nuclear Pleomorphism and Tubule Formation Analysis

The information of NP and TF scores can be extracted from the multifractal spectra. NP is a measurement for the deviation of cellular structures such as the sizes and shapes of cell nuclei. A cell nucleus is darker in colour, and hence its pixels' intensity values are smaller than other tissue substances. Based on this feature, the pixels of cell nuclei have a unique multifractal feature. The binary α-images of cell nuclei located within the specific α-sub-ranges are shown in Figure 4-9.

The criterion TF is an estimation of the percentage of biopsy sample made up of tubules. In this research, the TF criterion was analysed in high resolution image frames, where most researchers analysed the TF scoring under low resolution global images [27, 35-37]. The advantage of taking this approach is that both NP and TF scores can be analysed together. The binary α-images where tubules are present within the unique α-sub-ranges are shown in Figure 4-10.

All four types of multifractal spectra contain the information of NP and TF, as summarised in Figure 4-11 and Table 4-3. As mentioned in Section 3.3, every image frame has its unique α-range, so the α-sub-range of interest varies between each image frames.

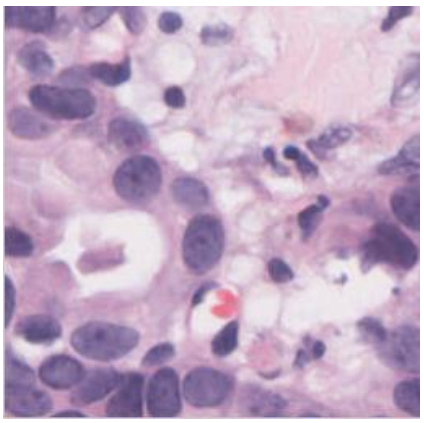

(a)

(b)

(c)

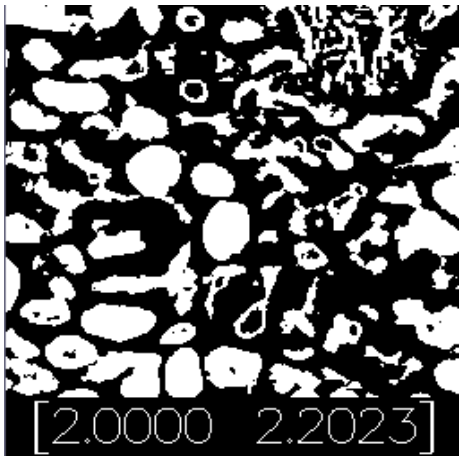

(d)

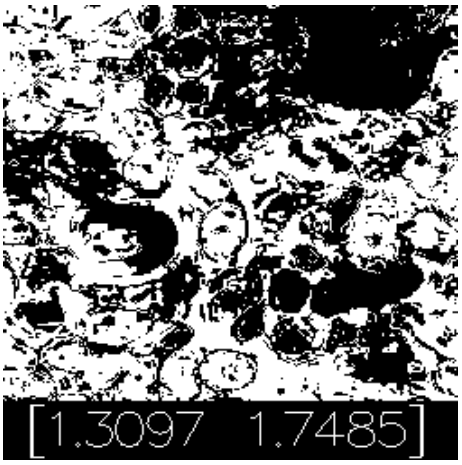

(e)

Figure 4-9 (a) The original sub-image frame, and the binary α-image of the specific α-sub-range for NP analysis: (b) max measure (c) inv-min measure (d) sum measure (e) Iso measure

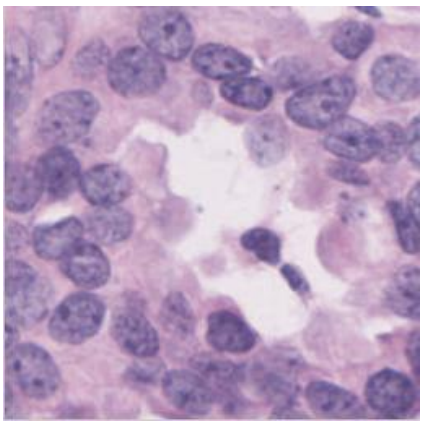

(a)

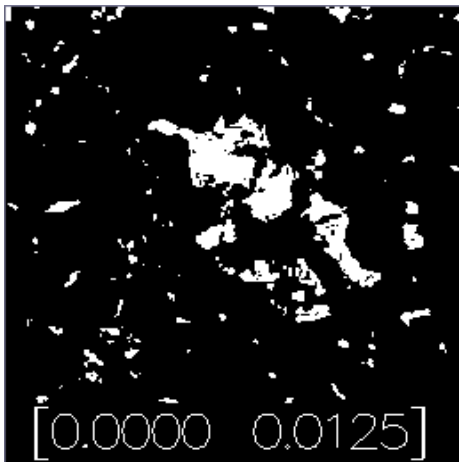

(b)

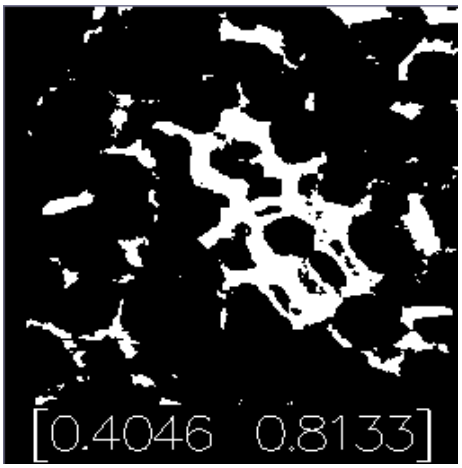

(c)

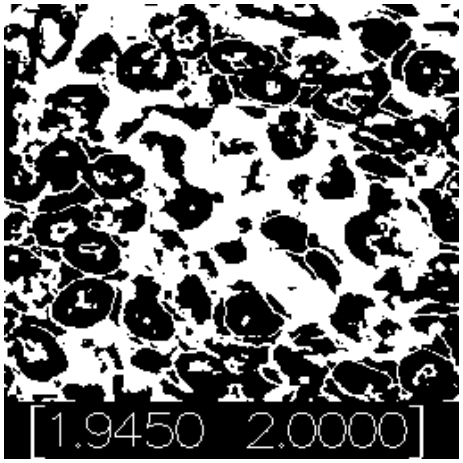

(d)

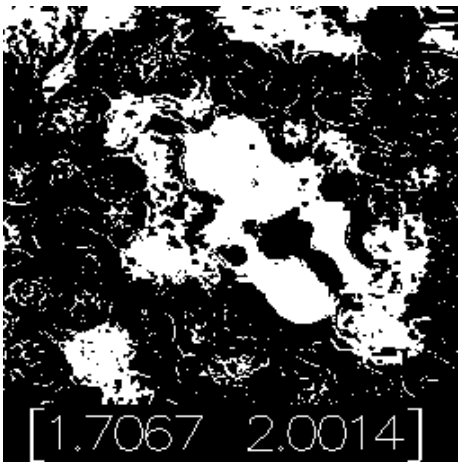

(e)

Figure 4-10 (a) The original sub-image frame, and the binary α-image of the specific α-sub-range for TF analysis: (b) max measure (c) inv-min measure (d) sum measure (e) Iso measure

Table 4-3Properties of the multifractal spectrum for NP and TF analysis

Type of multifractal measures	α-sub-range of interest			
	Nuclear Pleomorphism (NP)		Tubule Formation (TF)	
	from, α_0	to, α_1	from, α_2	to, α_3
Max	α_0, $f(\alpha_0) = 1$	α_{max}	α_{min}	α_3, $f(\alpha_3)$ at peak
Inv-min	α_0, $f(\alpha_0)$ at peak	α_1, $f(\alpha_1) = 1$	α_2, $f(\alpha_2) = 1$	α_{max}
Sum	$\alpha = 2$	α_{max}	α_2, $f(\alpha_2) = 1$	$\alpha = 2$
Iso	α_0, $f(\alpha_0) = 1$	α_1, $f(\alpha_1)$ at peak $1.4 < \alpha_1 < 1.9$	α_2 $\alpha_2 = 0.75 \times$ α-range	α_{max}

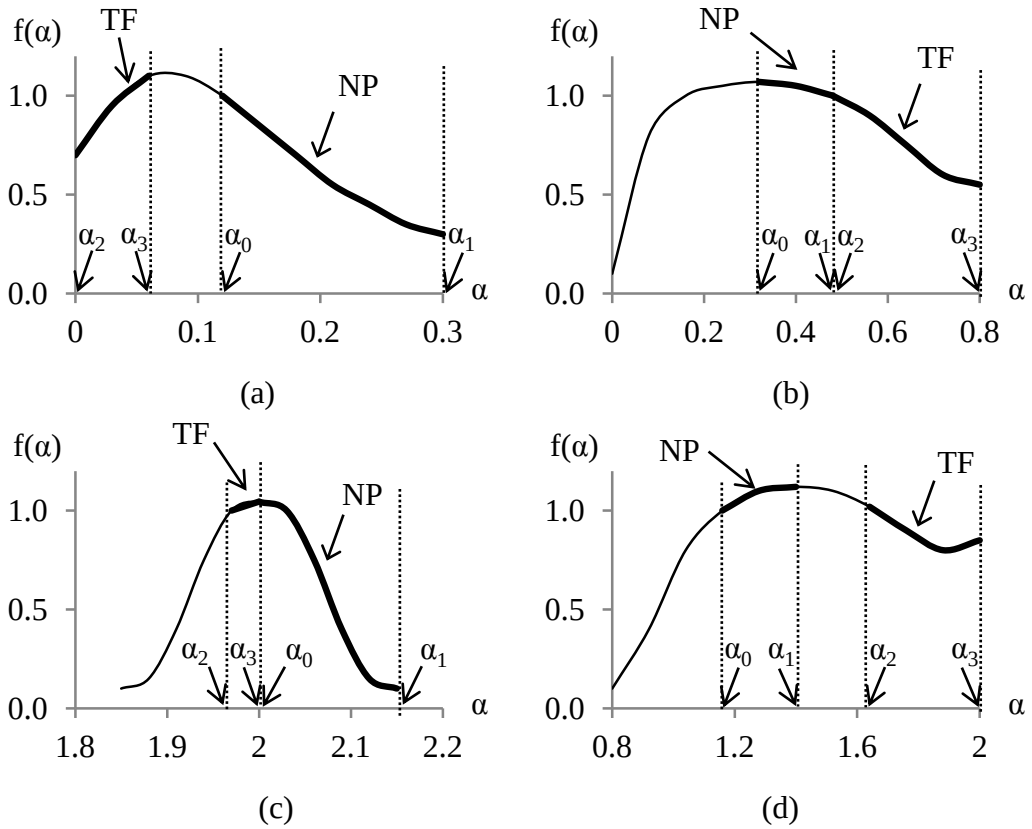

Figure 4-11 Multifractal spectrum for NP and TF analysis: (a) max measure (b) inv-min measure (c) sum measure (d) Iso measure

4.4.1 The development of the analysis

The features of NP and TF scores can be extracted from the multifractal spectra which have been discussed earlier. Every pixel in the sub-image carries four unique α-values calculated via four multifractal measures. If the α-value of a pixel is present in the α-sub-range of interest, the system would determine whether it is relevant for NP or TF analysis. However, the binary α-images based on the inv-min and sum measures contained background pixels that were irrelevant to the analysis.

Combining the unique features of Iso measure with α-images based on other multifractal measures can identify some of the background pixels. Iso measure describes the intensity similarity of the centred pixel and its surrounding pixels. Therefore, the α-value of the pixel given by Iso measure is small when its intensity value differs significantly from its neighbours, and vice versa. This property can be applied to improve the quality of NP and TF analysis.

As discussed above, the enhancement of NP analysis is to combine the α-images with the properties of Iso measure. For example, the α-value of a pixel based on sum measure is relevant to NP analysis if its α-value based on Iso measure is also relevant to NP analysis. For NP analysis, the inv-min measure should include the pixels that have α-values below 75% of the α-range of Iso measure. Similarly, when sum measure is applied, the system should take into account the pixels with α-values below 65% of the α-range of Iso measure.

This concept can also apply to TF analysis. TF analysis focuses on the distribution of tubules in a region. Tubules have constant intensity values; hence, the α-values based on Iso measure should be high. Therefore, the analysis using inv-min and sum measures should consider pixels with α-value above 75% of the α-range of Iso measure.

For NP analysis, the background pixels present in the binary α-image, as shown in Figure 4-12 (b) and Figure 4-12 (d), can be removed. The results are shown in Figure 4-12 (c) and Figure 4-12 (e) respectively. Likewise, as shown in Figure 4-13, after the enhancement, the background pixels for TF analysis have

significantly reduced. Although some of the background pixels remained after the enhancement, the estimations for NP and TF analysis have slightly improved and the results are still acceptable.

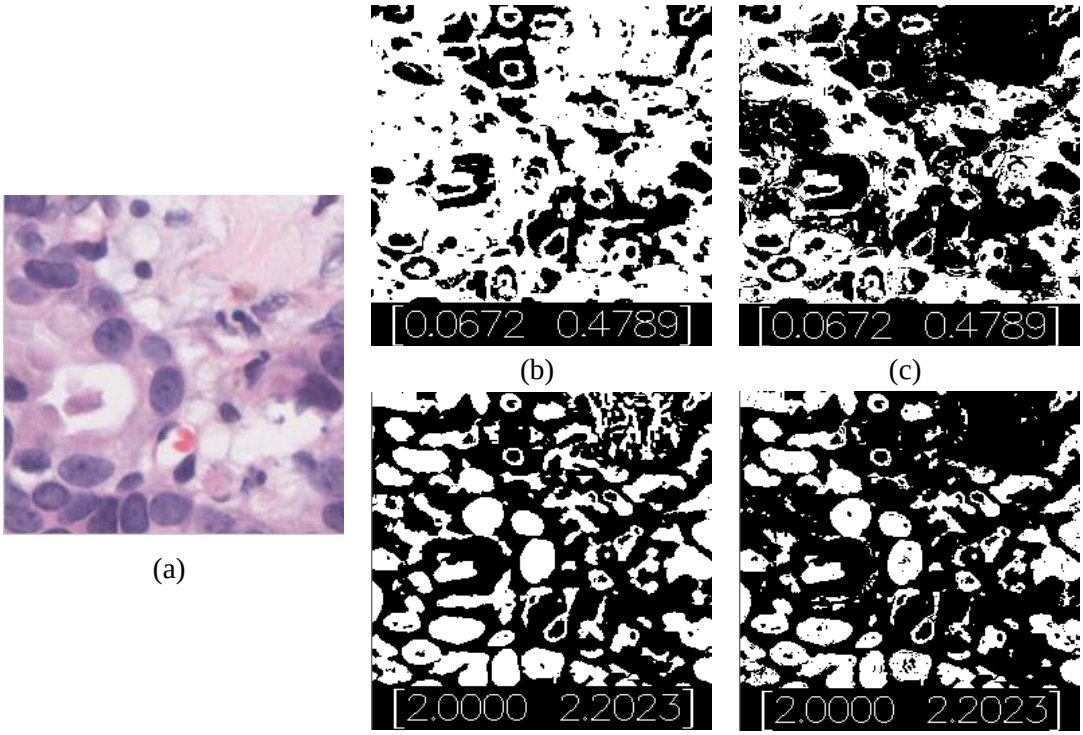

(a) (b) (c) (d) (e)

Figure 4-12Improvement of NP analysis: (a) the original image (b) before enhancement (c) after enhancement of inv-min measure (d) before enhancement (e) after enhancement of sum measure

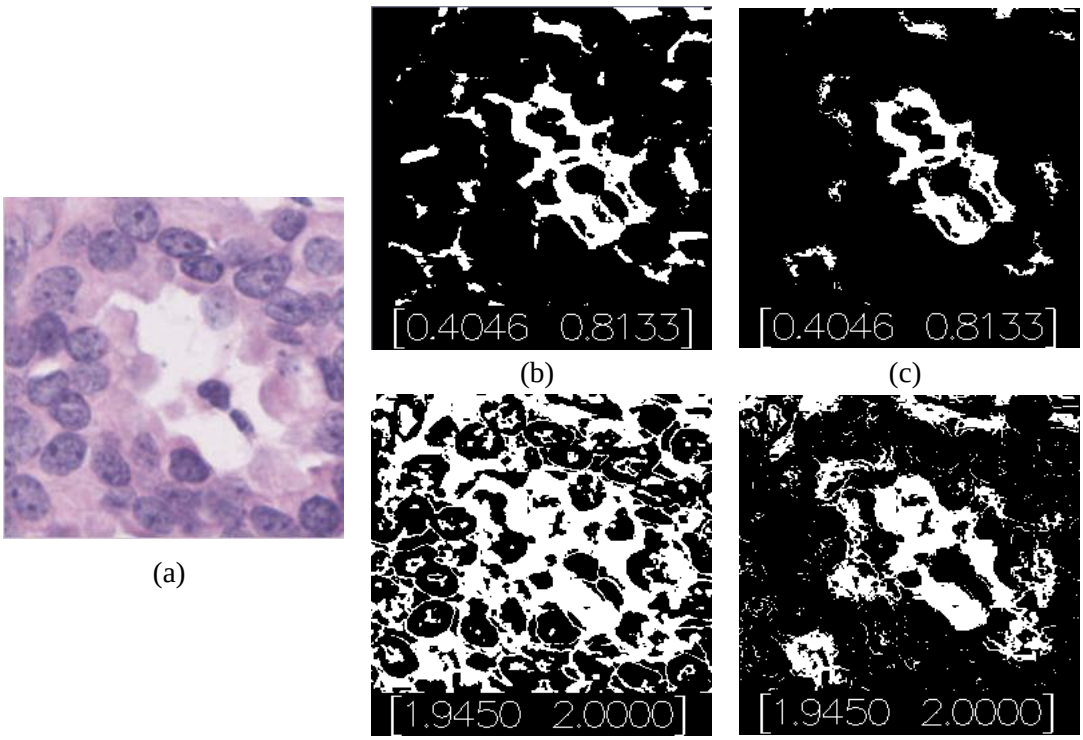

(a) (b) (c) (d) (e)

Figure 4-13 Improvement of TF analysis: (a) the original image (b) before enhancement (c) after enhancement of inv-min measure (d) before enhancement (e) after enhancement of sum measure

Besides, the enhancement of NP and TF analysis also requires the system to recalculate the fractal dimension of the image. The multifractal spectrum in Equation 3.9 is modified into:

$$f(\alpha)_{\gamma,\delta} = \frac{\log(n(\varepsilon)_{\gamma,\delta})}{\log(\varepsilon)} \tag{4.1}$$

$$n(\varepsilon)_{\gamma,\delta} = \#\left\{\Omega \;\middle|\; \begin{array}{c} \alpha_{\gamma,i} \le \alpha_{\gamma}(k,l) < \alpha_{\gamma,i+1} \\ \wedge \\ \alpha_{\delta,i} \le \alpha_{\delta}(k,l) < \alpha_{\delta,i+1} \end{array}, (k,l) \in \Omega\right\} \tag{4.2}$$

where # is the number of pixels

where γ is the fractal spectrum for the particular multifractal measure (inv-min measure or sum measure) and δ is the fractal spectrum of Iso measure. This modification has affected the fractal spectrum, and the effect on the summation measure is demonstrated in Figure 4-14.

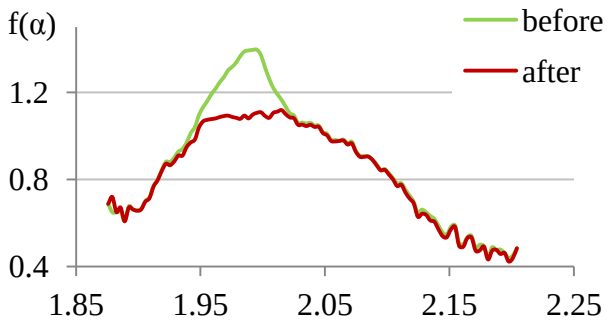

Figure 4-14 The effect of sum measure on the multifractal spectrum after applying the enhancement

After the enhancement of NP and TF analysis (as labelled in the boxes in Figure 4-15 and Figure 4-16 respectively), there is a clear difference between the spectra for NP and TF scores. Each score has unique features in the multifractal spectra. The key feature of analysing NP and TF scoring is to evaluate the slope of multifractal spectrum of the particular α-sub-range.

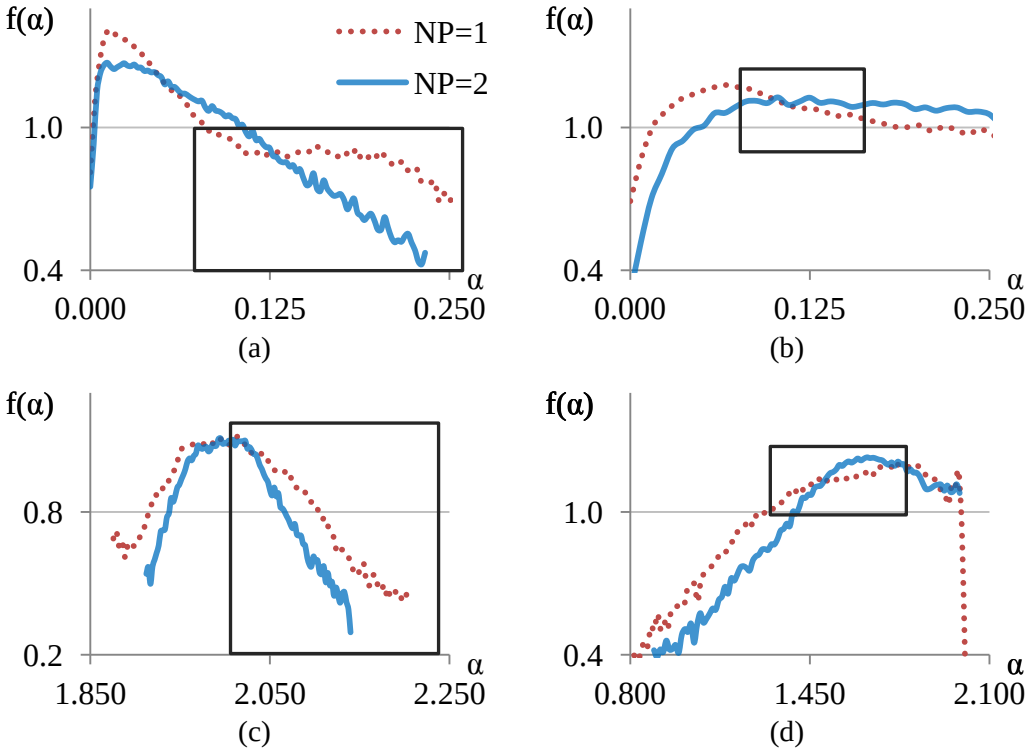

Figure 4-15 The features of multifractal spectrum for NP analysis: (a) max measure (b) inv-min measure (c) sum measure (d) Iso measure

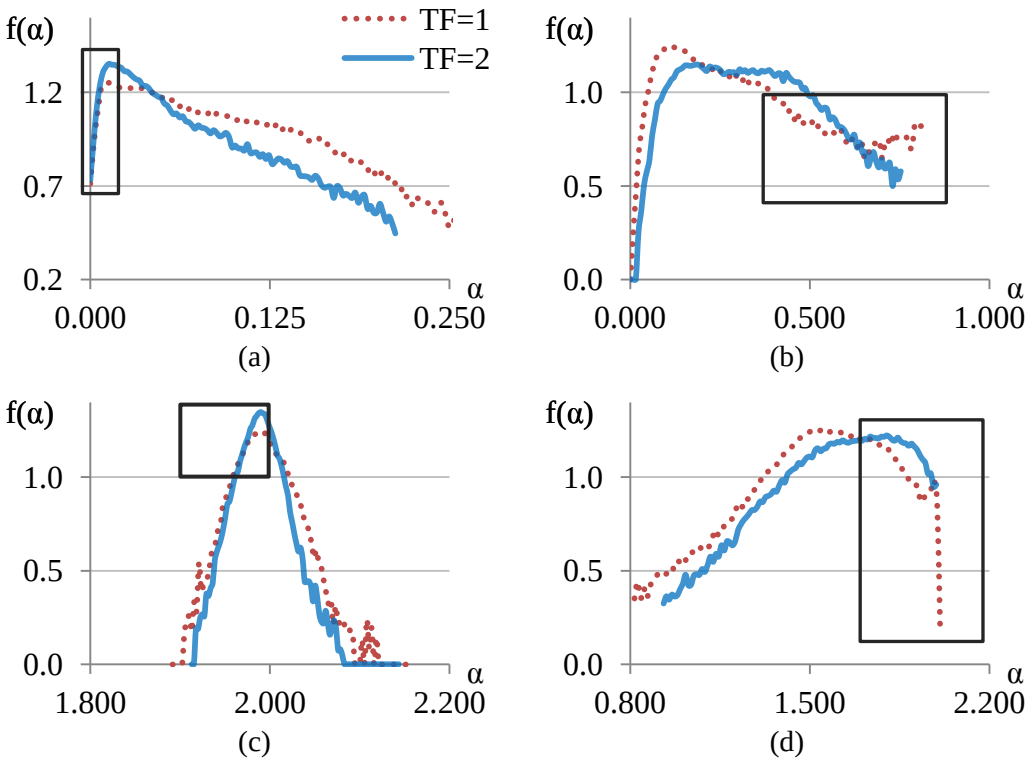

Figure 4-16 The features of multifractal spectrum for TF analysis: (a) max measure (b) inv-min measure (c) sum measure (d) Iso measure

4.4.2 Increasing the number of α-intervals

Fractal dimension is an estimation of a geometric property, local singular coefficient, of an image. As mentioned in Section 3.4.2, the number of subintervals applied for calculating the multifractal spectrum is 100. Increasing the number of α-intervals in the relevant section of α-range can change the estimation of fractal dimension. In the example of Figure 4-15 (c), the multifractal spectrum is calculated using the α-range [*1.8757*, *2.2043*], but the α-sub-range of interest for NP analysis is [*2.0000*, *2.2043*]. By increasing the number of α-intervals at this α-sub-range, the resolution of the spectrum can be improved. Figure 4-17 shows the difference of using α-range and α-sub-range during the calculation of multifractal spectrum. The multifractal spectrum based on the α-sub-range of interest has shifted downward because the number of pixels which fall into the α-interval has decreased. This has the same effect as increasing the number of intervals in the histogram, which causes the sampling distribution to drop.

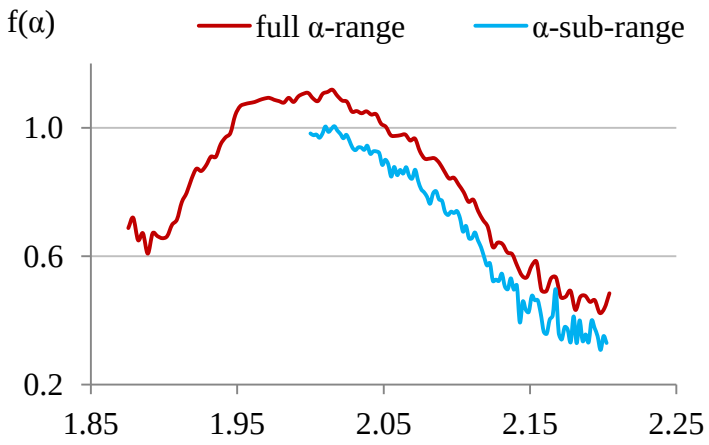

Figure 4-17 The multifractal spectrum that uses different α-range

4.4.3 Polynomial representation of the multifractal spectrum

The section of multifractal spectrum based on the α-sub-range of interest, which features with NP and TF scores, can be approximated by a cubic polynomial function $f_e(\alpha)$:

$$f_e(\alpha) = C_3\alpha^3 + C_2\alpha^2 + C_1\alpha + C_0 \tag{4.3}$$

where C_3, C_2, C_1, and C_0 are the arbitrary coefficients of the polynomial function. An example is shown in Figure 4-18.

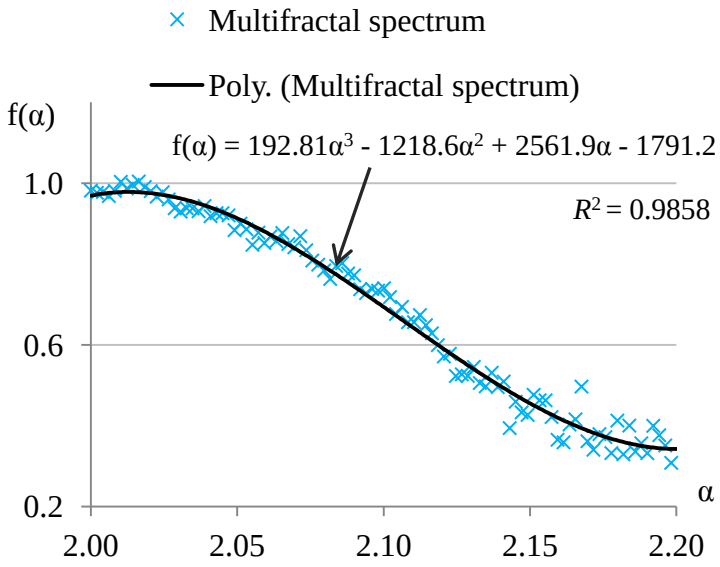

Figure 4-18 Multifractal spectrum of the original function and the cubic polynomial function

The polynomial representation is useful for transforming the multifractal spectrum which is a discrete function to a continuous third order polynomial equation. Since the α-sub-range of interest is small and the spectrum is unlikely to have more than two turning points, the third order polynomial equation is a sufficient approximation of the spectrum.

4.5 Graphical Interface Development for Analysis

During the development of this research, several GUI programs were developed to assist data analysis, these programs were written in C++ computer language under OpenGL framework. Although commercial products such as Microsoft Office and Matlab provide data analysis and visual functionalities, the developed GUIs were designed for specific task requirements in order to access the collected data with better control.

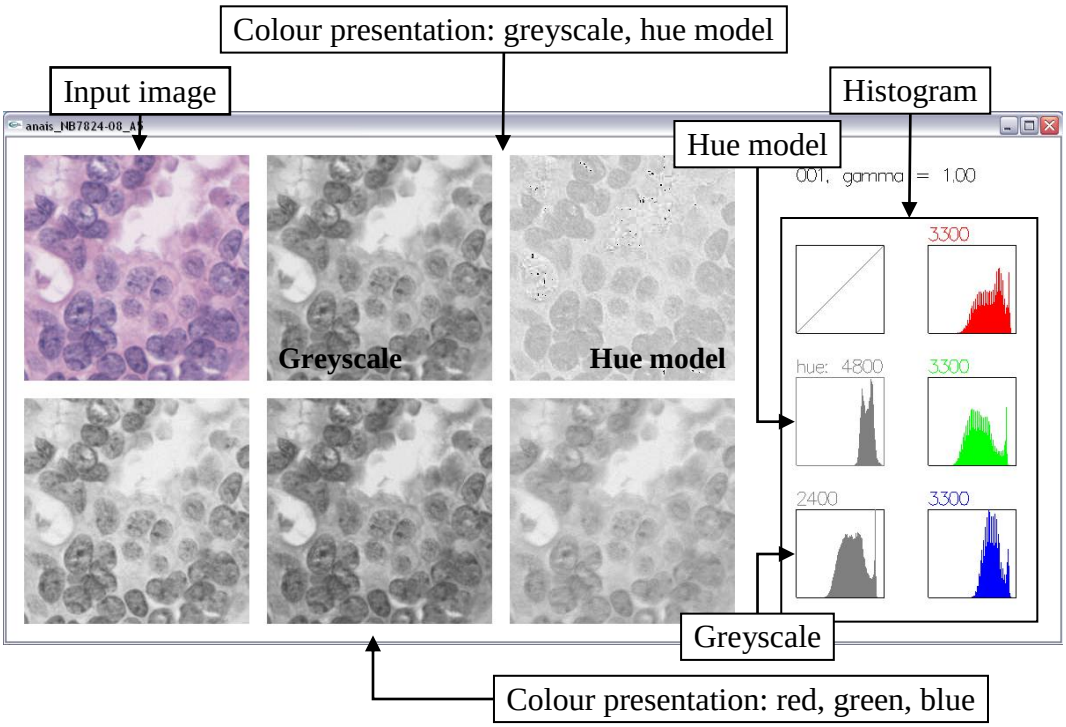

Figure 4-19 Displaying different colour models of an input image

GUI in Figure 4-19 was designed to demonstrate the colour presentation of an image under different colour models: greyscale, hue model, and red, green, blue

channels. Intensity histograms for each colour model are placed on the right hand side, which show the intensities distribution of colour values of the input image.

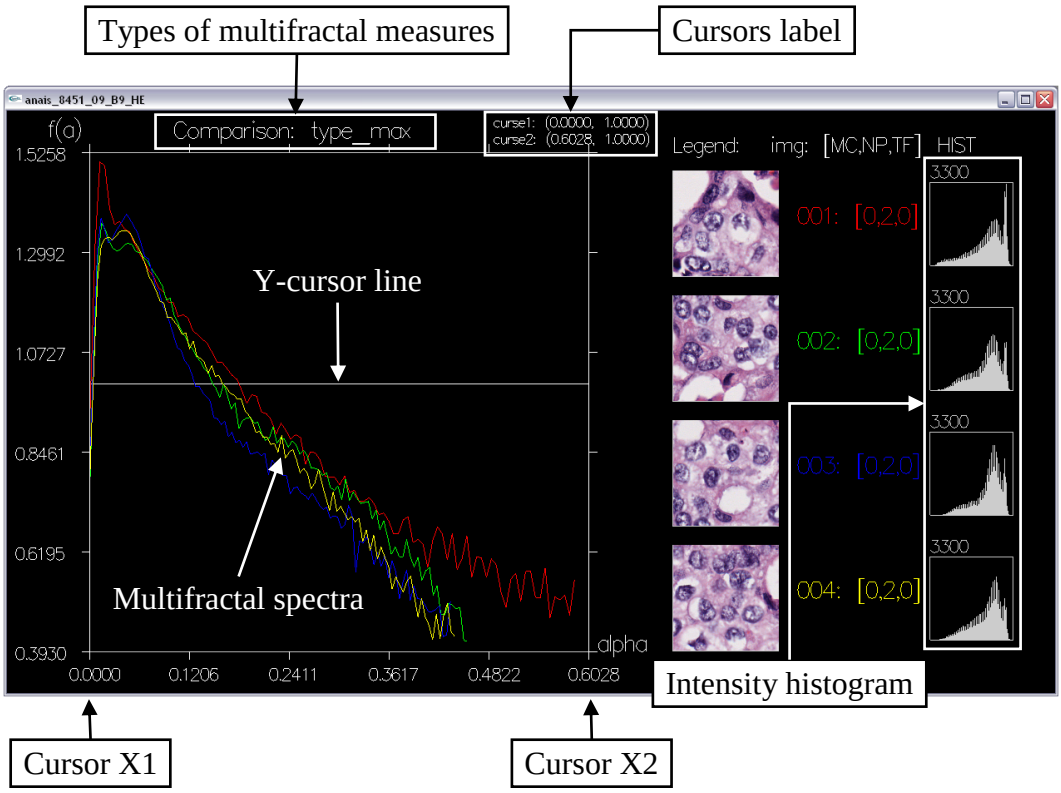

Figure 4-20 Displaying multifractal spectra of four sub-image frames

Meanwhile, GUI in Figure 4-20 was designed to display multifractal spectra based on different multifractal measures of the input images. The left panel shows multifractal spectra of four sub-image frames; users are allowed to switch between multifractal measures. In addition, there are two pairs of horizontal and vertical cursor lines, which display the values of Hölder exponent, α, and fractal dimension, $f(\alpha)$, on the spectrum. On the other hand, right panel displays the basic information of the input sub-image frames: thumbnail, MC, NP, and TF scores, and intensity histogram.

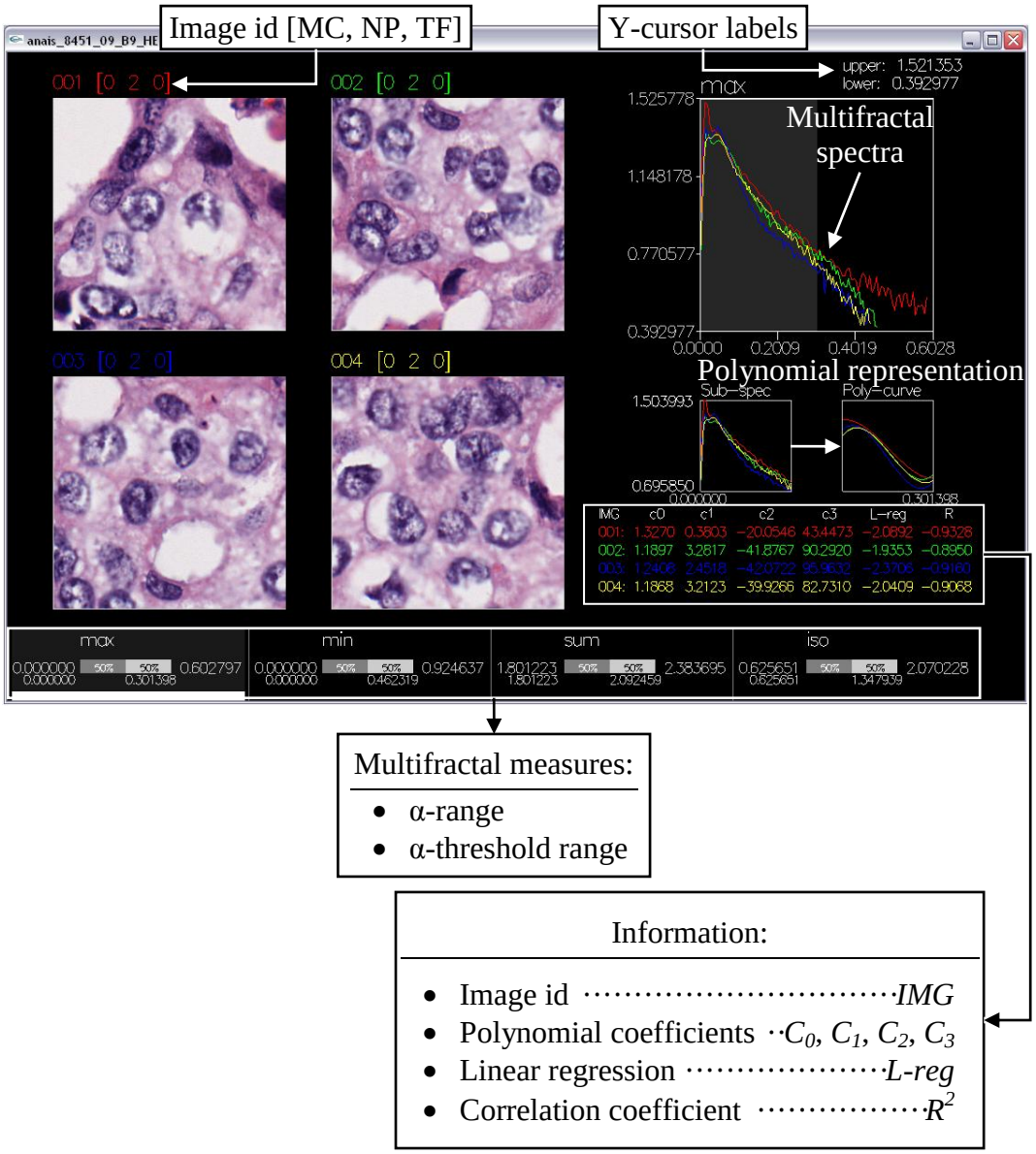

Figure 4-21 Advanced application of visualization for multifractal spectrum

GUI in Figure 4-21 is the advanced version of Figure 4-20; it shows more information about the fractal dimension of the input sub-image frames. An adjustable α-threshold range, in the bottom panel, is introduced and allowed to adjust the display of output based on a particular range of α-values. This enables the visualisation of the spectrum variance in NP or TF scores at a different α-range. The polynomial representations of the multifractal spectra are shown beside the spectrum plot, where the polynomial coefficients are displayed under the plots.

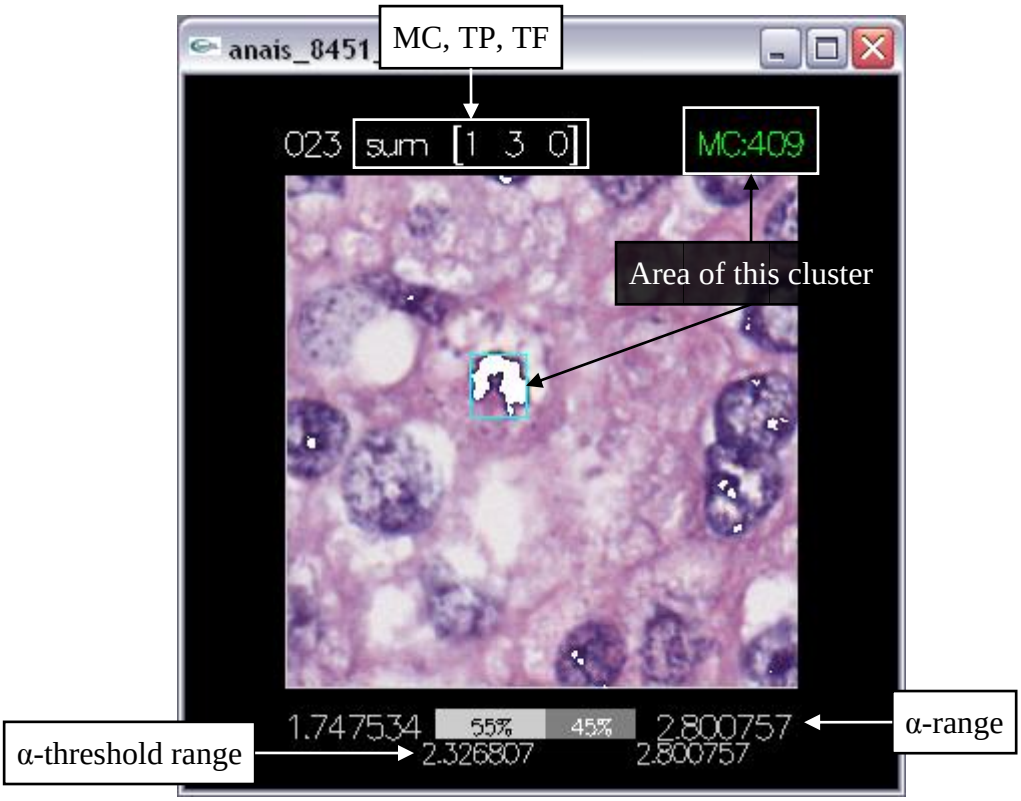

Figure 4-22 Displaying mitotic cell detection

On the other hands, GUI in Figure 4-22 was design to visualise the correlation between mitotic cells and α-values of the pixels. The input sub-image frame is displayed in the middle, while its basic information is located on top. An adjustable α-threshold range shows those pixels with α-values within the α-range in white colour. This helps to identify the pixels with α-values which are related to mitotic cells.

4.6 Summary of Implementation

The process of analysing the histopathological image for breast cancer grading is explained in this chapter. The summary of pre-processing the tissue image using multifractal technique is summarised in Figure 4-23. The local singular coefficients of image are calculated in small image frames of high resolution with the size of 288 × 288 pixels each. It has shown that epithelial and non-epithelial tissues have different multifractal properties.

Figure 4-24 is the summary of the developed methods. The mitotic cells have higher α-values than the other tissue substances in the region; hence, they can be easily segmented. The multifractal dimensions contain the information of NP and TF scores and can be estimated via the slope of the multifractal spectra at the α-sub-range of interest. The evaluations of these methods are discussed in Chapter 5.

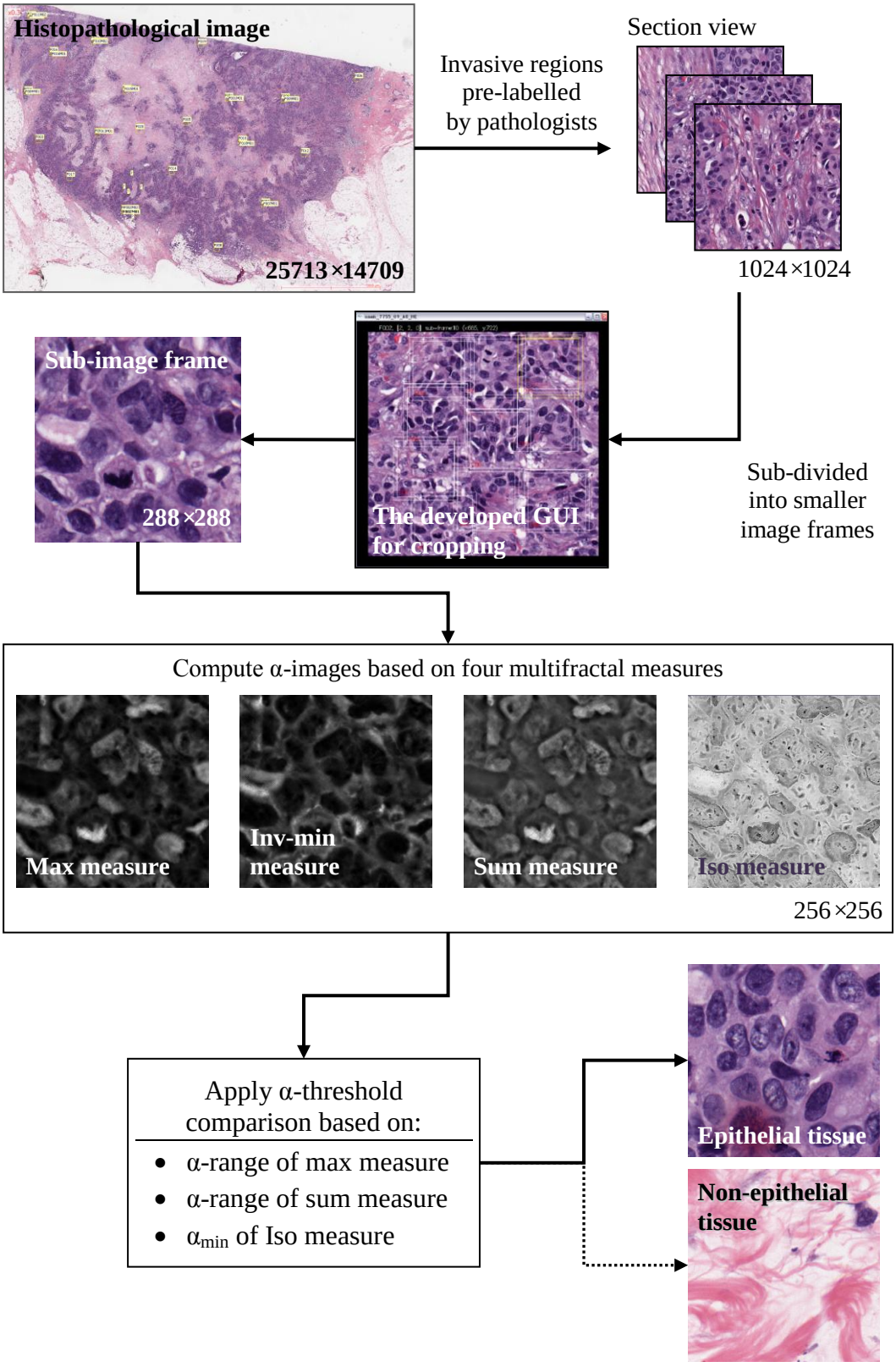

Figure 4-23 Summary of pre-processing the tissue images with multifractal techniques

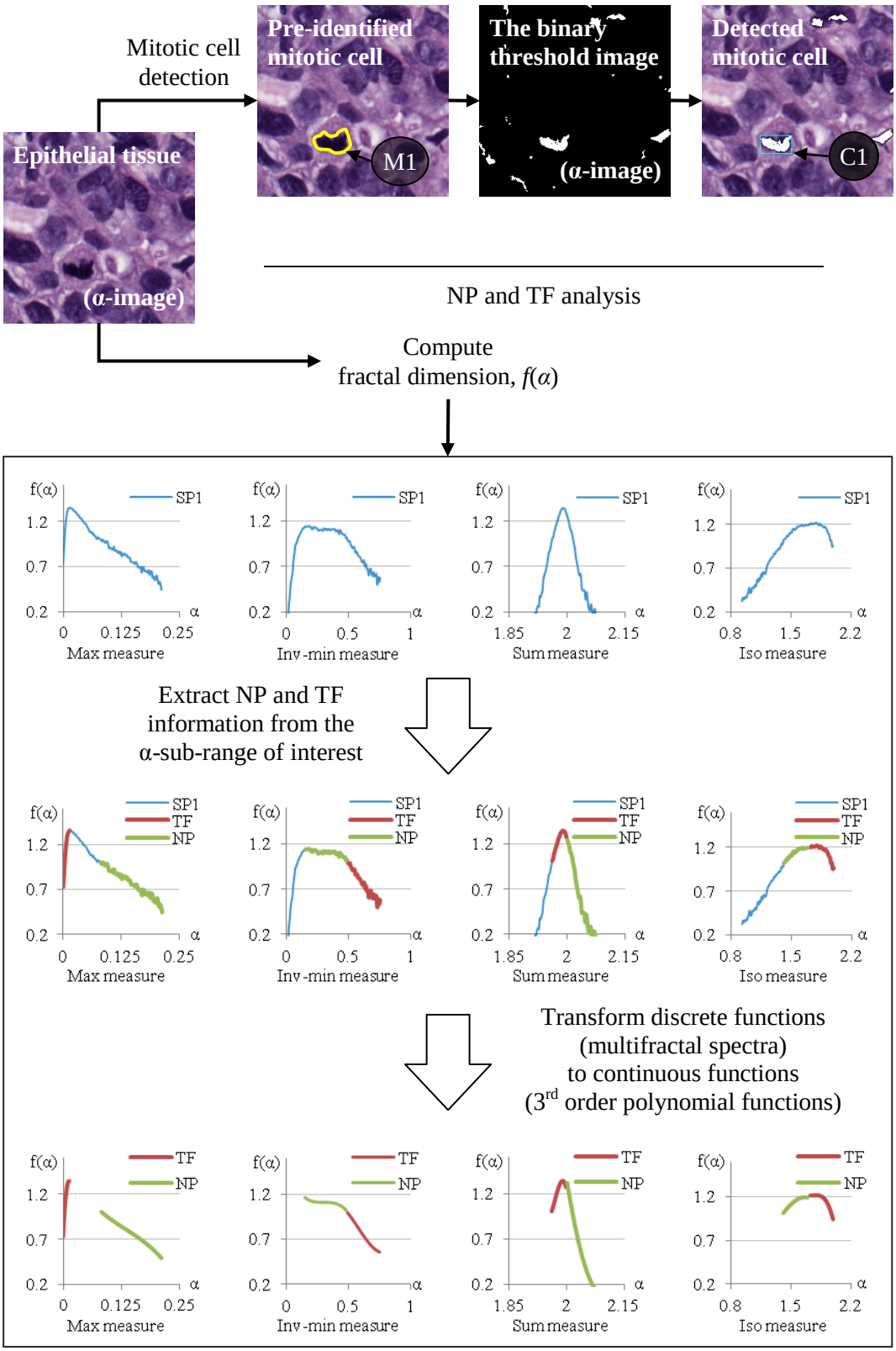

Figure 4-24 Summary of the procedure of breast cancer grading system

Chapter 5:

Results and Discussion

Using different parameters can change the results of a developed method, the evaluations are discussed in this chapter as follows: (1) digital representation of an image with different colour models, (2) parameters of α-threshold comparison for epithelial and non-epithelial type tissue with different magnification scale, (3) detection of mitotic cell with different α-threshold, (4) implementation of NP analysis, and (5) implementation of TF analysis.

5.1 The Effect of Using Different Colour Models

As discussed in Section 3.1, digital image can be represented in several digital formats. The high resolution, high magnification histopathological images can be saved as a 24-bit bitmap format, where each pixel is represented by three integers ranging from 0 to 255, based on the red, green, blue colour model.

Histopathological image is presented with true colour while multifractal method analyses the intensity variation of a pixel. It is important to define the term "*intensity*" of a colour image because it can refer to the intensity value in greyscale or the colour value of a single colour channel. Five colour models were tested: greyscale, hue model [65], red channel, green channel, and blue channel. Let *i* and *j* be the coordinate of the pixel in an image, then the colour representation for these colour models are denoted as follows:

$$colour(i,j) = f\big(r(i,j), g(i,j), b(i,j)\big) \tag{5.1}$$

$$greyscale(i,j) = cR \cdot r(i,j) + cG \cdot g(i,j) + cB \cdot b(i,j) \tag{5.2}$$

$$cR = 0.2989,\ cG = 0.5870,\ cB = 0.1140 \tag{5.3}$$

$$hue(i,j) = \begin{Bmatrix} r(i,j) \geq g(i,j) \geq b(i,j), & h_1(i,j) \\ g(i,j) > r(i,j) \geq b(i,j), & h_2(i,j) \\ g(i,j) \geq b(i,j) > r(i,j), & h_3(i,j) \\ b(i,j) > g(i,j) > r(i,j), & h_4(i,j) \\ b(i,j) > r(i,j) \geq g(i,j), & h_5(i,j) \\ r(i,j) \geq b(i,j) > g(i,j), & h_6(i,j) \end{Bmatrix} \tag{5.4}$$

$$\left.\begin{aligned} h_1(i,j) &= \frac{1}{6} \cdot \frac{g(i,j) - b(i,j)}{r(i,j) - b(i,j)} \\ h_2(i,j) &= \frac{1}{6} \cdot \left(2 - \frac{r(i,j) - b(i,j)}{g(i,j) - b(i,j)}\right) \\ h_3(i,j) &= \frac{1}{6} \cdot \left(2 + \frac{b(i,j) - r(i,j)}{g(i,j) - r(i,j)}\right) \\ h_4(i,j) &= \frac{1}{6} \cdot \left(4 - \frac{g(i,j) - r(i,j)}{b(i,j) - r(i,j)}\right) \\ h_5(i,j) &= \frac{1}{6} \cdot \left(4 + \frac{r(i,j) - g(i,j)}{b(i,j) - g(i,j)}\right) \\ h_6(i,j) &= \frac{1}{6} \cdot \left(6 - \frac{b(i,j) - g(i,j)}{r(i,j) - g(i,j)}\right) \end{aligned}\right\} \tag{5.5}$$

where *r* is the red colour value, *g* is the green colour value, and *b* is the blue colour value. Figure 5-1 illustrates the differences of presenting a colour image in different colour spaces.

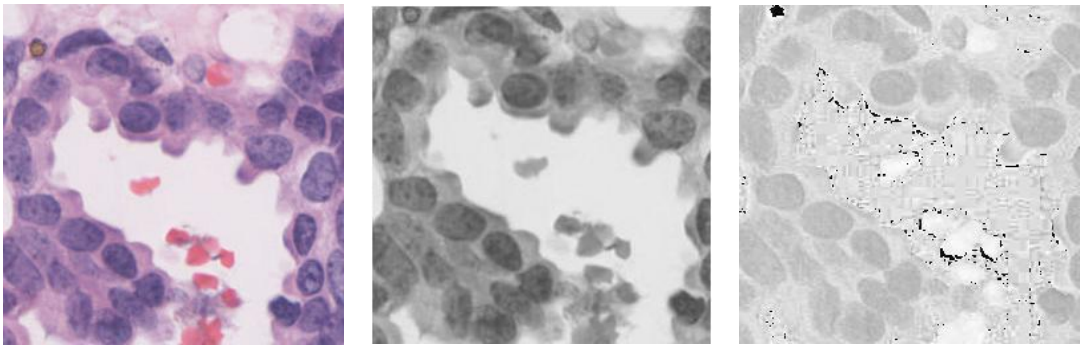

(a) Original RGB (b) Greyscale (c) Hue model

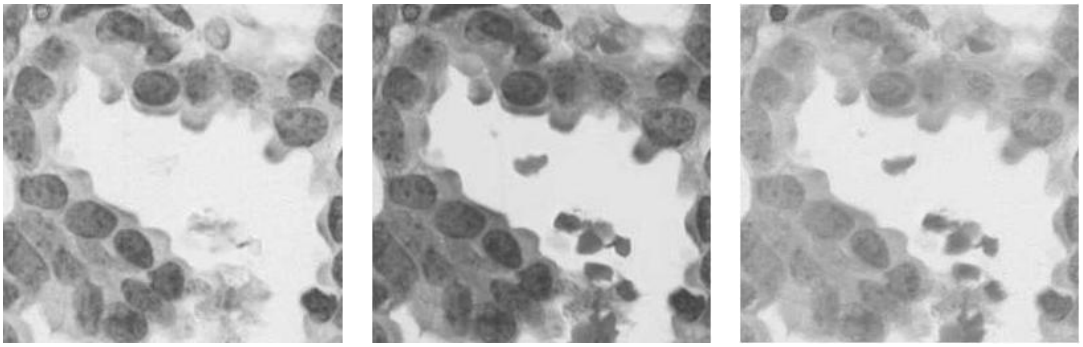

(d) Red channel (e) Green channel (f) Blue channel

Figure 5-1 Examples of an image frame and its presentation in different colour models

The intensity distribution of the cell nuclei's cluster is more uniform in the hue model, where cell nuclei have better outer line. However, hue model can have a mathematical error when a pixel has identical red, green, and blue colour values. Such pixel is treated as $h_1(i, j)$ in Equation 5.4 and can cause a division by zero in Equation 5.5. Hence, pixels with identical red, green, and blue colour values are treated as background and neglected in the calculations. Furthermore, hue model is not an ideal model for breast cancer analysis because the information of tubules is integrated in the background.

The images presented in green channel and greyscale have similar intensities because green value is the dominance in Equation 5.2. Conversely, the intensity distribution of the blue channel is brighter than the other two colour channels. As a result, the segmentation of cell nuclei is more difficult because the edges of the clusters are not clear. On the other hand, bloodstain may be present in a histopathological image. It can be present as background in the red channel because

its red colour value is higher than its green and blue colour values. Since the bloodstain has lower green and blue colour values, it could be mistreated as a cell nucleus in green and blue channels. Therefore, for breast cancer analysis, red channel is the best choice for measuring the intensity variation of an image. The study on the effect of using different colour models to the results of multifractal analysis is further discussed in Section 5.2.

5.2 The Evaluation of the First Stage Classification

Using different colour model for the calculation of Holder exponent has direct impact to the α-range of the α-images. Figure 5-2 illustrates the average α-range of five histopathological samples with magnification scale of ×20.0.

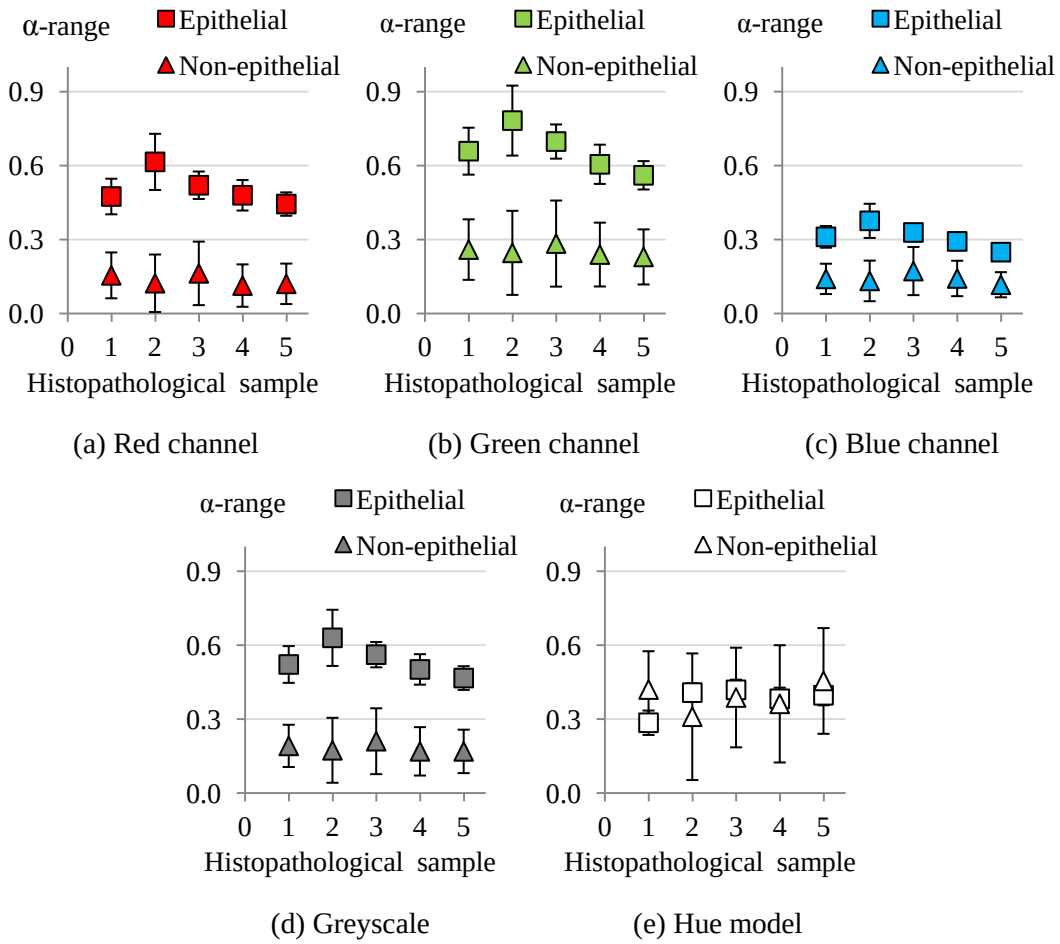

(a) Red channel (b) Green channel (c) Blue channel

(d) Greyscale (e) Hue model

Figure 5-2 The effect of different colour models to the average α-range of sum measure (×20.0)

Clearly, the results have shown that blue channel and hue model were not suitable for multifractal analysis since they cannot show a clear boundary between epithelial and non-epithelial tissues. In contrast, the results from red channel, green channel, and greyscale show potential candidates for calculating Hölder exponent. A further evaluation which studies the effect of using these three colour models on the histopathological image with magnification scale of ×40.0 is shown in Figure 5-3.

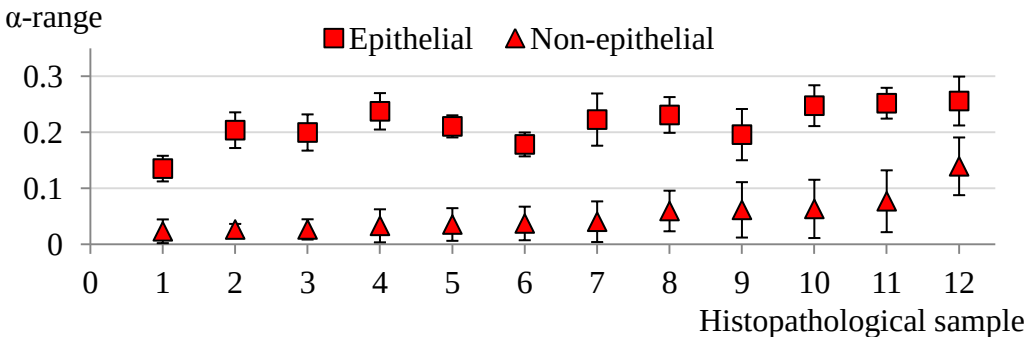

(a) Red channel

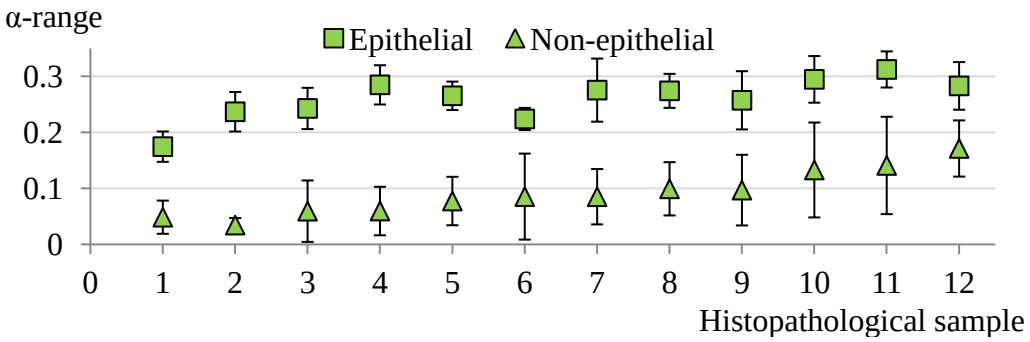

(b) Green channel

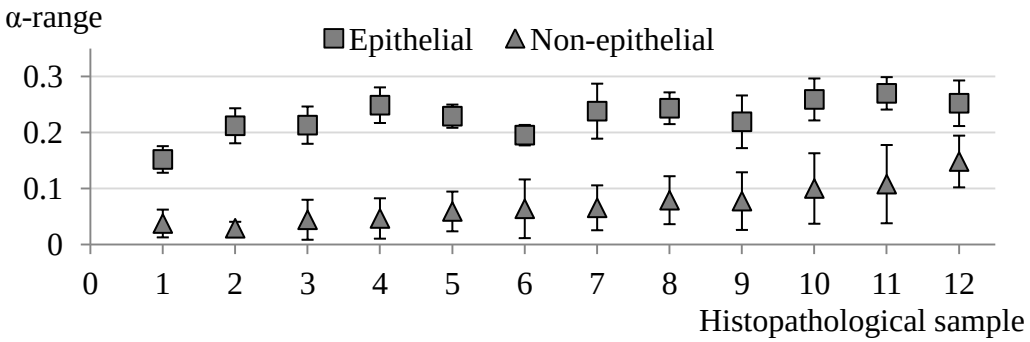

(c) Greyscale

Figure 5-3 The effect of using red channel, green channel, and greyscale to the average α-range of sum measure (×40.0)

Red channel has the largest average gap between epithelial and non-epithelial tissues than green channel and greyscale model; hence, a threshold boundary can easily separate them into two categories.

The α-thresholds for classifying the epithelial and non-epithelial tissue are dependent on the magnification scale of a histopathological image. The magnification scales of the image samples used in this research are ×20.0 and ×40.0. The α-thresholds for classification are listed in Table 5-1.

Table 5-1The α-threshold list for classifying the types of tissue structures

	The α-threshold (α-value)			
	Epithelial type		Non-epithelial type	
	Magnification scale		Magnification scale	
Type of multifractal	× 20.0	× 40.0	× 20.0	× 40.0
α-range of max measure	> 0.3	> 0.1	< 0.3	< 0.1
α-range of sum measure	> 0.3	> 0.1	< 0.3	< 0.1
α_{min} of Iso measure	< 0.8	< 1.2	> 0.8	> 1.2

Before performing a breast cancer diagnosis, a pathologist first labels the histopatological image into three regions: the invasive area, the normal area, and the unknown area. Since the histopathological image has high resolution, the invasive cancerous areas are unlikely to occupy in the whole region. The identification for invasive areas, ROI, is proposed by Huang et al. [20, 64]. A comparison of the developed first-stage classification with the work of Huang et al. is demonstrated in Figure 5-4.

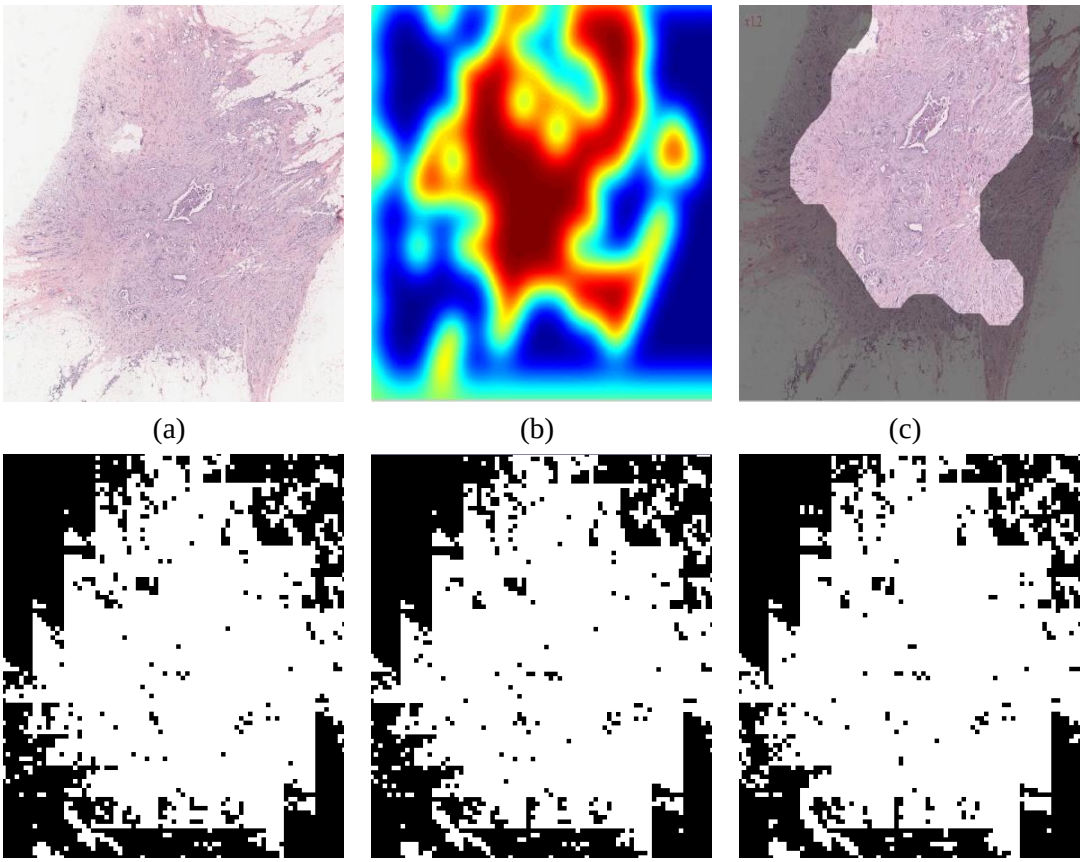

(a) (b) (c)

(d) (e) (f)

Figure 5-4 ROI: (a) original image sample (b-c) result from Huang et al. [20, 64]
(d-f) results obtained from this research: max, sum, Iso measures

Huang et al. defined the ROI as the region in Figure 5-4 (c) inside the grey region. On the other hand, this research detected ROI as regions displayed in white in Figure 5-4 (d), Figure 5-4 (e), and Figure 5-4 (f). Clearly, the ROIs in this research are larger than the ROI from Huang et al.'s.

Huang et al. reported that, with NVIDIA GeForce 9400M GPU acceleration, finding the ROI of an image slide with low resolution required an average computational time of 120 seconds. In contrast, high magnification, high resolution histopathological image slide was used for this comparison which sub-divided Figure 5-4 (a) into 7,007 sub-image frames of size 288 × 288 pixels each. It took a total computational time of 61,189 seconds, about 17 hours (8.733 seconds per sub-image frame), on an Intel Core2 Quad CPU Q6600 at 2.40 GHz. GPU processing has parallel processing capability and has advantage on CPU processing. Moreover, high resolution image was used in this example; the computational time took longer although the area of ROI was larger. Using different types of processing units and resolutions of image slide caused significant variation in the performance of detecting ROI between this research and Huang et al.'s.

5.3 The Evaluation of the Mitotic Cell Detection

The selection of α-threshold and noise threshold can affect the results of mitotic cell detection. A noise cluster is assumed to occupy less than 100 pixels, and it is removed from the results during the computation process. In sum measure, the α-values of mitotic cells were distributed across the second half of the α-range. All potential mitotic cells can be segmented using this unique feature. Cluster with the largest number of pixels after applying α-threshold is considered as a mitotic cell. Therefore, the selection of the α-threshold can affect the outcome.

In this research, 181 sub-image frames containing mitotic cells were selected. A comparison chart for different α-thresholds is shown in Figure 5-5. With an α-threshold of 65% of the α-range, 152 mitotic cells formed the largest clusters in their respective image frames, while 8 mitotic cells were not detected and 21 detected mitotic cells were not found as the largest cluster in their image frames.

In contrast, a higher α-threshold has the risk of not detecting more possible mitotic cells. For instance, with α-threshold of 80%, 97 mitotic cells were not detected because their sizes were smaller than the pre-defined noise threshold.

Although α-threshold of 65% has the best overall results in detecting mitotic cells, α-threshold of 55% was preferred because all mitotic cells could be detected.

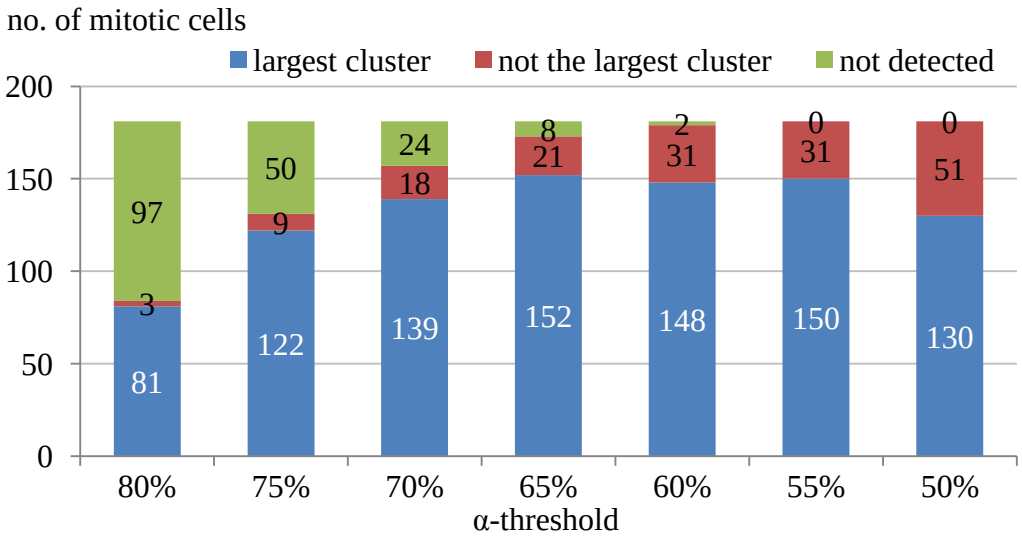

Figure 5-5 The effect of α-threshold on mitotic cell detection

Figure 5-6 illustrates the effect of α-threshold on the area of clusters detected. The decreasing trends show that a lesser amount of pixels are detected at higher α-values. This explains why less mitotic cells were detected with higher α-threshold.

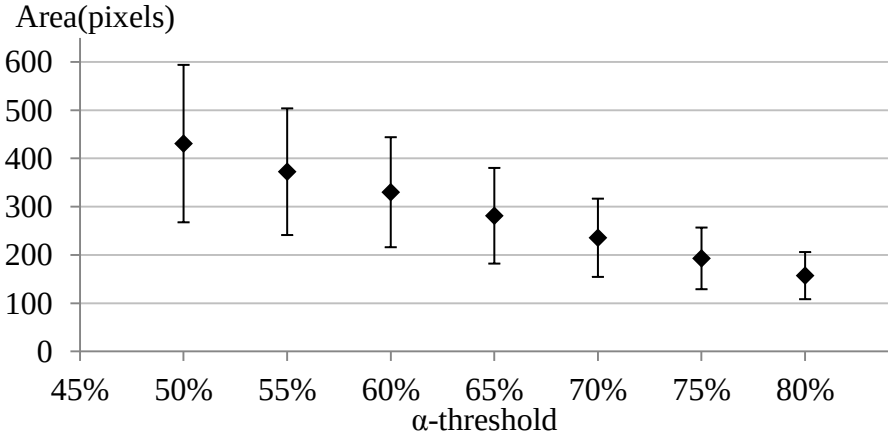

(a) Mitotic cells are the largest cluster

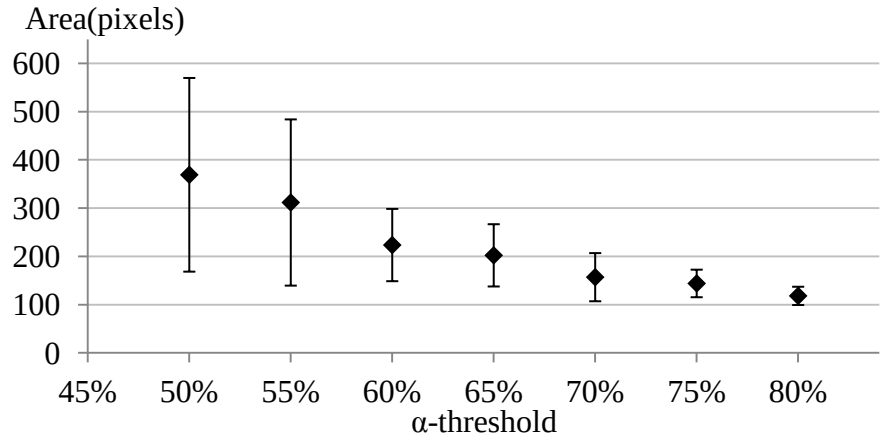

(b) Mitotic cells which are not the largest cluster

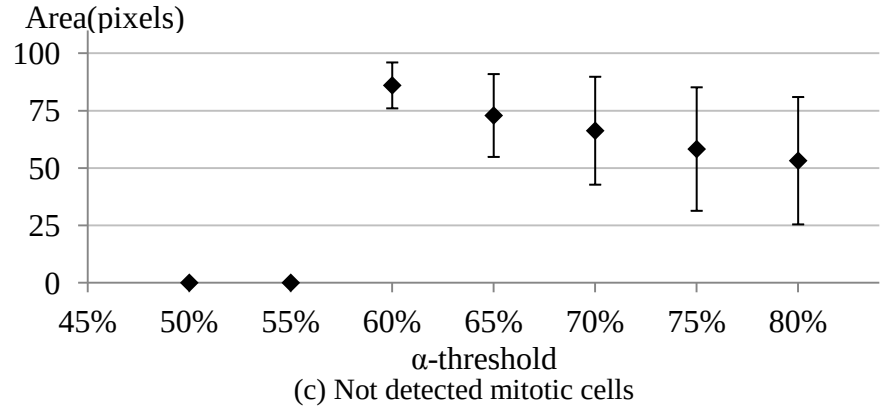

(c) Not detected mitotic cells

Figure 5-6 The effect of different α-thresholds to the average size of the mitotic cells

A mitotic cell is assumed to be the largest cluster detected in the analysis; however, this statement is hardly valid when there are other dominating clusters present in the image frame. An example is illustrated in Figure 5-7 where a mitotic cell has been identified by pathologists. Three clusters remained in the system when the α-threshold was 55% above the α-range. Cluster C1 was recognised as a mitotic cell since it occupied the largest area of 281 pixels, followed by cluster C2 (206 pixels), and the actual mitotic cell C3 (172 pixels). Although the mitotic cell C3 was highlighted, it was not recognised as a mitotic cell due to the presence of larger clusters in this sub-image frame. Since a mitotic cell is unlikely to be long and thin, the system should remove rod-shaped clusters in the binary threshold image as noise.

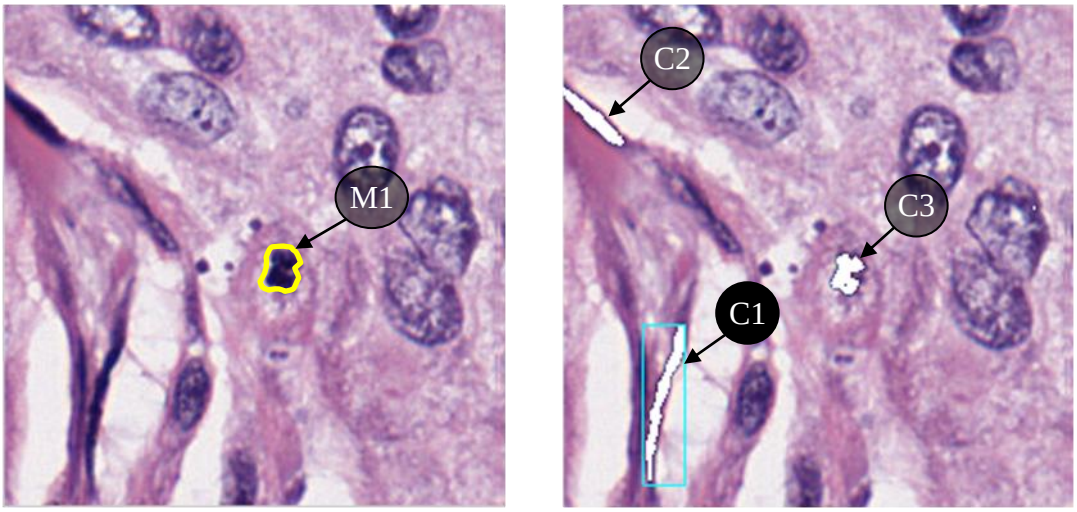

(a) (b)

Figure 5-7 An unexpected behaviour of the system: (a) manually identified mitotic cell, M1 (b) a mistakenly detected mitotic cell, C1

On the other hand, the system could underestimate the level of mitosis when there are more than one mitotic cells present in the image frame. As shown in Figure 5-8, two mitotic cells, M1 and M2, have been identified by pathologists. Although both mitotic cells were the two largest clusters in the image frame, the system detected only one largest cluster as a mitotic cell, C1, and ignored the others. Since the aim of this research is to develop a pre-screening system for the diagnosis

of breast cancer, the system is expected to recognise all possible mitotic cells in available image frames. The five largest clusters in a sub-image frame are suggested to be potential mitotic cells, which will be validated by pathologists.

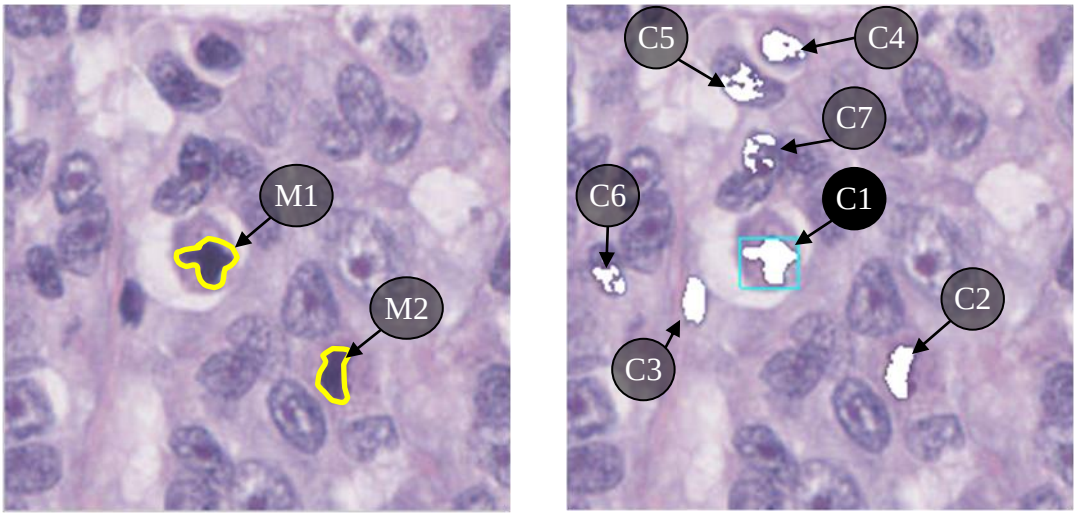

(a) (b)

Figure 5-8 An undesired behaviour of the system: (a) two manually identified mitotic cells, M1 and M2 (b) a detected mitotic cell, C1, the other mitotic cells are omitted

The true positive rate using the method developed in this research was 82.87%, which was an improvement on Kate et al.'s result of 81% [25]. Moreover, the false positive rate found in this research (17.13%) was reasonably lower than that obtained by Kate et al. (30%) [25] and Beliën et al. (19%) [26]. For mitotic cell detection, the multifractal technique is a better tool than the growing region technique.

The results of this research are not comparable with the results performed by Dalle et al. since this research focused on detecting individual mitotic cell, whereas Dalle et al. related their results with the MC score of NGS [27].

5.4 The Evaluation of the NP Analysis

During the exploration of NP analysis, it was assumed that the multifractal spectrum could describe the characteristics of the NP scores. In fact, a section of the multifractal spectrum had shown uniqueness in the geometric features of each NP score, as demonstrated in Figure 4-15. Based on this discovery, the multifractal spectra of sub-image frames with same NP score must be similar and are unique from other spectra of different NP scores. A classification approach was applied to verify this hypothesis of NP analysis.

As mentioned in Section 4.4.3, multifractal spectrum is a discrete function and can be transformed into a polynomial equation. A reference spectrum is a mean spectrum of a set of multifractal spectra, and can be calculated by averaging the polynomial coefficients of the multifractal spectra. Since an NP score was assumed to have a unique spectrum, a histopathological image should have three different reference spectra, each representing an NP score of NGS. Ideally, healthy tissues should have their specific reference spectrum, but only the sub-image frames with tumour tissues were used in the analysis of NP. In this research, healthy tissues have no reference spectrum.

Furthermore, the α-sub-range which describes the NP information of the multifractal spectrum varies between sub-image frames. For each NP score, a reference α-sub-range can be calculated by averaging the α-sub-range of every sub-image frames with the same NP score in the histopathological image.

Given that four multifractal measures were applied for NP analysis, each measure has three unique reference spectra and reference α-sub-ranges respectively. As a result, a histopathological image has 12 reference spectra and 12 reference α-sub-ranges.

The multifractal spectrum of a sub-image can then be compared with the reference spectrum using three measurements: a distance metric, a gradient difference metric, and a hybrid measure that combines both distance and gradient difference metrics. Distance metric is a function that measures the distance between

the multifractal spectra of an α-image and the reference spectrum. Let ω be a type of multifractal measure and τ be the NP score for a reference spectrum, the distance metric is calculated as followed:

$$\left.\begin{array}{c} NP\ score_{\omega,dist} = \{1,2,3\} = minimum\left(dist_{\omega,\tau}\right), \\ \tau = 1,2,3 \\ \omega\ =\ \max, \text{inv} - \min, \text{sum, Iso measures} \end{array}\right\} \tag{5.6}$$

$$dist_{\omega,\tau} = \sum_{i=1}^{m}\left(a_{\omega,\tau,i}^2 + b_{\omega,\tau,i}^2\right) \tag{5.7}$$

$$a_{\omega,\tau,i} = \alpha_{spec,\omega,i} - \alpha_{ref,\omega,\tau,i} \tag{5.8}$$

$$b_{\omega,\tau,i} = f\left(\alpha_{spec,\omega,i}\right) - f\left(\alpha_{ref,\omega,\tau,i}\right) \tag{5.9}$$

Consequently, as defined in Equation 5.6, a sub-image frame is classified as NP Score 2 if its multifractal spectrum is closer to the reference spectrum of NP Score 2 than the other two reference spectra.

Similarly, since the multifractal spectrum can be transformed into a polynomial equation $p(\alpha)$, the gradient of the curve can be easily calculated by differentiating the polynomial equation $p(\alpha)$ into $p'(\alpha)$ with respect to α. Then, the gradient difference metric calculates the gradient similarity of the multifractal spectrum with the reference spectrum, expressed as follows:

$$\left.\begin{array}{c} NP\ score_{\omega,grad} = \{1,2,3\} = minimum\left(grad_{\omega,\tau}\right), \\ \tau = 1,2,3 \\ \omega\ =\ \max, \text{inv} - \min, \text{sum, Iso measures} \end{array}\right\} \tag{5.10}$$

$$grad_{\omega,\tau} = \sum_{i=1}^{m}\left(s'_{\omega,i} - r'_{\omega,\tau,i}\right)^2 \tag{5.11}$$

$$s'_{\omega,i} = p'_{spec,\omega}(\alpha_{spec,\omega,i}) \tag{5.12}$$

$$r'_{\omega,\tau,i} = p'_{ref,\omega,\tau}(\alpha_{ref,\omega,\tau,i}) \tag{5.13}$$

The hybrid measure returns a result of either true (1) or false (0) for a sub-image frame with an NP score that combines the results of both distance metric and gradient difference metric, where:

$$hybrid_{\omega,\tau} = \left(dist_{\omega,\tau} \wedge grad_{\omega,\tau}\right) \tag{5.14}$$

In other words, a sub-image frame is classified as NP Score 2 only when both metrics agree that it is NP Score 2.

The classification results for NP analysis using four different multifractal measures is summarised in Table 5-2. These results were contributed by 14 histopathological images which contained 150 sub-image frames of NP Score 1, 970 sub-image frames of NP Score 2, and 1,550 sub-image frames of NP Score 3. The highlighted cells represent the percentage of correct NP score predictions. Clearly, the correct predictions are dominant, but are still unsatisfactory.

Table 5-2The classification results for NP scores using different multifractal measures

Measure	Actual NP Score	Predicted NP Score								
		Gradient difference			Distance difference			Hybrid measure		
		1	2	3	1	2	3	1	2	3
Max	1	58.00	36.67	5.33	53.33	38.67	6.00	48.00	32.67	2.00
	2	1.55	62.47	35.98	3.20	57.22	39.59	1.13	49.59	28.35
	3	0.84	38.65	60.52	1.74	41.36	56.90	0.39	30.71	49.23
Inv-min	1	65.33	34.67	0.00	64.67	35.33	0.00	64.00	34.00	0.00
	2	2.78	57.94	39.28	1.86	63.40	34.74	1.55	51.65	28.56
	3	1.10	36.90	62.00	0.71	38.71	60.58	0.65	28.65	52.26
Sum	1	77.33	20.67	2.00	78.00	20.67	1.33	77.33	20.67	1.33
	2	2.27	71.65	26.08	2.27	71.96	25.77	2.27	71.44	25.57
	3	0.07	39.94	60.00	0.00	40.26	59.74	0.00	39.74	59.49
Iso	1	44.67	30.00	25.33	52.00	30.00	0.67	44.67	26.00	0.67
	2	8.56	43.40	48.04	3.81	47.32	48.87	2.89	42.27	44.85
	3	4.13	29.94	65.94	1.23	31.87	66.90	1.23	28.65	64.07

The hybrid measure was introduced to the system to provide a double assurance for NP estimation. However, when using the hybrid measure, the NP score of a sub-image frame cannot be estimated in the condition of disagreement between two metrics. For this reason, 20% of the sub-image frames with max measure were not classified.

A voting system is then applied for the NP analysis. This voting system let all four multifractal measures to vote for the NP score of a sub-image frame. For instance, a sub-image frame is suggested to have a particular NP score if it gained more agreeing votes from the multifractal measures. Figure 5-9 shows the result of the receiver operating characteristic (ROC) curves for NP classification. Each mark on the curve represents the true positive rate against the false positive rate of the voting results. The mark with single vote has high true positive rate and high false negative rate. Conversely, both true and false positive rates are low for sub-images with four agreeing votes from all four multifractal measures. The ROC curves show that the numbers of sub-image frames with more than two votes are low; hence the NP score of a sub-image frame can be estimated when it gains two agreeing votes from any two multifractal measures.

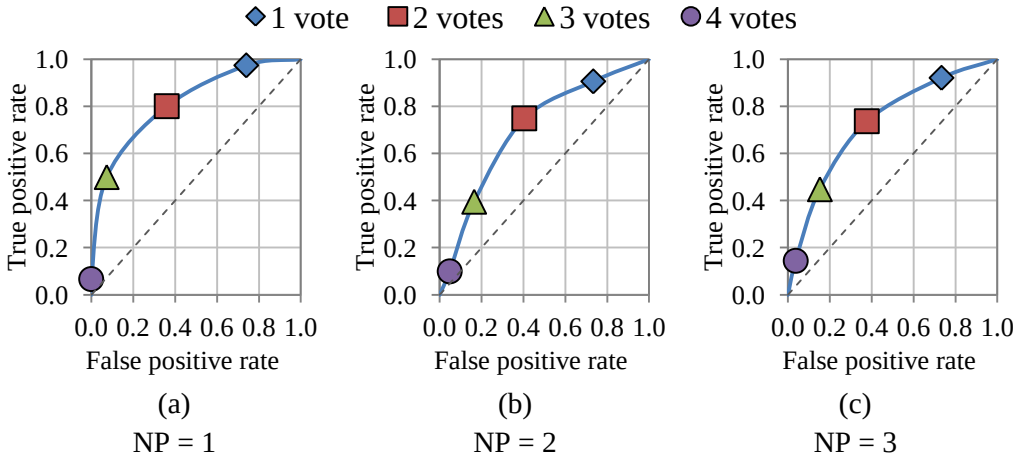

Figure 5-9 The ROC curves for NP classification

The classification results for the NP scores based on the agreeing votes of any two multifractal measures are shown in Table 5-3. A sub-image frame may be

assigned with two different NP scores if there were two different agreements from two pairs of multifractal measures.

Table 5-3The classification results for NP scores based on the voting system of any two multifractal results

Actual NP Score	Predicted NP Score			
	1	2	3	Total
1	80.00	35.33	0.67	116.00
2	2.37	74.85	38.04	115.26
3	0.00	37.68	73.68	111.35

Hence, the system over-classified 13% of the total sub-image frames although the overall correct classification rate and false classification rate were 74.46% and 38.58%, respectively. Based on this, the overall correct and false classification rates are calculated as follows:

$$correct = \frac{T_1 \cdot NP_1 + T_2 \cdot NP_2 + T_3 \cdot NP_3}{NP_1 + NP_2 + NP_3} \tag{5.15}$$

$$false = \frac{F_1 \cdot NP_1 + F_2 \cdot NP_2 + F_3 \cdot NP_3}{NP_1 + NP_2 + NP_3} \tag{5.16}$$

$$\left.\begin{matrix} NP_1 = 150 \\ NP_2 = 970 \\ NP_3 = 1{,}550 \end{matrix}\right\} \tag{5.17}$$

where NP_1, NP_2, and NP_3 are the numbers of sub-image frames, T_1, T_2, and T_3 are the correct predicted rates, in this case (Table 5-3), they are:

$$\left.\begin{matrix} T_1 = 0.8000 \\ T_2 = 0.7485 \\ T_3 = 0.7368 \end{matrix}\right\} \tag{5.18}$$

On the other hand, F_1, F_2, and F_3 are the false classification rate:

$$\left.\begin{matrix} F_1 = 0.3533 + 0.0067 \\ F_2 = 0.0237 + 0.3804 \\ F_3 = 0.0000 + 0.3768 \end{matrix}\right\} \tag{5.19}$$

A weight factor was introduced to prevent the conflicts during the voting process. From Table 5-2, the prediction based on sum measure has better accuracy

than the other three multifractal measures. Therefore, sum measure is more reliable, so its weight factor is higher than the other three multifractal measures. The weight factors w_1, w_2, w_3, and w_4 are defined as follows:

$$\left.\begin{array}{c} w_1 v_{\max,\tau} + w_2 v_{\text{inv}_{\min},\tau} + w_3 v_{\text{sum},\tau} + w_4 v_{\text{iso},\tau} = \#\text{ of } vote_\tau \\ \tau = 1,2,3 \end{array}\right\} \tag{5.20}$$

$$w_1 + w_2 + w_3 + w_4 = 1 \tag{5.21}$$

$$w_1 = 0.2250;\ \ w_2 = 0.2550;\ \ w_3 = 0.2625;\ \ w_4 = 0.2575 \tag{5.22}$$

$$v_{\omega,\tau} = \begin{cases} 1 \\ \\ 0 \end{cases},\ hybrid_{\omega,\tau} \tag{5.23}$$

where $v_{\omega,\tau}$ represents a vote based on the hybrid measure of the NP scores τ and the multifractal measures ω: max, inv-min, sum, and Iso measures respectively. The values of weight factors are rationally assigned to give multifractal measures a set of leading factors in descent order of sum, Iso, inv-min, and max measures.

The ROC curves for NP score classification involving weight factors are illustrated in Figure 5-10. Although the true positive rates had slightly reduced, the false positive rates for single vote had significantly dropped.

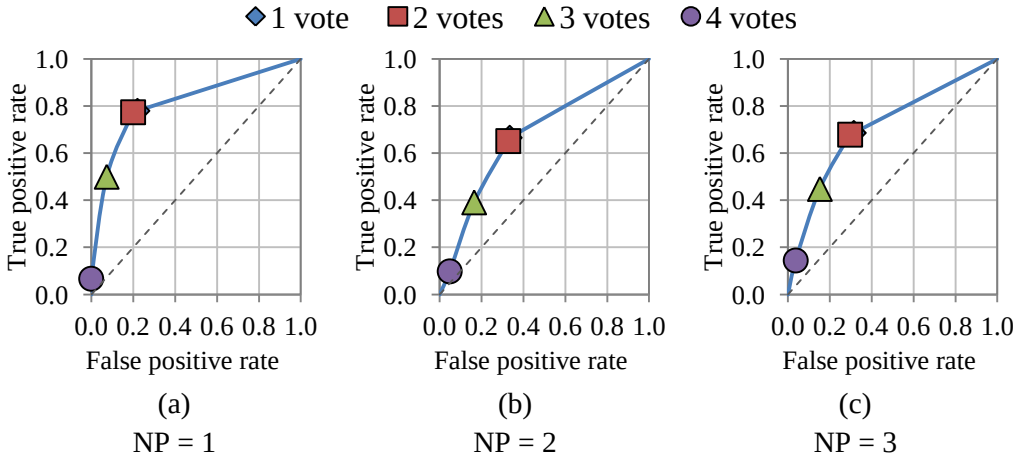

Figure 5-10 The ROC curves for NP classification after introducing the weight factors

Table 5-4 shows the classification results of the voting system for NP scores after applying the weight factors. The conflict caused by two different agreements

that suggested different NP scores had been solved. The weight factors can increase the percentage vote of the more favoured NP score. Although 2.36% of the whole samples were not classified as any NP score, the overall correct classification rate was 67.38% (see Equation 5.15), giving 30.26% (see Equation 5.16) of false classification rate.

Table 5-4The classification results for NP scores based on the combination of any two multifractal results after introducing the weight factors

Actual NP Score	Predicted NP Score			
	1	2	3	Total
1	77.33	20.00	0.00	97.33
2	2.16	65.15	30.62	97.94
3	0.00	29.68	67.81	97.48

On the other hand, a problem was encountered when the multifractal spectrum of Iso measure does not have a local maximum in the α-sub-range of [*1.40*, *1.95*]. As shown in Figure 5-11, both spectra assumed the global maxima in the α-sub-range of interest were the local maxima; hence the analysis for such spectra failed. The local maxima which exist in the α-sub-range of interest can hardly be noticed because the spectra are transformed into smooth third order polynomial equations. Increasing the order of polynomial can help to solve this problem, but also increase the complexity of computation. Therefore it was not implemented during this research.

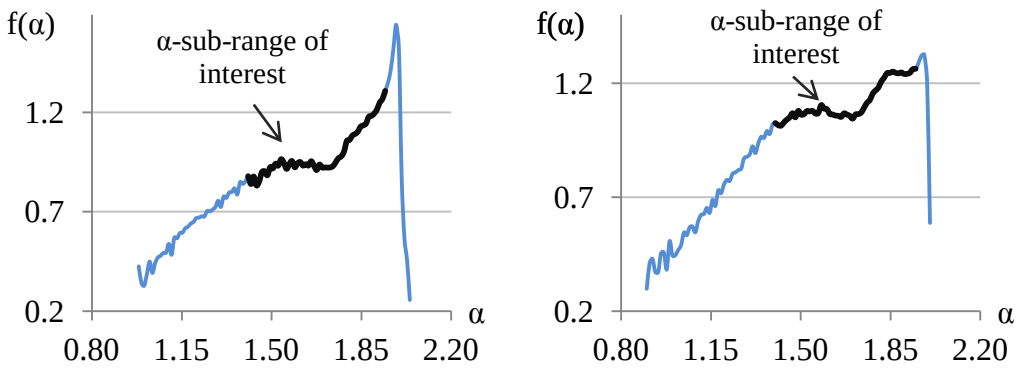

Figure 5-11 Two examples of α-sub-range with undeterminable local maxima

Only Dalle et al. presented the results related to NP score. They had six medical tests in which all three cases of NP Score 2 and a case of NP Score 3 was correctly classified. Meanwhile, two cases of NP Score 3 were underestimated as NP Score 2 [27]. However, the results of Dalle et al.'s study are not convincing enough due to the small amount of samples tested.

Although the overall accuracy of NP analysis was lower than 70% while obtaining a high false classification rate, the performance of this system is reasonably acceptable. Dalle et al. mentioned that a medical case required further attention if it had an NP Score of 2 or 3 [27]. Comparing Dalle et al.'s results with Table 5-4, this system raised a 20.00% chance of causing a false alarm for NP Score 1 and a possible loss of 4.22% of NP Score 2 cases. Besides, 30.63% of NP Score 2 cases were overestimated; 29.68% of NP Score 3 cases were underestimated as Score 2 while 2.52% of NP Score 3 were not detected. The assumption that the multifractal spectrum contains the information of NP score is valid although further study is required to improve the accuracy rate.

5.5 The Evaluation of the TF Analysis

The TF analysis used similar classification approach and hypothesis which was explained in Section 5.4. There were only three histopathological images with TF scores labelled by pathologists. In this research, 160 sub-image frames were labelled TF Score 1, 60 sub-image frames were labelled TF Score 2, and 380 sub-image frames were identified as TF Score 3. The classification results for TF scores using different multifractal measures are shown in Table 5-5. The highlighted cells represent the percentage of correct TF score predictions.

Table 5-5The classification results for TF scores using different multifractal measures

Measure	Actual TF Score	Predicted TF Score								
		Gradient difference			Distance difference			Hybrid measure		
		1	2	3	1	2	3	1	2	3
Max	1	35.63	37.50	26.88	13.75	63.13	23.13	12.50	31.88	16.88
	2	11.67	56.67	31.67	1.67	60.00	38.33	1.67	50.00	28.33
	3	29.21	6.32	64.47	15.53	53.26	79.21	9.74	5.00	58.68
Inv-min	1	53.13	41.25	5.63	57.50	40.63	1.88	49.38	38.88	1.25
	2	35.00	51.67	13.33	34.67	50.00	18.33	26.67	45.00	13.33
	3	19.21	14.74	66.05	23.68	16.58	59.74	15.53	11.58	55.53
Sum	1	63.13	32.50	4.38	67.38	31.25	4.38	63.13	31.25	4.38
	2	21.67	68.33	10.00	21.67	68.33	10.00	21.67	68.33	10.00
	3	3.68	19.21	77.11	3.68	19.21	77.11	3.68	19.21	77.11
Iso	1	25.00	31.25	43.75	54.38	33.13	12.50	23.13	31.25	12.50
	2	28.33	56.67	15.00	35.00	58.33	6.67	26.67	56.67	6.67
	3	8.68	30.26	61.05	3.32	31.32	62.37	6.32	30.00	60.79

As described in the Section 5.4, the voting system can be unreliable when two pairs of multifractal measures suggested different TF scores. Weight factors are applied to address the issue. Figure 5-12 shows the ROC curve for TF classification after applying the weight factors. The ROC curve of TF Score 1 closely lies on the diagonal line, which indicated the accuracy rate was only slightly above 50%.

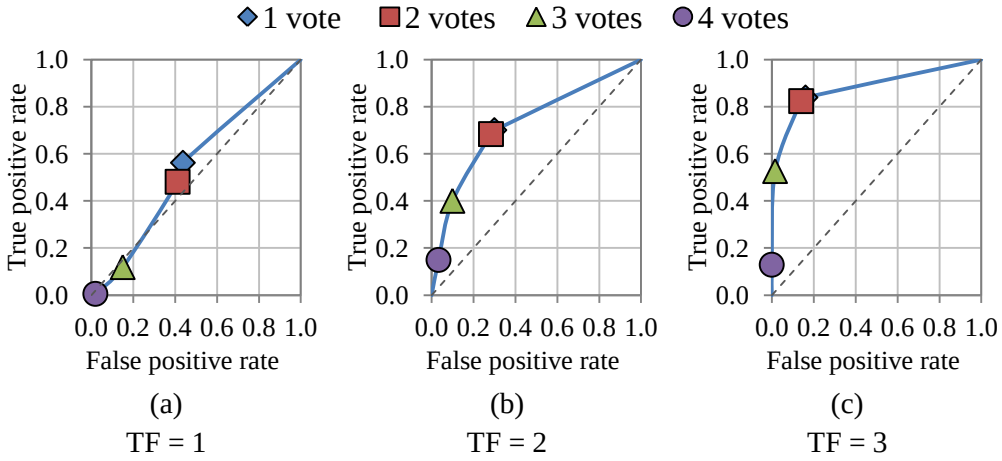

Figure 5-12 The ROC curve for TF classification after introducing the weight factors

The classification results for TF that received two votes from the voting system are as shown in Table 5-6. Overall, 5.5% of sub-image frames were not classified because they did not gain at least two votes from the multifractal measures. By applying Equation 5.15 and Equation 5.16 to Table 5-6, the resulting positive accuracy rate for this system is 71.82%, with 22.67% false classification rate. The positive accuracy rate for sum measure (in Table 5-5) was 72.50% (see Equation 5.15) and the false classification rate was 27.17% (see Equation 5.16). Although sum measure has higher positive accuracy rate than the voting system, the voting system is preferred because the false classification rate was lower than that of sum measure.

Table 5-6The classification results for TF scores based on the combination of any two multifractal results after introducing the weight factors

Actual TF Score	Predicted TF Score			
	1	2	3	Total
1	48.13	38.75	2.50	89.38
2	16.67	68.33	11.67	96.67
3	3.16	10.79	82.37	96.32

The true positive rate for TF Score 1 was low because a tubule may be large in size. It is possible to have a TF which occupies the majority space of a sub-image frame. Hence, the analysis for such TF is inaccurate. A possible solution

is to increase the size of the sub-image frame with a trade-off of increasing the computational resources.

Instead of presenting the single criterion of TF score, Petushi et al. have shown their results in equivalent NGS grade [36]. Therefore, the comparison of the effectiveness between TF analysis methods is not feasible.

Although the method developed by Dalle et al. indicated that the biopsy sample with TF Score 1 matched with pathologist' justifications, other biopsy samples pre-labelled as TF Score 3 were underestimated [27]. The developed system can correctly classify 82.37% of TF Score 3 and 68.33% of TF Score 2, while maintaining 13.95% and 28.34% false positive. However, the positive true rate for TF Score 1 was 48.13% and received 41.25% false positive along with 10.61% of the TF scores not being determined.

5.6 Summary of Results

The summary of data collected from the developed methods is presented in Table 5-7. The overall results based on multifractal technique have statistical relationship with breast cancer grading. Therefore, to improve the system for a better diagnosis tool, some of the future developments are suggested in Section 6.2.

Table 5-7Overall accuracy rate of the developed methods for each NGS criterion

NGS Criterion	Overall accuracy (%)			No. of samples tested	Condition
	True	False	Not detected		
MC	82.87	17.13	0.00	181	– Above α-threshold of 55% α-range, based on sum measure
NP	67.38	30.26	2.36	2,670	– Hybrid measure (gradient and distance metrics) – Voting system based on four multifractal measures with weight factors
TF	71.82	22.67	5.50	600	

Chapter 6:

Conclusion and Future Work

6.1 Conclusion

Breast cancer is one of the most deadly cancers for women, which has been recorded in many countries. According to the increasing incidence rate of breast cancer reported worldwide, early cancer detection and treatment play a major role in increasing the chances of recovery from the disease. Nottingham Grading System (NGS) is the standard grading procedures used in breast cancer assessment; it focuses on three criteria: Mitotic Count (MC), Nuclear Pleomorphism (NP), and Tubule Formation (TF). Each criterion can be assigned with 3 scores, and the final equivalent NGS grade is the summation of all three criteria.

Breast tissue samples of patients are taken for biopsy; pathologists need to assess hundreds of tissue samples under the microscope every day. The NGS grade of tissue samples are based on the deviation of the cell structures from normal tissues. Low agreement for medical cases commonly occurs between pathologists because they exam breast tissue samples based on their experience and opinion. Hence, the evaluation of breast cancer grading is a subjective, manual, and time-consuming process.

Digital high resolution and high magnification histopathological images are commonly used for extracting useful structural information. With the rapid growth in computer hardware technologies, many computer science researches have

focused on computer aided diagnosis systems to develop a standard and quantitative measurement for breast cancer assessment. The algorithms for automatic and semi-automatic diagnosis system have been proposed to provide pre-screening devices for pathologists.

This research received medical data from Image & Pervasive Access Lab (IPAL), from Singapore, who focuses on developing a "cognitive virtual microscopic framework" for breast cancer grading. Methods of a computer visual system have been progressively developed by IPAL; a new approach for breast cancer grading was proposed to study the feasibility of applying multifractal techniques on this specific application.

Multifractal refers to configurations with statistical multiple-level of self-similarity. Cell and tissue structures are known to have multifractal characteristics. In fact, multifractal formalism is an effective tool for biomedical image processing; analysis based on this method has been widely used in several medical applications.

The local singularity coefficient, α-value, describes the local variation of an intensity-based measure within the neighbourhood of a pixel. There are four commonly used intensity measures in multifractal analysis: maximum measure, inverse-minimum measure, summation measure, and Iso measure. Fractal dimension (multifractal spectrum) describes the geometrical properties of the local singularity coefficients of an image.

In this research, the relationship between various multifractal measures of cell structures in tissue samples and the corresponding pleomorphic scores (MC, NP, and TF) pre-assigned by pathologists was investigated. Several quantitative evaluations were presented to measure the effectiveness of using multifractal techniques for grading the tissues of breast cancer tumours.

In the analysis of MC, a mitotic cell is darker and smaller than other cell nuclei; it also has higher α-values which can be segmented. A cluster which occupies more than 100 pixels with α-values above 55% of the α-range in the cell

region is defined to be a potential mitotic cell. Based on this argument, all 181 pre-identified mitotic cells were computationally detected, and 150 of these mitotic cells were found to be the largest cluster in their corresponding sub-image frames.

The information of NP and TF scores can be extracted from the multifractal spectra of the sub-image frames. Multifractal spectra with the same NP or TF scores have similar geometrical features and curves. Two spectra are similar when they have similar gradient and are of short distance apart. The multifractal spectra based on four multifractal measures have these geometrical features in the respective α-sub-ranges of interest.

There were 2,670 sub-image frames pre-labelled with three levels of NP scores by pathologists. The system has classified 67.38% of sub-image frames with the correct NP scores, 30.26% were wrongly classified, with a total of 2.36% net loss. On the other hand, 600 sub-image frames with three different TF scores were pre-labelled by pathologists. Although a net loss of 5.50% was found, 71.82% of sub-image frames were correctly classified while maintaining a false rate of 22.67%.

A medical case required extra notice if it was assigned with NGS Grade II (total score 6-7) or Grade III (total score 8-9). The developed methods are not yet ready for practical application, but majority mitotic cells were detectable and sub-image frames with Score 2 and Score 3 of NP and TF were correctly estimated by the system. Further study is required for this system to develop a more effective, efficient, and reliable breast cancer prognosis tool.

6.2 Future Work

The results presented in this thesis show that multifractal analysis could be a valuable tool in the processing of tissue images for identifying irregularities in the cell structure and in estimating the NP and TF scores. Some possible enhancements and future research directions are outlined as below:

1. Integrate the result from the developed methods

The final equivalent grade of NGS is the combined scores of all three criteria. This master studies only focused on the feasibility of using multifractal analysis in breast cancer grading, where each criterion was separately handled by a single algorithm. Future work could focus on integrating the results from all three developed systems in order to provide a complete NGS grading system.

2. Apply genetic algorithm for α-threshold selection

The α-thresholds of the first stage classification are manually found for magnification scale of ×20.0 and ×40.0. An automatic adaptive α-threshold selection system, using the genetic algorithm, can be useful when different magnification input samples are available. This reduces the participation from users, hence being more time-conserving and avoiding subjective judgements.

3. Implement a shape detection function

Kate et al. and Beliën et al. mentioned that mitotic cells have hairy outline which can be detected as a unique contour feature. At present, majority mitotic cells were found because they were the largest clusters in their thresholded α-image. An automatic shape recognition algorithm can improve the accuracy of mitotic cells detection by eliminating cells without hairy feature.

4. Provide actual MC score

The method of detecting mitotic cells was studied in this research. However, it has not been related with MC score because MC score is obtained based on the number of mitotic cells found in 10 HPF. It is recommended that MC score can be calculated by converting a section of image (in terms of pixels) into HPFs.

5. Improve the accuracy of NP and TF score

Currently, the correct estimation rates for NP and TF were 67.38% and 71.82% respectively. The system could be improved to increase its accuracy and reliability.

6. Standardise NP and TF reference spectra

Currently, the reference spectra were exclusive for their input histopathological images; these reference spectra were incompatible for different medical samples. Global reference spectra for NP and TF are required in future development to provide standard measurements in breast cancer pre-screening applications.

7. Introduce multi-scale techniques

The multifractal analysis attempted in this research could be combined with multi-scale techniques (for example, wavelets) to further characterise the features of interest at different resolutions.

References:

[1] C. M. Rubin, "The Genetic Basis of Human Cancer," *Annals of Internal Medicine,* vol. 129, p. 759, November 1 1998.

[2] J. Ferlay, H. Shin, F. Bray, D. Forman, C. Mathers, and D. Parkin. (2008, October). *GLOBOCAN 2008: Cancer Incidence and Mortality Worldwide (v1.2 ed.)* [Internet]. Available: http://globocan.iarc.fr

[3] A. Jemal, F. Bray, M. M. Center, J. Ferlay, E. Ward, and D. Forman, "Global cancer statistics," *CA: A Cancer Journal for Clinicians,* vol. 61, pp. 69-90, 2011.

[4] R. Siegel, E. Ward, O. Brawley, and A. Jemal, "Cancer statistics, 2011," *CA: A Cancer Journal for Clinicians,* vol. 61, pp. 212-236, 2011.

[5] A. Jemal, M. M. Center, C. DeSantis, and E. M. Ward, "Global patterns of cancer incidence and mortality rates and trends," *Cancer Epidemiology Biomarkers Prevention* vol. 19(8), pp. 1893-1907, 2010.

[6] P. Armitage, G. Berry, and J. N. S. Matthews, in *Statistical Methods in Medical Research,* ed: Blackwell Science Ltd, 2008.

[7] F. Bray, P. McCarron, and D. M. Parkin, "The changing global patterns of female breast cancer incidence and mortality," *Breast Cancer Res,* vol. 6, pp. 229 - 239, 2004.

[8] L. Roux, A. Tutac, N. Lomenie, D. Balensi, D. Racoceanu, A. Veillard, L. Wee-Kheng, J. Klossa, and T. C. Putti, "A cognitive virtual microscopic framework for knowlege-based exploration of large microscopic images in breast cancer histopathology," in *Engineering in Medicine and Biology Society, 2009. EMBC 2009. Annual International Conference of the IEEE*, 2009, pp. 3697-3702.

[9] A. Veillard, Lome, x, N. nie, and D. Racoceanu, "An Exploration Scheme for Large Images: Application to Breast Cancer Grading," in *Pattern Recognition (ICPR), 2010 20th International Conference on*, 2010, pp. 3472-3475.

[10] N. Lomenie and D. Racoceanu, "Spatial relationships over sparse representations," in *Image and Vision Computing New Zealand, 2009. IVCNZ '09. 24th International Conference*, 2009, pp. 226-230.

[11] L. E. George and K. H. Sager, "Breast Cancer Diagnosis using Multi-Fractal Dimension Spectra," in *Signal Processing and Communications, 2007. ICSPC 2007. IEEE International Conference on*, 2007, pp. 592-595.

[12] H. J. G. Bloom and W. W. Richardson, "Histological Grading and Prognosis in Breast Cancer," *Br J Cancer,* vol. 11, pp. 359-377, 1957.

[13] C. W. Elston and I. O. Ellis, "Pathological prognostic factors in breast cancer. I. The value of histological grade in breast cancer: experience from a large study with long-term follow-up," *Histopathology,* vol. 19, pp. 403-410, 1991.

[14] C. W. Elston and E. I.O., *Assessment of histological grade. In Elston, C.W. and Ellis, I.O.* vol. 13. New York: Churchill Livingstone, Edinburgh, 1998.

[15] Tavassoli FA and D. P., *World Health Organization Classification of Tumours: Tumors of the Breast and Female Genital Organs*, 1 ed.: Lyon, 2003.

[16] I. O. Ellis, N. H. S. Cancer Screening Programmes, and Royal College of Pathologists, *Pathology reporting of breast disease : a joint document incorporating the third edition of the NHS Breast Screening Programme's Guidelines for pathology reporting in breast cancer screening and the second edition of the Royal College of Pathologists' Minimum dataset for breast cancer histopathology*: NHS Cancer Screening Programmes ; Royal College of Pathologists, 2005.

[17] M. N. Gurcan, L. E. Boucheron, A. Can, A. Madabhushi, N. M. Rajpoot, and B. Yener, "Histopathological Image Analysis: A Review," *Biomedical Engineering, IEEE Reviews in,* vol. 2, pp. 147-171, 2009.

[18] J. S. Meyer, C. Alvarez, C. Milikowski, N. Olson, I. Russo, J. Russo, A. Glass, B. A. Zehnbauer, K. Lister, and R. Parwaresch, "Breast carcinoma malignancy grading by Bloom-Richardson system vs proliferation index: reproducibility of grade and advantages of proliferation index," *Mod Pathol,* vol. 18, pp. 1067-1078, 2005.

[19] B. Dunne and J. J. Going, "Scoring nuclear pleomorphism in breast cancer," *Histopathology,* vol. 39, pp. 259-265, 2001.

[20] C. H. Huang, D. Racoceanu, L. Roux, and T. C. Putti, "Bio-inspired computer visual system using GPU and Visual Pattern Assessment Language (ViPAL): Application on breast cancer prognosis," in *Neural Networks (IJCNN), The 2010 International Joint Conference on*, 2010, pp. 1-8.

[21] F. A. Tavassoli, *Pathology of The Breast*: McGraw-Hill Professional, 1999.

[22] C. Genestie. (2011, 19-12-2011). Mammary Pathology. Available: http://ipal.cnrs.fr/doc/projects/MammaryPathology_CatherineGenestie_2011.pdf

[23] J. J. Blow and T. U. Tanaka, "The chromosome cycle: coordinating replication and segregation. Second in the cycles review series," *EMBO Rep,* vol. 6, pp. 1028-34, 2005.

[24] E. J. Kaman, A. W. Smeulders, P. W. Verbeek, I. T. Young, and J. P. Baak, "Image processing for mitoses in sections of breast cancer: a feasibility study," *Cytometry*, vol. 5, pp. 244-249, 1984.

[25] T. K. T. Kate, J. A. M. Belien, A. W. M. Smeulders, and J. P. A. Baak, "Method for Counting Mitoses by Image Processing in Feulgen Stained Breast Cancer Sections," *Cytometry*, vol. 14, pp. 241-250, 1993.

[26] J. A. Beli ën, J. P. Baak, P. J. V. Diest, and A. H. V. Ginkel, "Counting mitoses by image processing in Feulgen stained breast cancer sections: the influence of resolution," *Cytometry*, vol. 14, pp. 135-140, 1993.

[27] J.-R. Dalle, W. K. Leow, D. Racoceanu, A. E. Tutac, and T. C. Putti, "Automatic breast cancer grading of histopathological images," in *Engineering in Medicine and Biology Society, 2008. EMBS 2008. 30th Annual International Conference of the IEEE*, 2008, pp. 3052-3055.

[28] J. Hye-Jin, K. Tae-Yoon, H. Hae-Gil, C. Hyun-Ju, P. Hyung-Seon, and C. Heung-Kook, "Comparison of thresholding methods for breast tumor cell segmentation," in *Enterprise networking and Computing in Healthcare Industry, 2005. HEALTHCOM 2005. Proceedings of 7th International Workshop on*, 2005, pp. 392-395.

[29] L. Latson, B. Sebek, and K. A. Powell, "Automated cell nuclear segmentation in color images of hematoxylin and eosin-stained breast biopsy," *Analytical and quantitative cytology and histology the International Academy of Cytology and American Society of Cytology*, vol. 25, pp. 321-331, 2003.

[30] A. Nedzved, S. Ablameyko, and I. Pitas, "Morphological segmentation of histology cell images," in *Pattern Recognition, 2000. Proceedings. 15th International Conference on*, 2000, pp. 500-503 vol.1.

[31] A. Brook, R. El-Yaniv, E. Issler, R. Kimmel, R. Meir, and D. PelegRan, "Breast Cancer Diagnosis From Biopsy Images Using Generic Features and SVMs," *IEEE Transactions on Information Technology in Biomedicine*, vol. In press, 2007.

[32] E. Cosatto, M. Miller, H. P. Graf, and J. S. Meyer, "Grading nuclear pleomorphism on histological micrographs," in *Pattern Recognition, 2008. ICPR 2008. 19th International Conference on*, 2008, pp. 1-4.

[33] J.-R. Dalle, H. Li, C.-H. Huang, W. K. Leow, D. Racoceanu, and T. C. Putti, "Nuclear pleomorphism scoring by selective cell nuclei detection," presented at the IEEE Workshop on Applications of Computer Vision (WACV 2009), Snowbird, Utah, US, 2009.

[34] S. Singh, P. R. Gupta, and M. K. Sharma, "Breast Cancer Detection and Classification of Histopathological Images," *International Journal of Engineering Science and Technology*, vol. 3, pp. 4228-4232, 2010.

[35] A. E. Tutac, D. Racoceanu, T. Putti, X. Wei, L. Wee-Kheng, and V. Cretu, "Knowledge-Guided Semantic Indexing of Breast Cancer Histopathology Images," in *BioMedical Engineering and Informatics, 2008. BMEI 2008. International Conference on*, 2008, pp. 107-112.

[36] S. Petushi, F. Garcia, M. Haber, C. Katsinis, and A. Tozeren, "Large-scale computations on histology images reveal grade-differentiating parameters for breast cancer," *BMC Medical Imaging*, vol. 6, p. 14, 2006.

[37] S. Petushi, C. Katsinis, C. Coward, F. Garcia, and A. Tozeren, "Automated identification of microstructures on histology slides," in *Biomedical Imaging: Nano to Macro, 2004. IEEE International Symposium on*, 2004, pp. 424-427 Vol. 1.

[38] I. Reljin, B. Reljin, I. Pavlovic, and I. Rakocevic, "Multifractal analysis of gray-scale images," in *Electrotechnical Conference, 2000. MELECON 2000. 10th Mediterranean*, 2000, pp. 490-493 vol.2.

[39] F. K. Musgrave, "Fractal forgeries of nature," in *Fractal Geometry and Applications: A Jubilee of Benoît Mandelbrot: Multifractals, Probability and Statistical Mechanics, Applications*. vol. 72, M. L. Lapidus, Ed., ed: Amer Mathematical Society, 2004, pp. 533-574.

[40] A. Hemsley, "Multifractal-Based Biomedical Image Analysis - Automatic Recognition and Classification," University of Canterbury, Christchurch, New Zealand, Report2009.

[41] T. Stojić, I. Reljin, and B. Reljin, "Adaptation of multifractal analysis to segmentation of microcalcifications in digital mammograms," *Physica A: Statistical Mechanics and its Applications*, vol. 367, pp. 494-508, 2006.

[42] L. Yuxin and L. Yanda, "New approaches of multifractal image analysis," in *Information, Communications and Signal Processing, 1997. ICICS., Proceedings of 1997 International Conference on*, 1997, pp. 970-974 vol.2.

[43] K. Uma, K. R. Ramakrishnan, and G. Ananthakrishna, "Image analysis using multifractals," in *Acoustics, Speech, and Signal Processing, 1996. ICASSP-96. Conference Proceedings., 1996 IEEE International Conference on*, 1996, pp. 2188-2190 vol. 4.

[44] I. S. Reljin and B. D. Reljin, "Fractal geometry and multifractals in analyzing and processing medical data and images," *Archive of Oncology*, vol. 10, pp. 283-293, 2002.

[45] K. Falconer, "Random Fractals," in *Fractal Geometry: Mathematical Foundations and Applications*, Second ed Chichester, UK: John Wiley & Sons, Ltd, 2005.

[46] C. Canus and J. L. Vehel, "Change detection in sequences of images by multifractal analysis," in *Acoustics, Speech, and Signal Processing, 1996.*

ICASSP-96. Conference Proceedings., 1996 IEEE International Conference on, 1996, pp. 2172-2175 vol. 4.

[47] E. Nilsson, "Multifractal-based Image Analysis with Applications in Medical Imaging," Master, Department of Computing Science, Umea University, Umea, Sweden, 2007.

[48] A. Hemsley and R. Mukundan, "Multifractal Measures for Tissue Image Classification and Retrieval," in *Multimedia, 2009. ISM '09. 11th IEEE International Symposium on*, 2009, pp. 618-623.

[49] R. Mukundan and A. Hemsley, "Tissue Image Classification Using Multi-Fractal Spectra," *International Journal of Multimedia Data Engineering and Management (IJMDEM)*, vol. 1, pp. 62-75, 2010.

[50] J. Theiler, "Estimating fractal dimension," *J. Opt. Soc. Am. A*, vol. 7, pp. 1055-1073, 1990.

[51] N. Sarkar and B. B. Chaudhuri, "An efficient differential box-counting approach to compute fractal dimension of image," *Systems, Man and Cybernetics, IEEE Transactions on*, vol. 24, pp. 115-120, 1994.

[52] I. H. Song, Y. S. Ji, B. K. Cho, J. H. Ku, Y. J. Chee, J. S. Lee, M. Lee, I. Y. Kim, and S. I. Kim, "Multifractal Analysis of Sleep EEG Dynamics in Humans," in *Neural Engineering, 2007. CNE '07. 3rd International IEEE/EMBS Conference on*, 2007, pp. 546-549.

[53] D. Qi and L. Yu, "Multifractal spectrum theory used to medical image from CT testing," in *Advanced Intelligent Mechatronics, 2008. AIM 2008. IEEE/ASME International Conference on*, 2008, pp. 68-73.

[54] F. Family, B. R. Masters, and D. E. Platt, "Fractal pattern formation in human retinal vessels," *Physica D: Nonlinear Phenomena*, vol. 38, pp. 98-103, 1989.

[55] M. A. Mainster, "The fractal properties of retinal vessels: Embryological and clinical implications," *Eye*, vol. 4, pp. 235-241, 1990.

[56] Landini G, Murray PI, and Misson GP, "Local connected fractal dimensions and lacunarity analyses of 60 degrees fluorescein angiograms," *Invest Ophthalmol Vis Sci*, vol. 36, pp. 2749-2755, 1995.

[57] A. Avakian, R. E. Kalina, E. Helene Sage, A. H. Rambhia, K. E. Elliott, E. L. Chuang, J. I. Clark, J.-N. Hwang, and P. Parsons-Wingerter, "Fractal analysis of region-based vascular change in the normal and non-proliferative diabetic retina," *Current Eye Research*, vol. 24, pp. 274-280, 2002.

[58] T. Stosic and B. D. Stosic, "Multifractal analysis of human retinal vessels," *Medical Imaging, IEEE Transactions on*, vol. 25, pp. 1101-1107, 2006.

[59] J. F. Muzy, E. Bacry, and A. Arneodo, "Multifractal formalism for fractal signals: The structure-function approach versus the wavelet-transform modulus-maxima method," *Physical Review E,* vol. 47, pp. 875-884, 1993.

[60] J. W. Kantelhardt, S. A. Zschiegner, E. Koscielny-Bunde, A. Bunde, S. Havlin, and H. E. Stanley, "Multifractal Detrended Fluctuation Analysis of Nonstationary Time Series," *Physica A Statistical Mechanics and its Applications,* vol. 316, pp. 87-114, 2002.

[61] Y. Shimizu, M. Barth, C. Windischberger, E. Moser, and S. Thurner, "Wavelet-based multifractal analysis of fMRI time series," *NeuroImage,* vol. 22, pp. 1195-1202, 2004.

[62] Y. Shimizu, M. Umeda, H. Mano, I. Aoki, T. Higuchi, and C. Tanaka, "Neuronal response to Shepard's tones. An auditory fMRI study using multifractal analysis," *Brain Research,* vol. 1186, pp. 113-123, 2007.

[63] F. Soares, I. Sousa, F. Janela, J. Seabra, M. Pereira, and M. M. Freire, "Multifractal analysis of Arterial Spin Labeling functional Magnetic Resonance Imaging of the brain," in *Medical Measurements and Applications Proceedings (MeMeA), 2010 IEEE International Workshop on,* 2010, pp. 161-164.

[64] C.-H. Huang, A. Veillard, L. Roux, N. Loménie, and D. Racoceanu, "Time-efficient sparse analysis of histopathological whole slide images," *Computerized medical imaging and graphics : the official journal of the Computerized Medical Imaging Society,* vol. 35, pp. 579-591, 2011.

[65] H. Levkowitz and G. T. Herman, "GLHS: A Generalized Lightness, Hue, and Saturation Color Model," *CVGIP: Graphical Models and Image Processing,* vol. 55, pp. 271-285, 1993.